Modeling and scale-resolving simulations of knocking combustion initiation in a spark ignition engine

Modellierung und skalenauflösende Simulationen der Initiierung klopfender Verbrennung in einem fremdgezündeten Motor

Zur Erlangung des akademischen Grades Doktor-Ingenieur (Dr.-Ing.)
Genehmigte Dissertation von Magnus Kircher aus Frankfurt a. M.
Tag der Einreichung: 05.12.2023, Tag der Prüfung: 20.02.2024

1. Gutachten: Prof. Dr.-Ing. Christian Hasse
2. Gutachten: Prof. Dr.-Ing. Heinz Pitsch
Darmstadt, Technische Universität Darmstadt

TECHNISCHE UNIVERSITÄT DARMSTADT

STFS Simulation of reactive Thermo-Fluid Systems

Mechanical Engineering Department

Modeling and scale-resolving simulations of knocking combustion initiation in a spark ignition engine
Modellierung und skalenauflösende Simulationen der Initiierung klopfender Verbrennung in einem fremdgezündeten Motor

Accepted doctoral thesis by Magnus Kircher

Date of submission: 05.12.2023
Date of thesis defense: 20.02.2024

Darmstadt, Technische Universität Darmstadt

“Begin at the beginning,” the King said gravely,
“and go on till you come to the end.”

— *Lewis Carroll, Alice in Wonderland*

A: “Knock, knock, ...”
B: “Who’s there?”
A: “It’s me! Engine combustion.”

— *MK, MS, HB and VS*

Preface / Vorwort

This dissertation was written in the context of my work as a research assistant at the institute *Simulation of reactive Thermo-Fluid Systems* at the Technical University of Darmstadt. Parts of this work have already been published in the following publications:

- [P1] **M. Kircher**, J. Schneider, S. Popp, S. Gierth, M. Günther, and C. Hasse. Experimental and model-based analysis of combustion and auto-ignition of gasoline and three surrogate fuels in a single-cylinder research engine operated under knocking conditions. In: *Int. J. Engine Res.* 24.6 (2023), pp. 2727–2738. DOI: 10.1177/14680874221133143
- [P2] **M. Kircher**, S. Popp, S. Gierth, A. Pati, J. Schneider, M. Günther, and C. Hasse. Investigation of Engine Combustion and Auto-ignition of a Multicomponent Surrogate Fuel with NTC Behavior Under Knocking Conditions. In: *Flow, Turbul. Combust.* 110.1 (2023), pp. 149–169. DOI: 10.1007/s10494-022-00351-9

Other publications related to this work are:

- [A1] **M. Kircher**, E. Meindl, and C. Hasse. Numerical and experimental study on knocking combustion in turbocharged direct-injection engines for a wide range of operating conditions. In: *Int. J. Engine Res.* 24.2 (2023), pp. 652–671. DOI: 10.1177/14680874211060188
- [A2] J. Schneider, M. Günther, **M. Kircher**, and S. Pischinger. Fiber-optical analysis of weak knock and pressure oscillations in a single cylinder research engine. In: *Proc. Combust. Inst.* 39.1 (2023), pp. 1387–1395. DOI: 10.1016/j.proci.2022.09.005

Part of this work is funded by the Deutsche Forschungsgemeinschaft (DFG, German Research Foundation) – Project number 423158633 as part of the Research unit FOR2687 - Project number 349537577. The author gratefully acknowledges the computing time provided to him on the high-performance computer Lichtenberg at the NHR Centers NHR4CES at TU Darmstadt within the project p0020185. The work of the author is supported by the Graduate School CE within the Centre for Computational Engineering at TU Darmstadt.

An dieser Stelle möchte ich mich bei allen bedanken, die mich während meiner Promotionszeit unterstützt haben.

An erster Stelle Prof. Dr.-Ing. Christian Hasse, der diese Arbeit ermöglicht hat. Seine Betreuung, Diskussionen, Ideen und Anregungen haben wesentlich zur vorliegenden Arbeit beigetragen. Vielen Dank auch an Prof. Dr.-Ing. Heinz Pitsch für die Übernahme des Koreferats sowie die fruchtbare Zusammenarbeit im Rahmen des gemeinsamen Projekts.

Ich möchte mich auch bei meinen Kolleg:innen vom TME für den regelmäßigen Gedankenaustausch und die kontinuierlichen Diskussionen bedanken. Insbesondere möchte ich Jonathan Schneider erwähnen, der mit seinen Messungen die Grundlage für die numerischen Arbeiten lieferte.

Vielen Dank an Hongchao Chu für die Bereitstellung seiner DNS Daten und die damit einhergehende Zusammenarbeit. Seine Koordination im Rahmen der Forschungsgruppe hat erheblich zu ihrem Gelingen beigetragen. An dieser Stelle sei auch allen anderen Forschenden der FOR2687 für die spannenden Einblicke gedankt.

Ein besonderer Dank geht an meine drei Motoren-Gruppenleiter: Dr.-Ing. Sebastian Popp, Dr.-Ing. Sandro Gierth und Dr.-Ing. Andrea Pati. Von ihrem Fachwissen und ihrer langjährigen Erfahrung habe ich stets profitiert und aus den Diskussionen neue Impulse für meine Arbeit gewonnen. Darüber hinaus waren sie für mich von unschätzbarem Wert, was Software und Implementierung angeht.

Besonders hervorheben möchte ich die Zusammenarbeit im *pyFLUT*-Kernteam mit Matthias Steinhausen und Hannes Böttler. Mit einer klaren Vision ist es uns gelungen, diese Software so weiterzuentwickeln, dass sie hoffentlich noch vielen Generationen von Doktorand:innen von Nutzen sein wird. Auch die anregenden Diskussionen bei gemeinsamen Skat-Abenden zusammen mit Vinzenz Schuh und Julian Bissantz haben erheblich zum Gelingen dieser Dissertation beigetragen.

Im Laufe der Jahre habe ich mein Büro mit so vielen Kolleg:innen geteilt, dass es zu viel wäre, sie hier einzeln aufzuzählen. Unabhängig von der Konstellation habe ich immer die familiäre Atmosphäre am STFS genossen und konnte hoffentlich meinen Teil dazu beitragen. Die kreativen Freiräume bei der Ausgestaltung unserer Corporate Identity und die begeisterte Beteiligung der Kolleg:innen haben mir stets große Freude bereitet.

Ein ganz besonderer Dank geht an meine Familie. Ihre bedingungslose Unterstützung hat es mir erst ermöglicht, mein Studium in dieser Form zu absolvieren.

Schließlich möchte ich mich bei meiner Frau bedanken. Sie hat mir in dieser Zeit immer zur Seite gestanden, mich in stressigen Phasen unterstützt und in entspannten Phasen das Leben mit mir genossen. Eva, vielen Dank für Deine Liebe!

Abstract

Climate change has made the reduction of greenhouse gas emissions one of today's top priorities. Currently, individual mobility contributes significantly to global emissions. To reduce these emissions, there is a trend towards electric vehicles. However, combustion engines will remain relevant and the combustion efficiency must be further improved to reduce the carbon dioxide emissions associated with the combustion of fossil fuels.

In this regard, downsizing technology is promising but poses an increased risk of engine damage due to knocking combustion. Here, the stochastic occurrence of knocking combustion requires a knock control that retards the spark timing from the knock limit leading to non-optimal combustion. Therefore, the knock limit is a major limiting factor for engine efficiency.

In this context, the knock resistance is an important parameter that depends on the exact fuel composition. For gasoline fuels, however, the fuel composition is not standardized. Therefore, surrogate fuels are needed for numerical investigations. These surrogate fuels are chosen such that the combustion and auto-ignition properties of gasoline fuels are captured. A particular auto-ignition characteristic is the negative temperature coefficient (NTC) behavior, which might change the knocking combustion initiation. However, there is still a deficiency of comprehensive research on this subject.

In this thesis, a systematic investigation of the knocking combustion initiation, as well as its cycle-to-cycle variations, at the knock limit for surrogate fuels with NTC behavior is performed. First, a measurement campaign investigating the differences in the knocking behavior of three surrogate fuels and gasoline is analyzed. A model-based analysis shows that the NTC behavior of the fuels is relevant for the operating conditions and can potentially change the knocking combustion initiation mechanism. Given these insights, an existing precursor auto-ignition model is extended to capture the non-linear auto-ignition process of fuels with NTC behavior. The model is validated in 0-D configurations before being applied in two 3-D multi-cycle LES studies. Here, the model is capable of reproducing experimental trends of local and global knock quantities. An influence of the NTC behavior on the local auto-ignition process is found taking into account temperature stratification and turbulent flame propagation. Based on the single cycles of the multi-cycle LES, the cycle-to-cycle variations of knocking combustion initiation are analyzed. Correlations are found that show an influence of large-scale flow structures on the combustion process. The associated cycle-to-cycle variations in the local flame propagation in turn lead to local and thus global differences in the subsequent auto-ignition process.

In summary, the findings of this thesis significantly extend the understanding of the cause-and-effect chain of knocking combustion initiation of surrogate fuels with NTC behavior for operating conditions at the knock limit.

Kurzfassung

Der Klimawandel hat die Verringerung der Treibhausgasemissionen zu einer wesentlichen Priorität unserer Zeit gemacht. Derzeit trägt die individuelle Mobilität erheblich zu den globalen Emissionen bei. Um diese zu reduzieren, gibt es einen Trend zu Elektrofahrzeugen. Verbrennungsmotoren sind jedoch weiterhin relevant, und die Verbrennungseffizienz muss weiter gesteigert werden, um die mit der Verbrennung fossiler Kraftstoffe verbundenen Kohlenstoffdioxidemissionen zu verringern.
In dieser Hinsicht ist die Downsizing-Technologie vielversprechend, birgt aber ein erhöhtes Risiko von Motorschäden durch klopfende Verbrennung. In diesem Zusammenhang erfordert das stochastische Auftreten von klopfender Verbrennung eine Klopfregelung. Diese verschiebt den Zündzeitpunkt von der Klopfgrenze weg, was zu einer nicht-optimalen Verbrennung führt. Daher ist die Klopfgrenze ein wesentlicher limitierender Faktor für die motorische Effizienz.
Dabei ist die Klopffestigkeit wichtig, die von der genauen Kraftstoffzusammensetzung abhängt. Bei Benzin ist die Kraftstoffzusammensetzung jedoch nicht genormt. Daher werden für numerische Untersuchungen Surrogatkraftstoffe benötigt. Diese werden so gewählt, dass die Verbrennungs- und Selbstzündeigenschaften von Benzinkraftstoffen erfasst werden. Eine besondere Selbstzündcharakteristik ist negatives Temperaturkoeffizienten (NTC) Verhalten, das die Initiierung klopfender Verbrennung verändern könnte. Es fehlt jeodch noch an umfassender Forschung hierzu.
In dieser Arbeit wird eine systematische Untersuchung der Initiierung klopfender Verbrennung und ihrer zyklischen Schwankungen an der Klopfgrenze für Surrogatkraftstoffe mit NTC-Verhalten durchgeführt. Zunächst wird eine Messkampagne zur Untersuchung der Unterschiede im Klopfverhalten von drei Surrogatkraftstoffen und Benzin analysiert. Eine modellbasierte Analyse zeigt, dass das NTC-Verhalten der Kraftstoffe für die Betriebsbedingungen relevant ist und den Mechanismus der Klopfverbrennungsauslösung potenziell verändern kann. Angesichts dieser Erkenntnisse wird ein bestehendes Precursor-Selbstzündmodell erweitert, um die nicht-lineare Selbstzündung von Kraftstoffen mit NTC-Verhalten zu erfassen. Das Modell wird in 0-D-Konfigurationen validiert, bevor es in zwei 3-D-Multizyklen-LES-Studien angewendet wird. Hier ist das Modell in der Lage, experimentelle Trends der lokalen und globalen Klopfgrößen zu reproduzieren. Unter Berücksichtigung von Temperaturstratifizierung und turbulenter Flammenausbreitung wird ein Einfluss des NTC-Verhaltens auf den lokalen Selbstzündprozess festgestellt. Basierend auf Einzelzyklen der Multizyklen-LES werden die zyklischen Schwankungen der Initiierung klopfender Verbrennung analysiert. Dabei zeigen Korrelationen einen Einfluss von großskaligen Strömungsstrukturen auf den Verbrennungsprozess an. Die damit verbundenen zyklischen Schwankungen der lokalen Flammenausbreitung führen wiederum zu lokalen und damit globalen Unterschieden im nachfolgenden Selbstzündprozess.
Zusammengefasst erweitern die Erkenntnisse dieser Thesis das Verständnis der Wirkkette der Initiierung klopfender Verbrennung von Surrogatkraftstoffen mit NTC-Verhalten für Betriebsbedingungen an der Klopfgrenze erheblich.

Table of contents

1. Introduction

In the face of climate change, one of the key priorities of our time is to reduce greenhouse gas emissions, particularly carbon dioxide. These efforts were initially structured by the Kyoto Protocol [1] and subsequently reinforced by more detailed targets in the Paris Agreement [2]. Individual mobility, which has become an important part of modern society, contributes significantly to global greenhouse gas emissions. The effort to reduce emissions has led to a change in the passenger car market, with sales of electric vehicles increasing [3, 4]. According to the scenario discussed by Yergin [5], electric cars will account for the largest share of new car sales worldwide by 2050, at up to 80%. However, the usage of internal combustion engines (ICEs) in passenger cars is still common. In 2022 the registration of new gasoline cars in the EU was at 36.4% [6]. Globally even 85.6% of cars sold in 2022 were equipped with an ICE which sums up to 63.2 million cars in total [3]. In addition, due to their longevity 1.9 billion cars will drive with ICEs in 2050 [7]. The combustion of common carbon-based fuels in these ICEs is associated with the emission of carbon dioxide, which must be reduced. This can be achieved by optimization of existing engine technologies as an increase in combustion efficiency is equivalent to a reduction in specific emissions.

1.1. Introduction to knocking combustion

In terms of technology, downsizing is a promising route towards increasing efficiency [8]. However, the associated higher cylinder pressures favor knocking combustion [9, 10]. This common irregular combustion phenomenon can lead to extremely high peak cylinder pressures, high-pressure gradients and pressure oscillations. The consequences of these irregularities can include major forms of engine damage. As knocking combustion occurs stochastically, knock control is required to prevent this. Here, the spark timing is retarded from the knock limit to prevent knocking combustion initiation and enable safe engine operation. However, this leads to a non-optimal combustion and reduces the efficiency. With that, knocking combustion at the knock limit is a major limiting factor for engine efficiency and, hence, a crucial aspect of engine and combustion process development [10, 11]. The current understanding of knocking combustion initiation is discussed in Section 1.1.1. Thereafter, the aspects of fuel characteristics (see Section 1.1.2) and modeling of knocking combustion initiation (see Section 1.1.3) are outlined. Finally, the relevance of cycle-to-cycle variations of knocking combustion is discussed in Section 1.1.4

1.1.1. Knocking combustion theory

In the past, different theories have been proposed to explain the occurrence of knocking combustion based on either auto-ignition, detonation, or a combination of both [9, 12, 13]. The current understanding of knocking combustion initiation is schematically depicted in Figure 1.1 and discussed in the following.

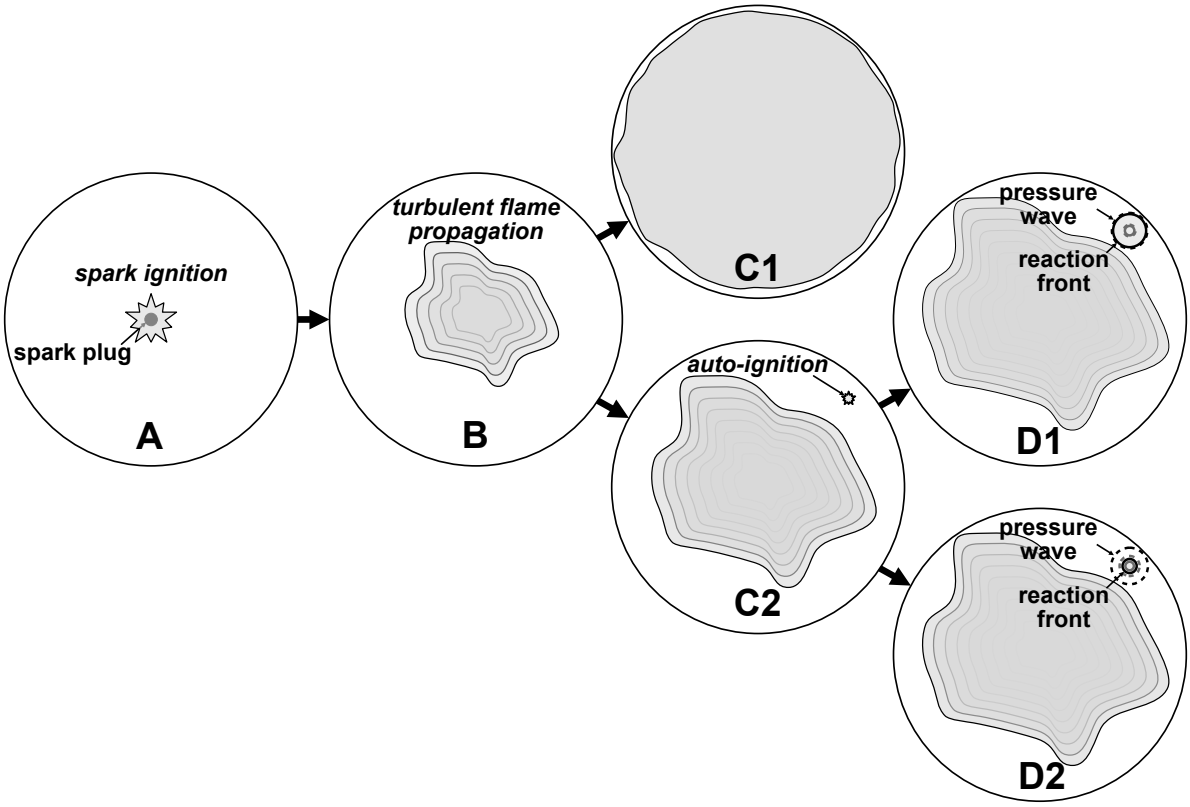

Figure 1.1.: Schematic of regular and knocking combustion. Spark ignition of an air-fuel mixture (**A**) results in turbulent propagation of a flame front (**B**). In a regular combustion, the entire mixture is consumed (**C1**). Knocking combustion is always initiated by auto-ignition in the unburned mixture (**C2**). For a developing detonation (**D1**), the pressure wave (dashed line) and reaction front (solid line) propagate at a similar speed (gray lines represent earlier time instants than black lines). In deflagrative mode (**D2**), the pressure wave and reaction front are immediately separated.

In a spark ignition engine, energy in the form of a spark is deposited in the cylinder to initiate the combustion of an air-fuel mixture (**A**). Subsequently, a turbulent flame front develops and propagates through the cylinder (**B**). Thereafter, the further progress differs:

- *Regular combustion*: In the case of the desired regular combustion, this flame propagation consumes the entire fresh mixture (**C1**).
- *Knocking combustion*: In contrast, knocking combustion is always initiated by auto-ignition events in the unburned mixture which are ahead of the flame front and clearly separated

spatially (**C2**), which was first shown by Spicher et al. [14]. Following an auto-ignition event, different propagation modes can develop that determine the intensity of knock [15–18]. Building upon studies by Zeldovich [19] and König et al. [15], Bradley et al. [16] proposed a theory for classifying the propagation modes originating from exothermic centers. In this context, two main types of knocking combustion are distinguished, strong knock and light knock:

- *Strong knock*: High amplitude pressure oscillations associated with strong knock appear to be caused by developing detonations. Here, the reaction front and the pressure wave resulting from auto-ignition propagate at similar velocities (**D1**). Subsequently, these fronts couple and form a detonation wave. This process is denoted a deflagration to detonation transition (DDT).
- *Light knock*: In contrast, light knock is characterized by low-pressure oscillations. These result from a deflagrative mode in which the reaction front emerging from auto-ignition is immediately separated from the respective pressure wave (**D2**). Here, the knock intensity depends primarily on the amount of auto-ignited mass [20].

The knock limit, which is the focus of this thesis, is characterized by low knock intensity and thus light knock.

1.1.2. Fuel characteristics

Knocking combustion has been investigated both experimentally and numerically in the past. The recently published review article by Wang et al. [10] summarizes the technological and scientific aspects of knocking combustion. Experimental campaigns are well-suited to collect a large amount of data enabling analysis of global trends and statistics of knocking combustion. Numerical investigations can complement this by providing additional temporal and spatial information. This allows a detailed analysis of specific phenomena that cannot be investigated experimentally.

Experimental investigations of knocking combustion often use conventional gasoline fuels (e.g., in the studies by Robert et al. [21] and Fontanesi et al. [22]). These fuels are mixtures of several different large hydrocarbons, such as alkanes, alcohols and aromatics. However, the exact composition of gasoline is not standardized. Therefore, numerical studies consider surrogate fuels which consist of a reduced number of known components [23]. These surrogates must reproduce the combustion and auto-ignition characteristics of gasoline fuel to enable a comprehensive analysis that incorporates both experimental data and simulations. Alternatively, the experiments themselves should directly employ surrogate fuels, as is the case in this thesis.

In the context of knocking combustion, the knock resistance of a fuel is an important characteristic. The experimental evaluation is based on Primary Reference Fuels (PRFs) which consist of isooctane and n-heptane. The knock resistance is expressed in terms of the research octane number (RON) and the motor octane number (MON). Here, the octane sensitivity (OS) is defined as the difference between RON and MON, has positive values for real gasoline fuels [23] and indicates the difference of a fuel from a PRF [24]. To determine the RON and MON, the relative proportion of isooctane and n-heptane is varied until the knock behavior of the tested fuel is reached. Common gasoline fuels have a RON of around 90, depending on local legal regulations.

With that, a mixture of mostly isooctane shows the same knock resistance as gasoline, which makes isooctane a common single-component surrogate fuel. In recent numerical studies, it has been used to investigate knocking combustion [20, 25]. However, the OS of isooctane is zero by definition, which is unrealistic for common gasoline fuels. Pera et al. [26] showed that ternary mixtures, e.g., mixtures of isooctane, heptane and toluene, so-called Toluene Reference Fuels (TRFs), are needed to formulate a proper surrogate fuel for gasoline. These TRFs mimic the aromatic content of real gasoline fuels and can provide a good match for main gasoline properties such as RON, MON, OS, liquid density and H/C ratio [27]. The above-mentioned studies by Robert et al. [21] and Fontanesi et al. [22] incorporated TRFs for the numerical investigations. To account for the alcohol content of modern gasoline fuels, ethanol is often added to these TRFs [28]. In addition to isooctane, two such TRFs are considered in this thesis, one of which is examined in detail in LES studies.

For numerical investigations of knocking combustion, the auto-ignition delay times as well as burning velocity must be properly captured by the surrogate formulation. Here, the increasing complexity of surrogate fuels makes it possible to take into account important aspects such as the low-temperature chemistry that many large hydrocarbons exhibit. This low-temperature chemistry leads to more complex auto-ignition behavior and may result in negative temperature coefficient (NTC) behavior [29–31]. While typically the auto-ignition delay times decrease with increasing temperature, the auto-ignition delay times increase with rising temperature within the NTC regime. The surrogate fuels considered in this thesis show NTC behavior, which is therefore a particular focus.

For the thermodynamic conditions in the NTC regime, two-stage auto-ignition occurs [31, 32]. The relevance of NTC behavior for knocking combustion was investigated in several studies, which have found that low NTC sensitivity fuels show high OS [28, 33, 34]. For a fuel with NTC behavior, Dai et al. [35] showed in a numerical study that after auto-ignition initiated by a cool spot, propagation modes similar to hot-spot auto-ignition develop, and concluded that this could lead to knocking combustion. However, there is no systematic study investigating such behavior in a combined experimental and numerical analysis.

1.1.3. Modeling of knocking combustion initiation

The accurate prediction of the detailed auto-ignition process of a surrogate fuel is the first prerequisite for numerical investigations of knocking combustion initiation. There are two common approaches of knock modeling in the context of numerical simulations: the direct modeling of the auto-ignition process and the determination of the auto-ignition reaction progress by a precursor model.

- *Direct modeling*: Directly modeling the auto-ignition process requires detailed chemical kinetics. The associated high computational costs can be reduced by simplified kinetic approaches [36, 37]. This was employed in several RANS and one LES study based on the G-equation model for flame propagation and finite-rate chemistry for the unburned gas for different surrogate fuels with reduced or skeletal mechanisms of varying complexity [38–42]. The pre-tabulation of chemistry is used in the tabulated kinetics of ignition (TKI) model [43, 44], which was applied to RANS studies investigating homogeneous charge

compression ignition (HCCI) and Controlled Auto-Ignition (CAI) engines [45, 46] and modified to analyze auto-ignition in a spark ignition (SI) engine [47]. A similar approach was used for LES investigations of knocking combustion by Robert et al. [20, 21, 25].

- *Precursor model*: In a precursor model, the evolution of a real (e.g., formaldehyde) or pseudo species is assumed to capture the auto-ignition process. In this regard, Livengood and Wu [48] proposed the knock integral method (KIM). For simplicity, a linear relation between the auto-ignition delay time and the precursor mass fraction is assumed. In particular, the chemical source term of the precursor is expressed as the reciprocal of the auto-ignition delay time. For the application in CFD simulations, empirical correlations [49, 50] or reaction mechanisms of varying complexity [51, 52] were used to calculate and tabulate the auto-ignition delay times, respectively. Linse et al. [53] developed the generalized knock integral method (gKIM), which incorporates the effect of turbulent fluctuations. Further adaption and application to a broader range of operating conditions demonstrated the capabilities of this approach [A1]. These RANS studies were based on complex mechanisms for isooctane. The extension of this model to surrogates with NTC behavior and to the LES context is part of this thesis.

1.1.4. Cycle-to-cycle variations in knocking combustion

The unsteady nature of ICE operation is a particular aspect of knocking combustion. Even for nominal stable operation conditions, the combustion process varies from cycle to cycle [54]. This results in variations of the cylinder pressure which commonly are referred to as cycle-to-cycle variations (CCVs) [55]. In particular, the heat release is different and thus are the thermodynamic conditions in the unburned gas, where auto-ignition may occur. Hence, the tendency of knocking combustion initiation varies from cycle to cycle. This poses a challenge for the investigation of knocking combustion.

There have been numerous numerical and experimental studies attempting to identify the causes and influencing factors of CCVs of combustion as summarized in the review articles by Young [54] and Ozdor [55]. Young [54] postulated that CCVs begin early in the cycle and that velocities in the spark region seem to have a significant influence. Ozdor [55] strengthened this hypothesis and identified the magnitude and direction of the local spark velocity as the main factors influencing the combustion process. This was subsequently further investigated in multiple experimental studies incorporating cylinder pressure measurements and imaging techniques for flow, spark and flame propagation [56–60]. In terms of numerical investigations, RANS simulations, which capture ensemble averages, are generally not suitable to investigate CCVs [61]. In contrast, single cycles of multi-cycle LES studies allow the analysis and understanding of fundamental physics and the complex interactions between the different processes causing CCVs [62]. Respective LES studies [63–65] confirmed, that the local spark velocity is influencing the combustion process. Other studies identified the kinetic energy [66] or the location of coherent vortex structures [67] as influencing factors of CCV. Truffin et al. [64] emphasize that there is no universal hierarchy of influencing factors, but that they seem to depend on engine geometry and operating conditions.

Investigating knocking combustion, a deeper understanding of the CCVs, particularly at the knock limit, is important [55]. Recent LES studies [20–22, 25, 42, 68] demonstrated the benefits of LES over RANS. In particular, by resolving CCVs, the influence of single cycles on the mean knock behavior can be investigated. In addition, correlations between physical phenomena can be analyzed. Here, Fontanesi et al. [22] and Robert et al. [21] found correlations between the flow velocity in the spark vicinity and the global burn rate. Robert et al. [25] presented a qualitative comparison of individual locations of auto-ignition. However, the global trend of these locations was attributed to heat transfer or residence times and the local randomness to turbulence, without further in-detail analysis. There is no systematic study of the correlations of flow, combustion and auto-ignition. Thus, such analysis is conducted in this thesis in the search for the causes of CCVs of knocking combustion initiation.

1.2. Objectives and structure of this thesis

While the use of more complex fuels enables a better replication of the real gasoline fuels, these fuels show different combustion and auto-ignition behavior that affects the knocking combustion characteristics. Several studies indicate that especially NTC behavior might have a significant effect on knocking combustion initiation. To better understand the impact of NTC, a systematic experimental and numerical analysis of the effect of NTC on knocking combustion initiation is performed. To the best of the author's knowledge, this is the first of its kind.

Although recent LES studies considered TRF surrogate fuels, similar to those considered in this thesis, the operating conditions were outside the NTC regime or the effects of NTC behavior on the auto-ignition process have not been addressed. With that, the influence of NTC behavior on the local auto-ignition process is unknown. To investigate how the local auto-ignition process is influenced by temperature stratification and flame propagation under thermodynamic conditions in the NTC regime, an LES study is performed.

Recently, LES studies have also been employed for the analysis of CCVs. However, the studies mainly focused on the investigation of correlations between flow and combustion. So far, studies on knocking combustion aim to capture the CCVs of knocking combustion but provide only limited analysis of the causes of the CCVs. In this thesis, based on a multi-cycle engine LES study, a systematic analysis of the correlations between flow, combustion and auto-ignition and thus the causes of CCVs of knocking combustion initiation is performed.

In particular, this thesis focuses on the systematic investigation of the knocking combustion initiation at the knock limit for surrogate fuels with NTC behavior. A comprehensive experimental database of three surrogate fuels and gasoline is used to analyze the knocking behavior. The research investigates both global and local auto-ignition processes and aims to understand the cause-and-effect chain of cycle-to-cycle variations in knocking combustion initiation. The investigation starts with a global perspective and progressively advances to more detailed insights through local analysis. Increasingly complex simulation setups are used, evolving from simplified configurations to multi-cycle LES with high spatial and temporal resolution. Further, an extended auto-ignition model is proposed and validated in this thesis.

The main objectives are summarized as follows:

- *Analysis of knock characteristics of surrogate fuels*: The differences in knocking combustion behavior between surrogate fuels in comparison to gasoline are analyzed based on a comprehensive experimental database (see Section 5.1). Subsequently, the fuel influence on combustion and auto-ignition is investigated in a model-based analysis. Here, the relevance of NTC behavior, which all of the surrogate fuels exhibit, is evaluated (see Section 5.2).
- *Model extension*: Based on the previous findings, an existing precursor model is extended to properly capture the non-linear auto-ignition behavior that occurs for surrogate fuels with NTC behavior (see Section 2.2.2). Subsequently, the new source term formulation is evaluated using a DNS dataset (see Section A.1). After validation of the extended auto-ignition model in 0-D configurations (see Section 5.3), it is subsequently employed in 3-D LES studies (see Chapter 6).
- *Analysis of the local auto-ignition process*: The first LES study is conducted to investigate the influence of NTC behavior on the local auto-ignition process (see Section 6.1). Here, the effects of temperature stratification and turbulent flame propagation are the main focus.
- *CCVs of knocking combustion initiation*: Extending the methodology, the second multi-cycle LES study considers the influence of different initial flow conditions on the knocking combustion initiation (see Section 6.2). In particular, the local and global CCVs of combustion and auto-ignition are investigated. In this context, correlations between the local processes of flow, combustion and auto-ignition are analyzed in the search for the causes of these CCVs.

The remainder of this thesis is structured as follows: In Chapter 2 the governing equations and the modeling approaches used in this thesis are discussed. The experimental configurations and the experimental database are introduced in Chapter 3. Subsequently, the numerical setup of the engine LES is described in Chapter 4. Chapter 5 addresses the analysis of knock characteristics of surrogate fuels. The conducted multi-cycle LES studies are discussed in Chapter 6. First, the influence of stratification and turbulent flame propagation is discussed in Section 6.1. Thereafter, CCVs are discussed and analyzed in Section 6.2. Finally, in Chapter 7, conclusions are drawn and an outlook is given.

2. Governing equations, models and numerical methods

Numerical simulations are based on solving a set of equations tailored to the respective use case. Within this work, knocking combustion initiation is simulated, which is a complex multi-physics problem involving turbulent flow, combustion and auto-ignition. Some of these processes are modeled rather than directly solved based on fundamental equations. In the following, the governing equations as well as models and numerical methods are discussed.

2.1. Governing equations

The governing equations for a fluid-mechanical problem are based on the principles of mass, momentum and energy conservation. These are discussed in the following together with closure models incorporated to enable the solving of those equations in a computational fluid dynamics (CFD) simulation. The equations discussed within this section are based on [69].

Navier stokes equations

The dynamics of a single-phase turbulent flow can be described by the Navier-Stokes equations:

$$\frac{\partial \rho}{\partial t} + \frac{\partial \rho u_i}{\partial x_i} = 0\,, \tag{2.1}$$

$$\frac{\partial}{\partial t}\rho u_j + \frac{\partial}{\partial x_i}\rho u_i u_j = -\frac{\partial p}{\partial x_j} + \frac{\partial \tau_{ij}}{\partial x_i} + \rho g_j\,. \tag{2.2}$$

Here, ρ is the gas density, u_i the velocity in direction i, g_j the gravitational acceleration and τ_{ij} the viscous stress tensor, which is expressed as:

$$\tau_{ij} = \mu\left(\frac{\partial u_i}{\partial x_j} + \frac{\partial u_j}{\partial x_i}\right) - \frac{2}{3}\mu\frac{\partial u_k}{\partial x_k}\delta_{ij}\,. \tag{2.3}$$

Here, δ_{ij} is the Kronecker delta and μ is the dynamic viscosity, which is retrieved from a closure model (see Section 2.1.1).

Species conservation equation

In a multicomponent flow the mass conservation applies for each species mass fraction Y_k, resulting in the following equation:

$$\frac{\partial \rho Y_k}{\partial t} + \frac{\partial}{\partial x_i}\left(\rho\left(u_i + V_{k,i}\right) Y_k\right) = \dot{\omega}_k \,, \tag{2.4}$$

with $V_{k,i}$ being the diffusion velocity of species k (see Section 2.1.1) and $\dot{\omega}_k$ the respective source term due to chemical reactions.

Energy conservation equation

In this work, energy is expressed in terms of total enthalpy h_t, which considers the kinetic energy, $0.5 u_i u_i$, and the specific enthalpy h of the mixture:

$$h = \sum_{k=1}^{n} h_k Y_k \,. \tag{2.5}$$

Here, the specific enthalpy h_k of species k results from its standard enthalpy of formation $\Delta h^0_{f,k}$ and the sensible enthalpy h_s:

$$h_k = \underbrace{\int_{T_0}^{T} c_{p,k} dT}_{h_s} + \Delta h^0_{f,k} \,. \tag{2.6}$$

For the determination of the sensible enthalpy, T_0 is the reference temperature of $298.15\,\mathrm{K}$ and $c_{p,k}$ is the heat capacity at constant pressure which is retrieved from a closure model (see Section 2.1.1).

Capturing the energy conservation, the transport equation of total enthalpy h_t is solved:

$$\frac{\partial \rho h_t}{\partial t} + \frac{\partial \rho u_i h_t}{\partial x_i} = \frac{\partial p}{\partial t} - \frac{\partial q_i}{\partial x_i} + \frac{\partial \tau_{ij} u_i}{\partial x_j} + \rho u_j g_j \,. \tag{2.7}$$

Here, q_i is the energy flux:

$$q_i = -\lambda \frac{\partial T}{\partial x_j} + \rho \sum_{k=1}^{N} h_k Y_k V_{k,i} \,. \tag{2.8}$$

The first term represents the heat flux and applies Fourier's Law with the thermal conductivity λ, which is determined by a closure model (see Section 2.1.1). The second term stems from the diffusion of species with different enthalpies.

2.1.1. Closure models

The equations introduced above contain unknown variables that require modeling. The respective closure models are discussed in the following.

Diffusion velocity

Determination of the diffusion velocity is costly when the interaction of all species is considered. The common mixture average diffusion approach uses the Hirschfelder and Curtiss approximation [70] and reads:

$$V_{k,i} = -D_k \frac{1}{X_k} \frac{\partial X_k}{\partial x_i}, \tag{2.9}$$

where X_k is the mole fraction of species k. The diffusivity D_k of species k into the mixture is given by:

$$D_k = \frac{1 - Y_k}{\sum_{k \neq l} X_l / \mathcal{D}_{k,l}}. \tag{2.10}$$

Here $\mathcal{D}_{k,l}$ is the binary diffusion coefficient of species k and l. The dimensionless Lewis number Le_k is the quotient of species diffusivity D_k and thermal diffusivity $\alpha = \lambda/(\rho c_p)$:

$$\mathrm{Le}_k = \frac{\alpha_k}{D_k}. \tag{2.11}$$

Within the approximation referred to as the unity Lewis number approach, it is assumed that the Lewis number is unity for all species. With that, the diffusion velocity can be expressed by Fick's Law and reads:

$$V_{k,i} = -D \frac{1}{Y_k} \frac{\partial Y_k}{\partial x_i} \tag{2.12}$$

Thermophysical properties

The dynamic viscosity μ used in Eq. (2.3) to determine the viscous stress tensor and the thermal conductivity used in Eq. (2.8) are calculated by weighted sums of the individual properties of each species k:

$$\mu = \sum_{k=1}^{N} Y_k \mu_k, \tag{2.13}$$

$$\lambda = \sum_{k=1}^{N} Y_k \lambda_k, \tag{2.14}$$

where μ_k and λ_k are retrieved from a temperature-dependent polynomial form in the simulation.

The heat capacity $c_{p,k}$ is required to correlate enthalpy to temperature (see Eq. 2.6). The molar based quantities $c^m_{p.k}$ and h^m_k are retrieved from the so-called NASA polynomial form [71]:

$$\frac{c_p^m(T)}{R} = a_0 + a_1 T + a_2 T^2 + a_3 T^3 + a_4 T^4, \tag{2.15}$$

$$\frac{h^m(T)}{RT} = a_0 + \frac{a_1}{2} T + \frac{a_2}{3} T^2 + \frac{a_3}{4} T^3 + \frac{a_4}{5} T^4 + \frac{a_5}{T}, \tag{2.16}$$

with the universal gas constant $R = 8.314\,\mathrm{J\,K^{-1}\,mol^{-1}}$. The specific quantities are then retrieved from the molar-based quantities by division with the species molar mass M_k, e.g. $c_{p,k} = c^m_{p,k}/M_k$.

The ideal gas law is used as the equation of state:

$$p = \rho \frac{R}{M} T \tag{2.17}$$

Contribution of control volume motion

In the context of engine simulations, the domain of interest is defined by moving parts, e.g. the piston and the valves. With that, the fluid is not enclosed by a fixed volume anymore. In the finite volume method (FVM) approach, this movement of faces of the control volume results in additional mesh-induced fluxes that need to be accounted for. For a generic scalar ϕ, the respective transport equation in integral form reads:

$$\int_{V_p} \frac{\partial \rho\phi}{\partial t} dV + \int_{V_p} \frac{\partial}{\partial x_i} \cdot \left[\rho\phi \left(u_i - u_{\mathrm{f},i}\right)\right] dV - \int_{V_p} \frac{\partial}{\partial x_i} \cdot \left(\rho\Gamma_\phi \frac{\partial \phi}{\partial x_i}\right) dV = \int_{V_p} S_\phi \phi dV \,. \tag{2.18}$$

Here, the volume to integrate, dV, is a function of time, Γ_ϕ is a diffusion coefficient and S_ϕ is a source term. The mesh motion is taken into account by the inclusion of the mesh velocity $u_{\mathrm{f},i}$ in the convective term. This adaption is applied to the previously discussed conservation equations. Further details on the implications of mesh motion concerning implementation and discretization can be found in [72–74].

2.1.2. Turbulence modeling

The flow inside an engine is characterized by its transient nature. Depending on the engine phase, different flow length scales dominate the overall flow structure. During the intake phase, the fresh mixture enters the cylinder through the relatively small valve gap and generates a transient high-velocity jet. This creates a large-scale tumble motion which is compressed during the compression phase and finally breaks up when the piston approaches the top dead center (TDC). These three-dimensional, transient and chaotic flows are considered turbulent and comprise eddy structures of different time and length scales.

Following the theory of Kolmogorov [75, 76], large eddies break up into smaller forming an energy cascade. Resolving all temporal and spatial turbulent scales in a Direct Numerical Simulation (DNS) requires very small time steps and computational cells, which typically limits its application to simplified configurations. Within the Reynolds Averaged Navier Stokes (RANS) approach, the flow is statistically described by decomposing the flow into a time-averaged and a fluctuating component. The development of the unsteady RANS (URANS) method enabled the simulation of transient flows by replacing the time-average with an ensemble-average. Nevertheless, the statistical nature of RANS prevents the in-detail analysis of individual transient phenomena in the context of engine simulations [62]. To enable such analyses based on single cycles, this work uses the Large Eddy Simulation (LES) method for turbulence modeling [77].

Here, the scales are filtered and the respective operator $\overline{\square}$ reads:

$$\overline{\phi}\left(x_i\right) = \int \phi\left(x_i, r_j\right) G\left(x_i, r_j\right) dr_j \,, \tag{2.19}$$

where $G\left(x_i, r_j\right)$ is the filter kernel centered at x_i and spanning a radius r_j. This results in the resolution of the large turbulent structures while the small scales are unresolved:

$$\phi = \overline{\phi} + \phi' \,. \tag{2.20}$$

For an implicit LES, as used in this work, scale separation is achieved implicitly by the discretization [78]. Respectively, the unresolved scales are often referred to as sub-grid scales (SGS). For compressible flows, the Favre-filter $\widetilde{\square}$, a density-weighted filter operation is introduced:

$$\widetilde{\phi} = \frac{\overline{\rho\phi}}{\overline{\rho}} \,. \tag{2.21}$$

Application of the Favre-averaging [69] to Equations (2.1), (2.2), (2.4) and (2.7) yields:

$$\frac{\partial \overline{\rho}}{\partial t} + \frac{\partial \overline{\rho}\widetilde{u}_i}{\partial x_i} = 0 \tag{2.22}$$

$$\frac{\partial \overline{\rho}\widetilde{u}_i}{\partial t} + \frac{\partial}{\partial x_i}\left(\overline{\rho}\widetilde{u}_i\widetilde{u}_j\right) = -\frac{\partial \overline{p}}{\partial x_j} + \overline{\rho}g_j + \frac{\partial}{\partial x_i}\left(\overline{\tau}_{ij} - \tau_{ij}^{\mathrm{SGS}}\right) \,, \tag{2.23}$$

$$\frac{\partial(\overline{\rho}\widetilde{Y}_k)}{\partial t} + \frac{\partial}{\partial x_i}(\overline{\rho}\widetilde{u}_i\widetilde{Y}_k) = \frac{\partial}{\partial x_i}\left[\overline{\rho}\left(\widetilde{D} + \frac{\nu_{\mathrm{SGS}}}{\mathrm{Sc}_{\mathrm{SGS}}}\right)\left(\frac{\partial \widetilde{Y}_k}{\partial x_i}\right)\right] + \widetilde{\dot{\omega}}_k \,. \tag{2.24}$$

$$\frac{\partial \overline{\rho}\widetilde{h}_t}{\partial t} + \frac{\partial}{\partial x_i}(\overline{\rho}\widetilde{u}_i\widetilde{h}_t) = \frac{\partial \overline{p}}{\partial t} - \frac{\partial}{\partial x_i}\left(\overline{q}_i - q_i^{\mathrm{SGS}}\right) + \overline{\rho}\widetilde{u}_j g_j \,, \tag{2.25}$$

Here, $\mathrm{Sc}_{\mathrm{SGS}}$ is the sub-grid scale Schmidt number which is set to 0.4 in this work unless stated otherwise. The filtered heat flux $\overline{q}_i$ is expressed as:

$$\overline{q}_i = -\frac{\overline{\lambda}}{c_p}\frac{\partial \widetilde{h}}{\partial x_i} \tag{2.26}$$

and the sub-grid heat flux $q_i^{\mathrm{SGS}} = \overline{\rho}\left(\widetilde{u_i h_t} - \widetilde{u}_i\widetilde{h}_t\right)$ is modeled as:

$$q_i^{\mathrm{SGS}} = -\overline{\rho}\frac{\nu_{\mathrm{SGS}}}{\mathrm{Pr}_{\mathrm{SGS}}}\frac{\partial \widetilde{h}_t}{\partial x_i} \,, \tag{2.27}$$

where the Prandtl number $\mathrm{Pr}_{\mathrm{SGS}} = \alpha_{\mathrm{t}}/\nu_{\mathrm{SGS}}$ relates thermal diffusivity α_{t} and sub-grid viscosity ν_{SGS}. The filtered viscous stress tensor $\overline{\tau}_{ij}$ reads:

$$\overline{\tau}_{ij} = \overline{\mu}\left(\frac{\partial \widetilde{u}_i}{\partial x_j} + \frac{\partial \widetilde{u}_j}{\partial x_i} - \frac{2}{3}\delta_{ij}\frac{\partial \widetilde{u}_k}{\partial x_k}\right) \,. \tag{2.28}$$

The SGS viscous stress tensor $\tau_{ij}^{\mathrm{SGS}} = \overline{\rho}\left(\widetilde{u_i u_j} - \widetilde{u}_i \widetilde{u}_j\right)$ is modeled adopting the Boussinesq hypothesis [79]:

$$\tau_{ij}^{\mathrm{SGS}} - \frac{1}{3}\tau_{kk}^{\mathrm{SGS}}\delta_{ij} = -\overline{\rho}\nu_{\mathrm{SGS}}\left(\frac{\partial \widetilde{u}_i}{\partial x_j} + \frac{\partial \widetilde{u}_j}{\partial x_i} - \frac{2}{3}\delta_{ij}\frac{\partial \widetilde{u}_k}{\partial x_k}\right) . \tag{2.29}$$

The sub-grid scale viscosity ν_{SGS} is modeled utilizing the σ-model [80]:

$$\nu_{\mathrm{SGS}} = \left(C_\sigma \Delta\right)^2 \mathcal{D}_\sigma\left(u_i\right) , \tag{2.30}$$

$$\mathcal{D}_\sigma = \frac{\sigma_3\left(\sigma_1 - \sigma_2\right)\left(\sigma_2 - \sigma_3\right)}{\sigma_1^2} , \tag{2.31}$$

with $\sigma_1 \geq \sigma_2 \geq \sigma_3$ being the singular values of the velocity gradient tensor, and the model constant C_σ is set to 1.5 in this work. The characteristic sub-grid scale length Δ is determined based on the cell volume V_{cell}:

$$\Delta = V_{\mathrm{cell}}^{1/3} . \tag{2.32}$$

2.2. Turbulent knocking combustion modeling

Knocking combustion results from auto-ignition events ahead of the turbulent propagating flame front (see Figure 1.1). Thus, turbulent flame propagation and turbulent auto-ignition must be captured properly, which is incorporated by the respective models discussed in the following.

2.2.1. Turbulent flame propagation modeling

The modeling of turbulent combustion considers two aspects: a proper description of the local reaction zone and the interaction of the flame front with the turbulence. In an ICE, the local combustion process is influenced by parameters such as pressure, temperature of the unburned gas or mass fraction of exhaust gas recirculation (EGR). Those need to be accounted for as discussed in the following.

Flamelet-based manifolds

Flamelet-based manifolds utilize the assumption, that a 3-D flame is an ensemble of 1-D flame structures, the so-called flamelets. With that, the thermochemical states occurring in a 3-D flame can be reconstructed from a manifold of pre-calculated flamelets [81–85]. However, these flamelets need to capture the dominating effects occurring in the 3-D flame. Hence, the flamelet-based manifold needs to be tailored for the respective application. In this work, a detailed gasoline surrogate mechanism with 485 species and 2081 reactions [86] is used for the generation of combustion and auto-ignition manifolds, which are described in the following.

Combustion manifold

The flamelet-based manifold used for the combustion model described below is based on 1-D laminar freely propagating flames. The individual calculations are performed with *cantera* [87] while the in-house code *pyFLUT* performs the parameter variations of the initial conditions and generates the manifold. As initial conditions, the pressure p, the unburned temperature T_u and the initial composition are varied (see Table 2.1). The latter is fixed to the stochiometric value of mixture fraction Z but takes into account different exhaust gas recirculation (EGR) mass fractions Y_EGR. The variation in T_u spans different enthalpy levels h, which are then mapped to a normalized enthalpy h_norm:

$$h_\mathrm{norm}(Z,p,Y_\mathrm{EGR}) = \frac{h - h_\mathrm{min}(Z,p,Y_\mathrm{EGR})}{h_\mathrm{max}(Z,p,Y_\mathrm{EGR}) - h_\mathrm{min}(Z,p,Y_\mathrm{EGR})}\,. \tag{2.33}$$

Here, $h_\mathrm{max}(Z,p,Y_\mathrm{EGR})$ and $h_\mathrm{min}(Z,p,Y_\mathrm{EGR})$ are the maximum and minimum enthalpies for a given level of Z, p and Y_EGR.

The reaction progress variable Y_c is defined by the sum of mass fractions of carbon dioxide and carbon monoxide: $Y_\mathrm{c} = Y_\mathrm{CO2} + Y_\mathrm{CO}$. The normalized reaction progress variable c is given by

$$c(Z,p,h_\mathrm{norm},Y_\mathrm{EGR}) = \frac{Y_\mathrm{c} - Y_\mathrm{c,min}(Z,p,h_\mathrm{norm},Y_\mathrm{EGR})}{Y_\mathrm{c,max}(Z,p,h_\mathrm{norm},Y_\mathrm{EGR}) - Y_\mathrm{c,min}(Z,p,h_\mathrm{norm},Y_\mathrm{EGR})}\,, \tag{2.34}$$

Table 2.1.: Parameter variation of combustion manifold

Parameter	min. value	max. value	# steps
p	$0.8\,\mathrm{bar}$	$70\,\mathrm{bar}$	20
T_u	$300\,\mathrm{K}$	$1000\,\mathrm{K}$	15
Y_EGR	0	1	11

where $Y_\mathrm{c,min}(Z, p, h_\mathrm{norm}, Y_\mathrm{EGR})$ is the respective value in the unburned and $Y_\mathrm{c,max}(Z, p, h_\mathrm{norm}, Y_\mathrm{EGR})$ that in the burned mixture. The parameterization of the thermo-chemical state $\boldsymbol{\varphi}$ in the manifold is defined by the mixture fraction Z, normalized reaction progress variable c, pressure p, normalized enthalpy h_norm and exhaust gas recirculation EGR, i.e. $\boldsymbol{\varphi} = \boldsymbol{\varphi}(Z, c, p, h_\mathrm{norm}, Y_\mathrm{EGR})$.

Flame surface density model

The modeling of the turbulent flame propagation is based on an algebraic flame surface density (FSD) model [88] coupled to the previously described combustion manifold. In the LES, a transport equation is solved for the normalized reaction progress variable $\widetilde{c}$ [69]:

$$\frac{\partial(\overline{\rho}\widetilde{c})}{\partial t} + \frac{\partial(\overline{\rho}\widetilde{u}_i\widetilde{c})}{\partial x_i} = \frac{\partial}{\partial x_i}\left(\frac{\mu_\mathrm{SGS}}{\mathrm{Sc}_\mathrm{SGS}}\frac{\partial\widetilde{c}}{\partial x_i}\right) + \rho_\mathrm{u} s_\mathrm{L}\Sigma\,. \tag{2.35}$$

Here, $\rho_\mathrm{u}, \mu_\mathrm{SGS}, s_\mathrm{L}$ and Σ denote the density conditioned upon the unburned state, SGS eddy viscosity, laminar burning velocity and sub-grid flame surface density, respectively. For diffusion modeling, a unity Lewis number is assumed. A gradient assumption is used for turbulent flux closure, with the turbulent Schmidt number set to $\mathrm{Sc}_\mathrm{SGS} = 0.4$. The combustion process is initiated by imposing a sphere of burned state ($\widetilde{c} = 1$) in the spark plug gap at the respective numerical spark timing.

The passive scalar Y_EGR accounts for the burned gas mass fraction of the previous cycle and a respective transport equation is solved. Prior to exhaust valve opening (EVO), $\widetilde{c}$ is mapped to Y_EGR and reset to zero [89]. During the simulation, the state $\boldsymbol{\varphi}$ is used to access the tabulated manifold. Transport and thermodynamic data are determined by the extracted species composition. Further, the tabulated unburned density and the laminar burning velocity are used in Eq. (2.35) and for determining Σ in the FSD model [88]:

$$\Sigma = \left[1 + 0.46\mathrm{Re}_\mathrm{SGS}^{0.25}\left(\frac{u'_\mathrm{SGS}}{s_L}\right)^{0.3}\left(\frac{p}{p_0}\right)^{0.2}\right]\left|\frac{\partial\widetilde{c}}{\partial x_i}\right|\,, \tag{2.36}$$

where Re_SGS and u'_SGS are turbulent Reynolds number and unresolved turbulent velocity fluctuation, respectively. The reference pressure p_0 is 0.1 MPa.

For the analyses described in Chapter 6, the combustion progress during the engine cycle is expressed in terms of the fuel mass fraction burned (MFB):

$$\mathrm{MFB} = \frac{\int\overline{\rho}\widetilde{c}\mathrm{d}V}{\int\overline{\rho}\mathrm{d}V}\,. \tag{2.37}$$

The unburned mass is calculated from the initial mass, $m_{\mathrm{u},0}$, and the MFB:

$$m_{\mathrm{u}} = m_{\mathrm{u},0} \cdot (1 - \mathrm{MFB})\,. \tag{2.38}$$

2.2.2. Turbulent auto-ignition modeling

In this thesis, the auto-ignition process is modeled with a precursor model. First, the existing model is described and then modifications conducted are outlined.

Generalized Knock Integral Method

The generalized Knock Integral Method (gKIM) was introduced by Linse et al. [53]. Using the precursor formaldehyde CH_2O, global experimental knock trends were properly captured in isooctane-based simulation studies [A1, 53]. Since the gKIM model is based on RANS, it does not provide cycle-individual auto-ignition predictions. Instead, it provides auto-ignition probabilities based on a presumed PDF approach to account for turbulence-chemistry interaction (TCI). With the objective of this thesis to investigate cycle-to-cycle variations of knocking combustions, this statistical approach is not sufficient (cf. [A1]) and therefore modifications were introduced, which are discussed in the following.

Modifications introduced in this thesis: *detailed gKIM*

Following Linse et al. [53], the auto-ignition process is modeled as a process separated from the turbulent flame (see Figure 1.1). For that, a precursor is used to track the auto-ignition process in the unburned mixture [A1]. In this thesis, the fuel consumption is used as a pseudo precursor species and determines the auto-ignition progress variable conditioned on the unburned state $Y_{\mathrm{c_{I,u}}}$. The transport equation of $Y_{\mathrm{c_{I,u}}}$ in the LES-context reads:

$$\frac{\partial(\overline{\rho}\widetilde{Y}_{\mathrm{c_{I,u}}})}{\partial t} + \frac{\partial \overline{\rho}\widetilde{u}_i \widetilde{Y}_{\mathrm{c_{I,u}}}}{\partial x_i} = \frac{\partial}{\partial x_i}\left[\left(\overline{\rho}D + \frac{\mu_{\mathrm{SGS}}}{\mathrm{Sc_{SGS}}}\right)\frac{\partial \widetilde{Y}_{\mathrm{c_{I,u}}}}{\partial x_i}\right] + \overline{\rho}\widetilde{\dot{\omega}}_{Y_{\mathrm{c_{I,u}}}}\,. \tag{2.39}$$

Here, a gradient assumption with a turbulent Schmidt number of $\mathrm{Sc_{SGS}} = 0.4$ is used for turbulent flux closure, and diffusion modeling assumes a Lewis number of unity.

The closure of this model is based on the determination of the unknown source term $\dot{\omega}_{Y_{\mathrm{c_{I,u}}}}$ from a flamelet-based auto-ignition manifold, which is generated based on homogeneous reactor calculations with the in-house solver *ULF* [90]. The in-house code *pyFLUT* is used to vary the pressure p, the unburned temperature T_{u} and the EGR mass fraction Y_{EGR} (see Table 2.2). The mixture fraction is set to its stoichiometric value. With the unburned temperature T_{u} mapped to the normalized enthalpy h_{norm}, the thermo-chemical state is parametrized as $\varphi_{\mathrm{I}} = \varphi_{\mathrm{I}}(Z, Y_{\mathrm{c_{I,u}}}, p, h_{\mathrm{norm}}, Y_{\mathrm{EGR}})$,

The source term $\dot{\omega}_{Y_{\mathrm{c_{I,u}}}}$ of Equation 2.39 is calculated based on the temporal evolution of $Y_{\mathrm{c_{I,u}}}$ in the respective homogeneous reactor calculation. In previous works [A1, 53], a linearization has been used for the source term modeling. Following Livengood and Wu [48], it is assumed that the auto-ignition progress variable increases linearly until auto-ignition. With that, the source

Table 2.2.: Parameter variation of auto-ignition manifold

Parameter	min. value	max. vale	# steps
p	$0.8\,\mathrm{bar}$	$70\,\mathrm{bar}$	18
T_u	$300\,\mathrm{K}$	$1000\,\mathrm{K}$	23
Y_EGR	0	1	10

term is given by the reciprocal of the auto-ignition delay time τ:

$$\dot{\omega}_{Y_{\mathrm{c_{I,u,lin}}}} = \frac{1}{\tau}\,. \tag{2.40}$$

This model is referred to as *linear gKIM* in the following.

As a modification introduced in this thesis, the detailed non-linear auto-ignition evolution is captured in the source term. Similar to existing modeling approaches, e.g., the TKI model [47], the source term is defined by the respective instantaneous reaction rates of the auto-ignition progress variable[1]:

$$\dot{\omega}_{Y_{\mathrm{c_{I,u,det}}}} = \frac{\partial Y_{\mathrm{c_{I,u}}}}{\partial t}\,. \tag{2.41}$$

This model is referred to as *detailed gKIM* in the following[2].

In the post-processing, the conditional auto-ignition progress variable is normalized to $c_\mathrm{I,u} = Y_{\mathrm{c_{I,u}}}/Y_{\mathrm{c_{I,u,max}}}$, where $Y_{\mathrm{c_{I,u,max}}}$ is the value after auto-ignition. With that, the auto-ignition progress variable is retrieved from $c_\mathrm{I} = (1-c)\cdot c_\mathrm{I,u}$. Assuming that no auto-ignition can occur in the burned gas [53], this takes into account the turbulent flame propagation modeled by the normalized combustion progress variable c. Finally, the set Ω_crit, representing all computational cells that exhibit a critical auto-ignition state, is defined by $c_\mathrm{I} \geq \varepsilon = 0.95$ in this work. In accordance with [A1], the mass represented by these cells is referred to as critical mass m_crit hereafter and assumed to undergo auto-ignition.

[1] This formulation is evaluated based on a DNS dataset as described in Section A.1

[2] Section 5.3 discusses the direct comparison of the two source term formulations for representative operating conditions studied in this thesis. Figure 5.14 gives a visual impression of the Livengood-Wu assumption.

3. Experimental configurations[1]

The experimental database used throughout this thesis is provided by the Chair of Thermodynamics of Mobile Energy Conversion Systems (TME) at the RWTH Aachen University. This data subsequently serves as initial and boundary conditions for the numerical simulations performed. The joint analysis of the experimental and numerical results is a crucial part of the subsequent investigations.

A single-cylinder research engine (SCRE) is employed for the experimental investigation of knocking combustion. The respective geometry and measurement procedure are introduced in Section 3.1. Thereafter, the processing of recorded signals is discussed in Section 3.2. Finally, the main properties of the different surrogate fuels investigated are outlined in Section 3.3

3.1. Experimental database

The experimental database consists of two measurement campaigns, where the second extends the investigation through the utilization of a fiber-optical spark plug. All experiments are conducted employing a full-metal SCRE. More details on the engine can be found in previous studies [91–93].

3.1.1. Geometry and boundary conditions

The knocking behavior of the investigated fuels (see Section 3.3) is investigated in the SCRE under stoichiometric operating conditions. To ensure a homogeneous mixture inside the cylinder, port-fuel injection (PFI) is used. This avoids possible interference caused by direct injection, e.g. mixture inhomogeneities or local temperature differences due to different latent heats of vaporization. The engine geometry and operating conditions are listed in Table 3.1. A schematic visualization of the combustion chamber and the fiber-optical spark plug is given in Figure 3.1.

[1] Parts of this chapter are taken from the publication by Kircher et al. [P1] which was created during the work on this thesis. In this, I was the main author. The experiments were conducted by my co-author Jonathan Schneider at TME, RWTH Aachen University. He contributed as the author of technical descriptions of the measurement setup and procedure.

Table 3.1.: Engine geometry and operating conditions.

Parameter	Value
Stroke	90.5 mm
Bore	75 mm
Compression ratio	11.83:1
Number of valves	2/2
Max valve lift	8 mm
Valve angle	22.5°
Valve diameter (IV/EV)	32/26 mm
Intake air pressure	ambient
Exhaust air pressure	ambient
Ambient air pressure	1013 mbar
Oil and coolant temp.	90° C

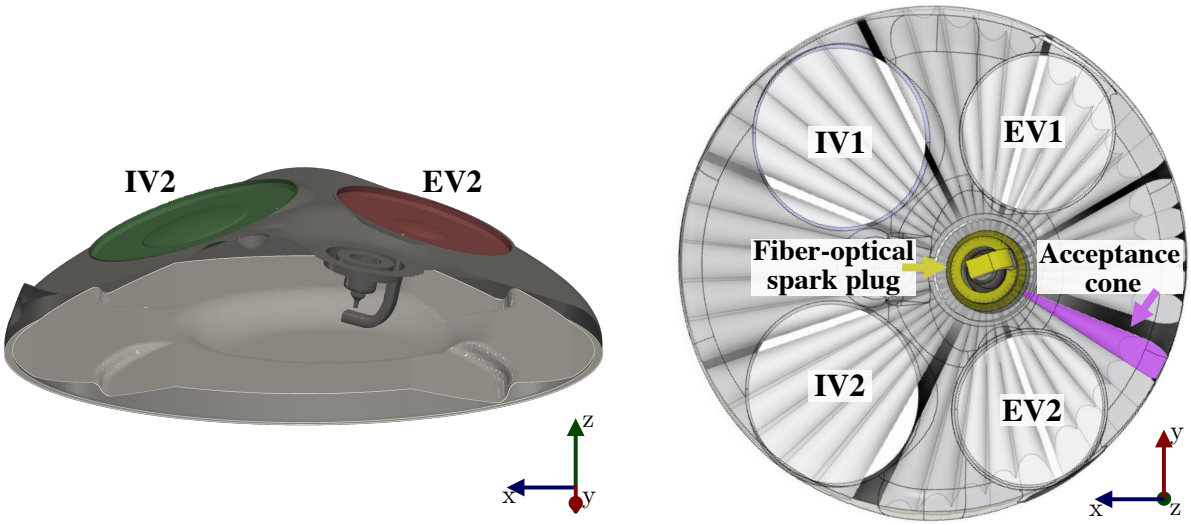

Figure 3.1.: The left side shows the combustion chamber geometry close to TDC. The cylinder head is cut at the symmetry plane. On the right side, the fiber-optical spark plug of the second measurement campaign is schematically depicted. The 40 optical acceptance cones are shown in transparent gray. Intake valves (IV) and exhaust valves (EV) are labeled for orientation.

3.1.2. Measurement setup

The pressure in the cylinder is measured with two flush-mounted KistlerA6061B piezoelectric pressure transducers opposite each other in the combustion chamber roof between the intake and exhaust valves. Two transducers are used for redundancy. The pressure values given refer to the average of both pressure transducers. The pressures in the intake and exhaust manifolds are measured with Kistler 4045-A5 piezoresistive pressure transducers. The position of the crankshaft is measured with an optical encoder with a 0.1° CA resolution. The measurement signals are processed via Kistler 5064 charge amplifiers and an FEV combustion analysis

system (FEVIS). Coolant and oil temperatures are conditioned to 90° C. The engine is coupled to an eddy-current brake and an electric dynamometer to maintain the desired engine speed with an accuracy of ± 1 r/min, regardless of the engine load. The intake air mass flow is measured via a hot-film air mass meter. To ensure constant stoichiometric engine operation the relative air/fuel ratio λ of the exhaust gas is derived according to Spindt [94] with the extension for oxygenated fuels by Bresenham et al. [95]. Static pressures and all temperatures are averaged over a 30-second time period.

For a second measurement campaign, the same engine is provided with optical access through the insertion of a 40-channel fiber-optical spark plug produced by AVL List GmbH. The combustion chamber geometry with the optical acceptance cones of the 40 optical channels is shown in Figure 3.1. The optical data are acquired with a S1336-BQ photo-multiplier array from Hamamatsu Photonics. The spectral characteristics of the fiber system are only limited by the photomultiplier's spectral photosensitivity, which allows the detection of broadband light emission between 200–1100 nm with a peak sensitivity at 950 nm. The processing of the optical signals is described in Section 3.2.2

3.1.3. Operating conditions

Two reference operating points (OPs), OP1500 and OP2500, are defined with different engine speeds. These engine OPs are chosen to investigate the knock onset and the influence of engine speed for all four fuels under similar boundary conditions and are listed in Table 3.2. Identical valve timings of intake valve opening (IVO; 15° CA aTDC) and exhaust valve closing (EVC; -26° CA aTDC) at 1 mm lift are chosen for both OPs. This minimizes valve overlap and internal exhaust gas recirculation (EGR) rate, which is around 4%.

Table 3.2.: Operating point definition.

Parameter	OP1500	OP2500
Engine speed / r/min	1500	2500
IMEP / bar	10	
IVO / ° CA aTDC	15	
EVC / ° CA aTDC	-26	
Spark timing	var.	

3.1.4. Measurement procedure

The focus of this work is the investigation of knocking combustion behavior at the knock limit. Accordingly, spark timing sweeps are conducted to vary the combustion phasing in terms of 50% fuel mass fraction burned (MFB50), to investigate the onset of knock.

Starting from a spark timing well below the knock limit, the spark timing is incrementally advanced, which shifts the center of combustion (MFB50) forward and increases cylinder pressure and maximum temperature. Therefore, the likelihood of auto-ignition increases. Two

spark timings ($ST_{low} = -3°$ CA aTDC and $ST_{high} = -6.5°$ CA aTDC) are exemplarly shown in Figure 3.2 (Operating point is OP1500, see Section 3.1.3). For each spark timing, 20 exemplary single-cycle pressure traces are plotted, as well as the resulting mean pressure trace.

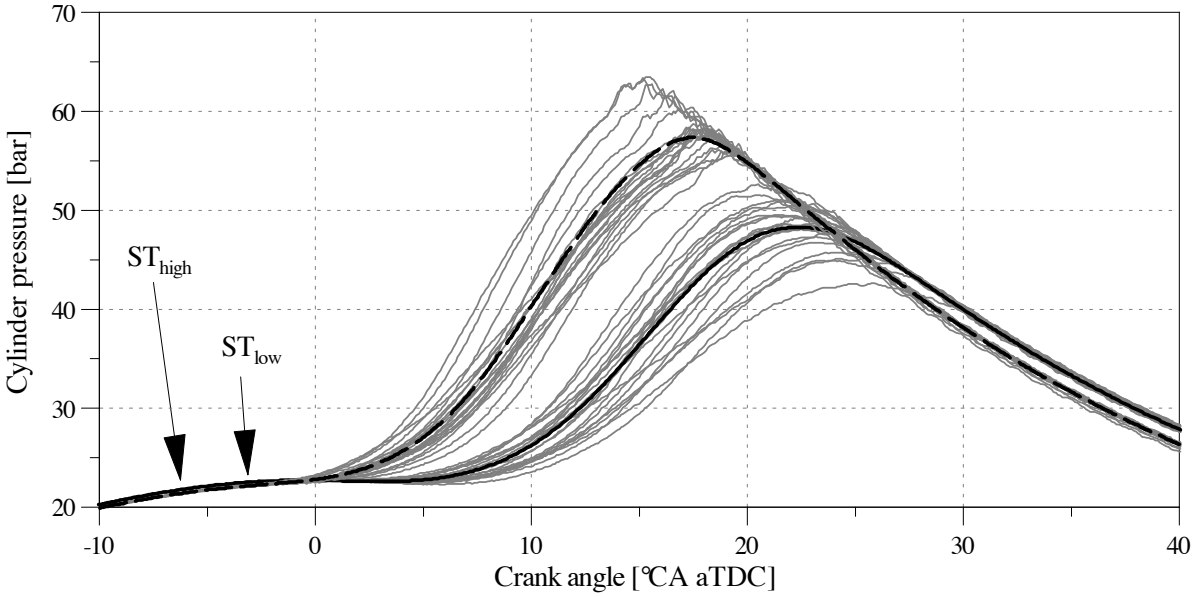

Figure 3.2.: Measurement procedure: spark timing sweep at the knock limit

For ST_{low}, only a few knocking cycles with a low amplitude of the pressure oscillation are recorded. At ST_{high} the mean peak pressure position is advanced, the peak pressure is higher and almost all cycles show significant pressure oscillations. Due to possible engine damage, the increasing pressure oscillations set a limit to the advance of the spark timing. For the different spark timings, the engine load is kept constant by adjusting the intake manifold pressure. Due to the characteristic cycle-to-cycle variations (CCV) in each operating condition, suitable auto-ignition conditions are not reached for every cycle, but rather only for the fastest burning cycles with the highest cylinder pressures and temperatures. Therefore, the knock-relevant quantities, discussed in the next section, are retrieved by considering all the 1000 recorded cycles for each operating condition. To compare the knock behavior of the fuels investigated (see Table 3.3), different spark timings are chosen for each fuel to achieve similar knock intensity levels. This in turn leads to different thermodynamic conditions, which have to be considered when interpreting the results. Although the same reference operating conditions are used for both measurement campaigns, the individual spark timings of the spark timing sweeps performed differ slightly for comparable knock intensities.

3.2. Experimentally obtained knock quantities

Investigation of the knocking combustion behavior is mainly based on the pressure sensor-related signals. The respective quantities are described in the following. Additional information is available based on the signals of a fiber-optical insert and the respective processing is discussed in Section 3.2.2. However, this data is only available for the second measurement campaigns (see Section 3.1)

3.2.1. Quantities based on pressure sensor signals

All pressure-based quantities are obtained from the recorded 1000 individual cycles per operating point and discussed in the following.

Peak pressure & pressure rise

Since cylinder pressure is a key factor influencing auto-ignition, the average maximum cylinder pressure and the maximum rate of pressure rise are calculated from the pressure transducer signal.

Heat delay & heat duration

To calculate the heat release rate, the high-resolution pressure trace is further analyzed in a detailed offline model based on the Rassweiler and Withrow method [96] using the FEVIS system. The polytropic coefficients of compression and expansion are fitted to the individual pressure traces of the combustion cycles. This enables the calculation of the MFB from the pressure data, providing key parameters such as the crank angle at MFB50, the heat delay, calculated from spark timing to MFB10, and the heat duration, calculated from MFB10 to MFB90.

Knock intensity

The auto-ignition of the unburned mixture induces high-frequency pressure oscillations that superimpose the mean pressure trace in the cylinder. Thus, the high-resolution pressure trace is used to characterize knock intensity, as depicted in Figure 3.3. First, the high-frequency part of the pressure trace is separated from the low-frequency part by a weighted moving average low-pass filter. Subsequently, from the filtered high-frequency component of the cylinder pressure p, which is calculated by subtracting the low-pass filtered signal from the unfiltered signal, the characteristic value Knock-Peak-Peak (KPP) can be determined. Based on all cycles in one operating condition, the average value $\mathrm{KPP}_{\mathrm{mean}}$ can be calculated.

Variation of knock intensity

The standard deviation of KPP (σ_{KPP}) is calculated from the variance of the cycle-individual KPP values in each operating condition. Therefore, it can be used as a parameter describing the cyclic variations in knock intensity.

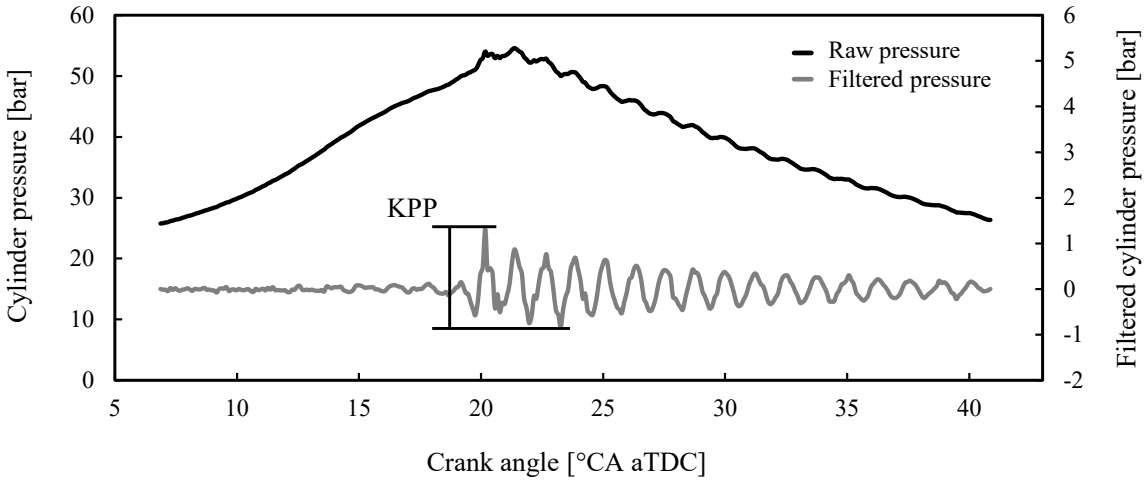

Figure 3.3.: Example of a single cycle raw pressure trace with the corresponding filtered pressure trace and the parameter KPP.

3.2.2. Determination of knock initiation direction based on fiber-optical signals

The optical signals of the fiber-optical spark plug are processed in addition to the available pressure signals. In a direct localization of the knock origin, intensity peaks caused by auto-ignition events are tracked. The measurements conducted in the scope of this thesis use an indirect localization approach. The respective methodology first described in [A2] allows a robust knock origin determination for operating conditions with low knock amplitudes. Here, the individual signals of each optical acceptance cone are stacked vertically which leads to a transformation in the image space and enables the application of image processing algorithms. In addition, oscillation mode analysis is used to identify the most probable direction of knock initiation. This discretizes the knocking direction into 40 bins in the circumferential direction, which corresponds to the 40 optical acceptance cones (see Figure 3.1). Thus, in addition to the global information provided by the pressure signal, local information is available to further characterize the observed knock event.

3.3. Properties of investigated single and multi-component surrogate fuels

For the experimental investigation of knocking combustion research grade RON95E10 gasoline is used as the reference fuel. In addition, three surrogate fuels are being studied, one single-component and two multi-component. The selection of surrogate fuels captures a variation in compositional complexity as well as expected knock resistance. The suitability as a reference surrogate fuel for knock investigations can be determined in comparison with RON95E10. The characteristic parameters of the fuels are listed in Table 3.3.

Table 3.3.: Characteristic parameters and composition of the fuels under investigation.

Parameter	RON95E10	Isooctane	TRF-E10	TRF-OS
RON / -	96.4	100	96.6	95.3
MON / -	86.3	100	88.3	92.6
OS / -	10.1	0	8.3	2.7
H/C / -	1.87	2.25	1.93	2.07
ρ / kg/m^3	739.9	690	739.6	714.6
Ethanol / mass-%		-	9.8	5.3
Toluene / mass-%		-	30.3	17.4
Heptane / mass-%		-	13.4	11.3
Isooctane/ mass-%		100	46.3	66

The first surrogate fuel selected is isooctane, a commonly used single-component surrogate fuel for knock investigations. With a RON and MON of 100 by definition, isooctane is expected to show a higher knock resistance than the reference RON95E10.

In addition, two TRFs are investigated in this study. The first, TRF-E10, is based on an experimental and numerical study [86]. The composition has been optimized to match well with RON95E10 in terms of RON, MON, H/C and aromatic content. The auto-ignition delay times were found to be consistent with RON95E10 measurements [86]. Therefore, TRF-E10 is expected to have a similar knock behavior as the reference RON95E10.

The second, TRF-OS, is chosen to investigate the influence of octane sensitivity (OS), which is related to the change in reactivity with pressure and temperature [10]. TRF-OS is based on a study by Kim et al. [28], in which the two-stage auto-ignition behavior and OS of four-component TRFs were investigated. Previous studies have found that fuels with similar RON, but higher OS, show higher knock resistance [97–99]. With a similar RON to RON95E10 but a significantly lower OS, TRF-OS is expected to show lower knock resistance in comparison.

Auto-ignition delay times

The surrogate fuels are further characterized by analysis of the auto-ignition delay times based on 0-D homogeneous reactor calculations performed with the in-house solver *ULF* [90]. A detailed mechanism developed for the TRF-E10, which considers 485 species and 2081 reactions [86], is used to perform the calculations for all surrogate fuels at stoichiometric mixture. The sensitivity of the auto-ignition delay times to the unburned temperatures T_u and the pressures p is depicted in Figure 3.4. Isooctane is shown on the left side, TRF-E10 in the middle and TRF-OS on the right side. All three surrogate fuels show a distinct NTC regime for the thermodynamic conditions investigated, with the auto-ignition delay times increasing between approximately 750 K and 850 K. The respective limits of the NTC regime are highlighted by dashed lines. The NTC limits of isooctane and TRF-OS show a similar range. For TRF-E10, the NTC regime narrows considerably with increasing pressure and finally disappears at the highest pressures investigated. Isooctane and TRF-OS show higher pressure sensitivity than TRF-E10, resulting in a wider range of auto-ignition delay times in the NTC range. In summary, the differences observed here are nevertheless not very pronounced.

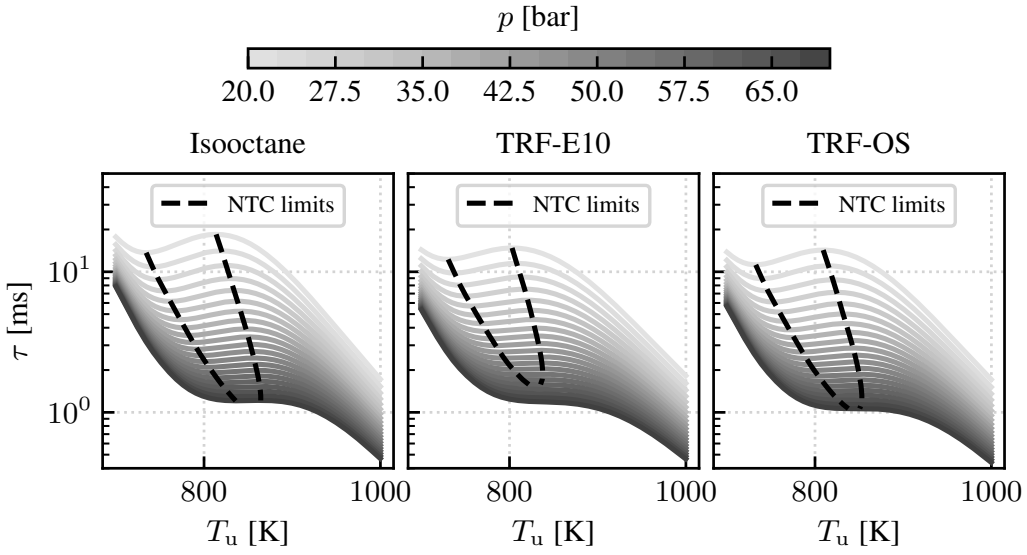

Figure 3.4.: Influence of unburned temperature T_u and pressure p on auto-ignition delay times τ of stoichiometric mixtures. Isooctane shown on the left side, TRF-E10 in the middle and TRF-OS on the right side. The NTC limits are depicted as dashed lines.

4. Numerical setup

The simulations in this thesis can be loosely separated into 0-D/1-D simulations (for the generation of the combustion and auto-ignition manifolds as discussed in Section 2.2) and 3-D engine simulations, which are discussed in Chapter 6. The framework for the latter is described in the following.

4.1. Engine simulation framework

The 3-D engine simulations are performed using *TFMotion* which is an *OpenFOAM*-based framework developed for engine simulations as described in [100]. The interface between the 3-D simulations and the chemistry manifolds is based on a memory abstraction layer [101], which is included in the *pyFLUT* software package.

4.1.1. Topological changes and mesh generation

The four strokes of the gasoline engine involve the movement of the piston and the valves. These are captured by moving the respective boundaries of the computational grid. This movement is transferred to the whole grid via a Laplacian deformation, where the diffusivity is proportional to the distance from the wall. To capture the movement over the whole engine cycle the *key grid* approach is applied [102]. In a pre-processing step, a key mesh is generated for a specific crank angle. In the following, the motion of parts is prescribed, and the mesh deforms accordingly, which results in a distortion of the computational cells. To prevent bad mesh quality, a new key mesh is generated when a certain distortion is reached. During the full-cycle engine simulation runs, results are mapped from one key mesh to another. The meshes are hexa-dominant structured grids (see Figure 4.1) generated using *snappyHexMesh*. The base cell size in the cylinder is $0.5\,\mathrm{mm}$, which is comparable to other LES studies presented in the literature, e.g., [20, 25, 64, 103]. For the intake and exhaust pipe region, the cell size is increased to $1.0\,\mathrm{mm}$. To capture geometric features, a local refinement down to $0.125\,\mathrm{mm}$ is applied. The same refinement level is used for a sphere of $2\,\mathrm{mm}$ around the spark position (see inlay of Figure 4.1). The maximum number of cells is approximately 5.9 million at the bottom dead center. For computational efficiency, the mesh regions of the intake and exhaust pipes are removed from the main simulation as soon as the respective valve is closed. The pipe simulations are then continued separately and mapped back onto the main simulation when the respective valve re-opens.

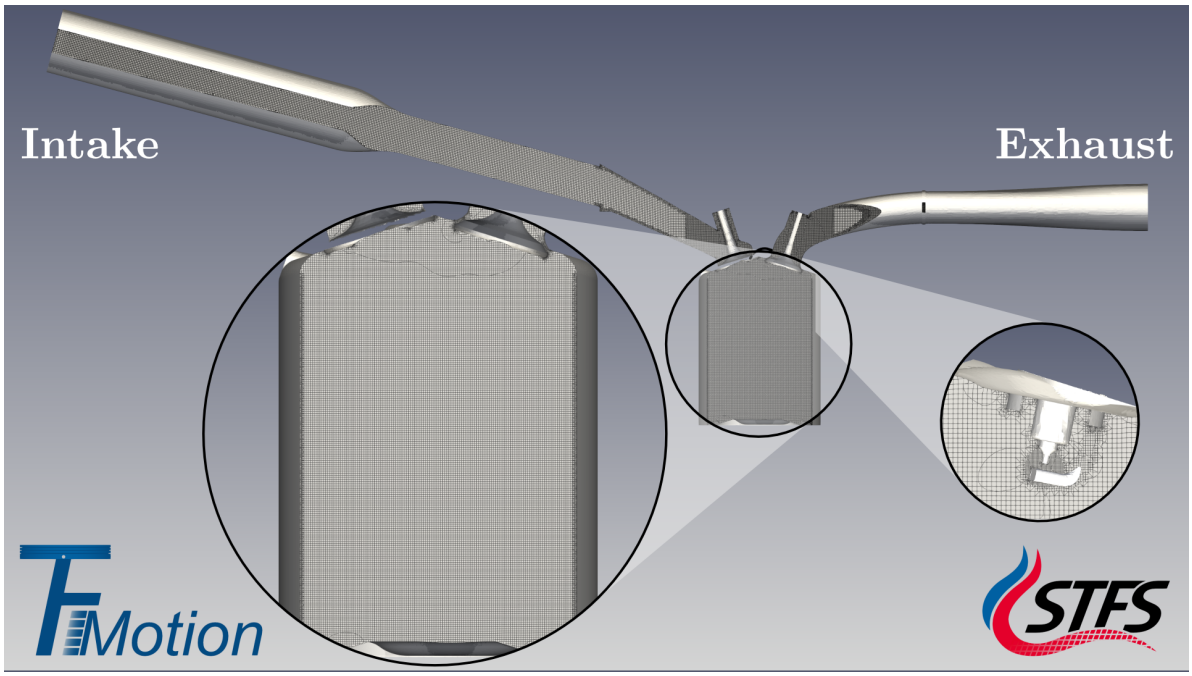

Figure 4.1.: Engine geometry and mesh for an engine timing within the exhaust phase. The large inlay shows a zoom of the mesh within the cylinder on the valve plane. The small inlay depicts a zoom of mesh region around the spark plug on the tumble plane.

4.1.2. Multi-cycle procedures

The results of the two multi-cycle LES studies are discussed in Section 6. A pre-initialization is used consistently, in which the simulation is started in the early exhaust phase. The composition and temperature of the quiescent mixture in the cylinder and the exhaust port are set according to a burned state. The simulation of the first gas exchange phase and the compression stroke is used as the initial condition for the first combustion simulation in *Cycle 0* (see Figure 4.2). Subsequently, the multi-cycle strategy differs[1].

For the simulations discussed in Section 6.1, the combustion LES of *Cycle 0* matches the experimentally obtained mean pressure trace. The subsequent gas exchange provides the initial conditions for *Cycle 1*. Here, different mass-burning rates are achieved through a variation in the numerical spark timing.

For the multi-cycle LES study discussed in Section 6.2, the complete procedure shown schematically in Figure 4.2 applies. The numerical spark timing is varied to obtain different pressure traces in *Cycle 0*. From this, three individual results, which differ in peak cylinder pressure (see blue, orange and dark grey line), are selected as initial conditions for *Cycle 1*. With the subsequent gas exchange, the initialization procedure is completed resulting in three initial

[1] In addition, adjustments are applied to the combustion simulation framework based on parameter variation studies. The corresponding discussion can be found in Section A.2.

conditions for *Cycle 2*. Due to the initialization procedure only results from *Cycle 2* onwards are considered in the analyses. The full-cycle simulations within each thread are independent of the other threads and are therefore executed in parallel. This reduces the processing time compared to a fully consecutive multi-cycle LES.

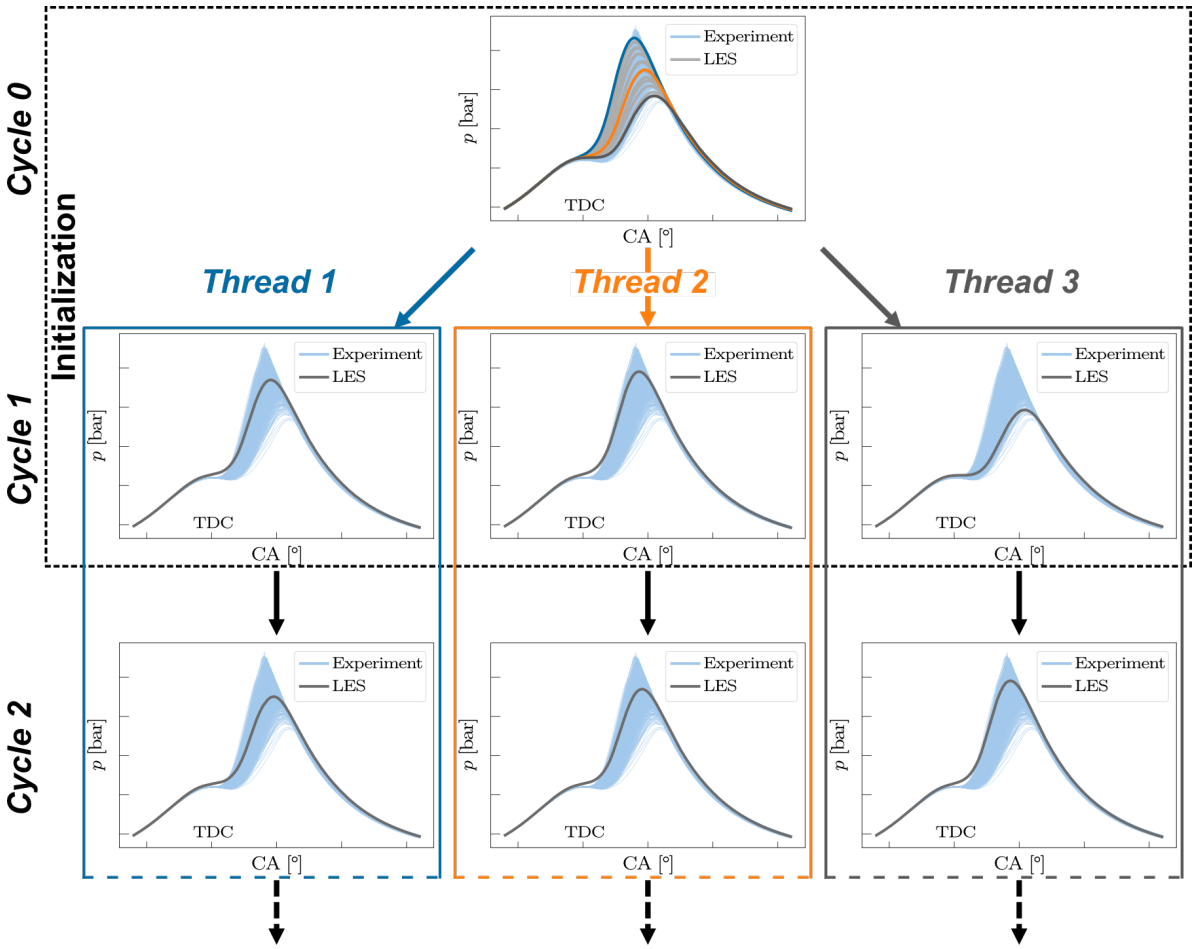

Figure 4.2.: Schematic visualization of the multi-cycle approach discussed in Section 6.2. *Cycle 0* and *Cycle 1* represent the initialization procedure. The pressure traces of *Cycle 0*, which are selected as initial conditions for the individual threads, are highlighted in the respective color. The arrows and dashed lines shown below indicate the extension of each thread by further cycles.

4.1.3. Boundary conditions and solver settings

In agreement with the measurement position, the experimental intake and exhaust pressures are prescribed as *totalPressure* boundary conditions at the respective ends of the computational domain (see Figure 4.1). The wall temperatures are based on a conjugate heat transfer (CHT) simulation conducted by the experimental research partner and set as listed in table 4.1.

Table 4.1.: Wall temperature boundary conditions.

Component	Temperature
Intake duct	310 K
Intake port	363 K
Cylinder head	410 K
Intake valve stem	420 K
Intake valve bottom	500 K
Liner	380 K
Piston	420 K
Spark plug	800 K
Exhaust valve bottom	600 K
Exhaust valve stem	600 K
Exhaust port	400 K
Exhaust duct	400 K

The *engineFlameletFoam*-solver, developed within the *TFMotion*-framework, uses the finite volume method (FVM) for spatial discretization. The PISO algorithm is used in terms of pressure-velocity coupling. The simulation time is discretized with a first-order method. The time step ranges between $1 \times 10^{-6}\,\mathrm{s}$ and $1 \times 10^{-7}\,\mathrm{s}$, depending on the engine phase. The convective flux in the momentum equation is spatially discretized using a second-order upwind stabilized CDS. Convective scalar fluxes are discretized with a TVD scheme utilizing the Sweby limiter [104].

5. Analysis of knock characteristics of surrogate fuels[1]

The analysis of knocking combustion initiation in a spark ignition engine starts with the investigation of the global knock behavior. The experimental campaign (see Section 5.1) conducted by the research partners is used to investigate differences between surrogate fuels in comparison to gasoline. A model-based analysis investigates the fuel influence on combustion and auto-ignition as outlined in Section 5.2. Special focus is given to the NTC behavior and its potential influence on auto-ignition under knocking conditions. Subsequently, the influence of NTC behavior on the global auto-ignition process is investigated in detail for one of the surrogate fuels (see Section 5.3). Here, the auto-ignition modeling (see Section 2.2.2) is applied and validated.

5.1. Discussion of experimental database

The experimental configuration used in the following investigations has been described in Chapter 3. The operating points are defined in Table 3.2 and the investigated fuel properties are summarized in Table 3.3. The experimental knock quantities introduced in Section 3.2.1 are discussed in the following to characterize the knocking combustion behavior.

Analysis of OP1500

The experimental knock quantities of OP1500 are shown in Figure 5.1. The gasoline RON95E10, as the reference fuel, shows low $\mathrm{KPP_{mean}} = 0.47$ bar at $\mathrm{MFB50} = 14.3°$ CA, increasing with earlier spark timing to a maximum $\mathrm{KPP_{mean}} = 1.35$ bar at $\mathrm{MFB50} = 11.0°$ CA. The increase in knock intensity towards earlier MFB50 is exponential. With earlier MFB50, heat delay and heat duration decrease linearly, while pressure rise rate and peak cylinder pressure increase up to $p_{\mathrm{cyl}} = 60.9$ bar at $\mathrm{MFB50} = 11.0°$ CA. The standard deviation of $\mathrm{KPP_{mean}}$, σ_{KPP}, increases exponentially with earlier MFB50, similar to $\mathrm{KPP_{mean}}$, indicating increased CCV with earlier spark timings. In general, it is found that as the MFB50 decreases, the combustion process becomes shorter and higher pressures and mean knock intensities occur, as well as higher cyclic variations. This is observed for all tested fuels.

[1] This chapter is partly taken from the publications of Kircher et al. [P1, P2], which were created during the work on this thesis. In these, I was the main author of the parts used. My co-author Jonathan Schneider conducted the experiments and authored the corresponding discussion.

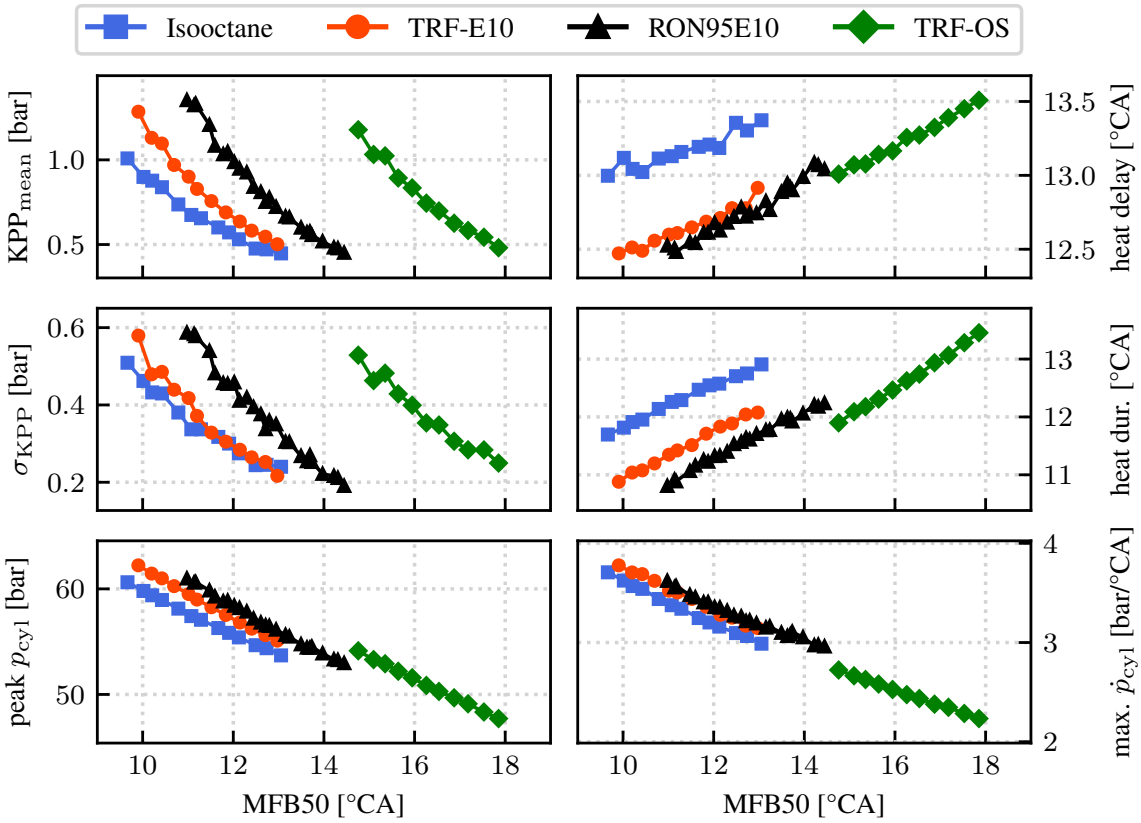

Figure 5.1.: Overview of the experimental knock quantities for the four fuels under investigation at OP1500 (see Table 3.2).

Regarding surrogate fuels, isooctane, as a single-component fuel, is discussed first. With a RON of 100 by definition, significant knock intensities occur only at very early spark timings and hence MFB50 with high cylinder pressures and rates of pressure rise. Thus, isooctane exhibits a high knock resistance, as expected. The combustion behavior of isooctane differs slightly from that of the RON95E10. The calculated heat delay and heat duration at comparable MFB50 are higher for isooctane because the cylinder pressure generally rises slower. To achieve the same MFB50, isooctane needs to be ignited earlier. The lower cylinder pressures correspond to a relatively slow heat release rate of isooctane. Due to these differences in combustion characteristics and the significantly higher knock resistance, isooctane can only be used to a limited extent as a surrogate fuel for knock investigations if a comparison is to be made with RON95E10.

TRF-E10 closely matches RON95E10 in terms of heat delay and heat duration, as well as peak pressure and pressure rise rate. For TRF-E10 comparable KPP values at only slightly earlier MFB50 ($\Delta < 1.5°$ CA) compared to RON95E10 are observed. The similar behavior in terms of knock onset and increase in KPP with ignition timing demonstrates that it is suitable as a surrogate fuel.

As expected, TRF-OS with the lowest RON is the least knock-resistant fuel. Comparable KPP values to those of RON95E10 are observed already at late MFB50 and therefore low peak cylinder pressures. However, reaching similar knock intensities at much less critical conditions is unexpected for TRF-OS given its individual composition. With a significantly higher content of isooctane and lower content of toluene, heptane and ethanol compared to TRF-E10, one would expect its knock behavior to be closer to that of isooctane. This suggests a strong non-linear dependence between the composition of the TRF and the knock resistance. Considering heat delay and heat duration, TRF-OS closely matches the values of isooctane, although at later MFB50, providing no further insight into this outlier behavior. Since the different thermodynamic conditions compared to the other fuels at identical knock intensity or MFB50 make further experimental analysis of TRF-OS difficult, an analysis beyond the experimental investigations is required. Therefore, a model-based analysis of the experimental results is performed and discussed after the results for OP2500 (see Section 5.2). Here, special emphasis is put into the analysis of NTC relevance for the operating conditions investigated, as previous experimental studies have shown a correlation of low OS with strong NTC behavior [33, 34, 105].

The standard deviation of KPP is directly proportional to the average KPP for all four fuels. With identical MFB50, eliminating the influence of combustion phasing on CCV in comparison, a significant influence of the fuel on σ_{KPP} similar to that on KPP is observed. TRF-OS reaches potentially destructive KPP values before reaching MFB50 values similar to those of the other fuels, thus no direct comparison can be conducted. However, since TRF-OS reaches the same levels of cyclic variability of knock intensity at later spark timings and therefore less critical conditions, the outlier behavior of TRF-OS becomes apparent. The peak cylinder pressure is shown to be fuel dependent both at identical combustion phasing, where it is lowest for isooctane and highest for TRF-E10, and at identical $\mathrm{KPP_{mean}}$, where it is highest for isooctane and lowest for TRF-OS. This again corresponds well with the order of knock resistance according to RON. The maximum rate of pressure rise appears to be less dependent on fuel composition than on MFB50.

Analysis of OP2500

In the following, the same knock quantities as before, but at a different engine speed, are discussed for OP2500 (see Table 3.2). The respective results are shown in Figure 5.2. The increased engine speed leads to higher flow velocities and reduced residence times. Relevant knock intensities only occur at earlier spark timings compared to those discussed for OP1500. As a result, for RON95E10, the MFB50 at which the mean knock intensity $\mathrm{KPP_{mean}} = 1$ bar is reached shifts by 2° CA forward from $\mathrm{MFB50} = 12.0°$ CA at $\mathrm{n_{engine}} = 1500$ r/min to $\mathrm{MFB50} = 10.0°$ CA at $\mathrm{n_{engine}} = 2500$ r/min. The magnitude of this shift in MFB50 can be considered as a relative increase in knock resistance as a function of engine speed and is similar for TRF-E10 (1.7° CA), but significantly higher for TRF-OS (3° CA) and isooctane (3.7° CA).

While the heat delay and heat duration for RON95E10, TRF-OS and TRF-E10 generally increase with higher engine speed, the heat delay of isooctane increases, but the heat duration decreases significantly. The longer heat delay is attributed to increased knock resistance. The lower heat duration indicates faster combustion and thus faster consumption of the end-gas volume which reduces the time available for the development of a potential auto-ignition. The strong

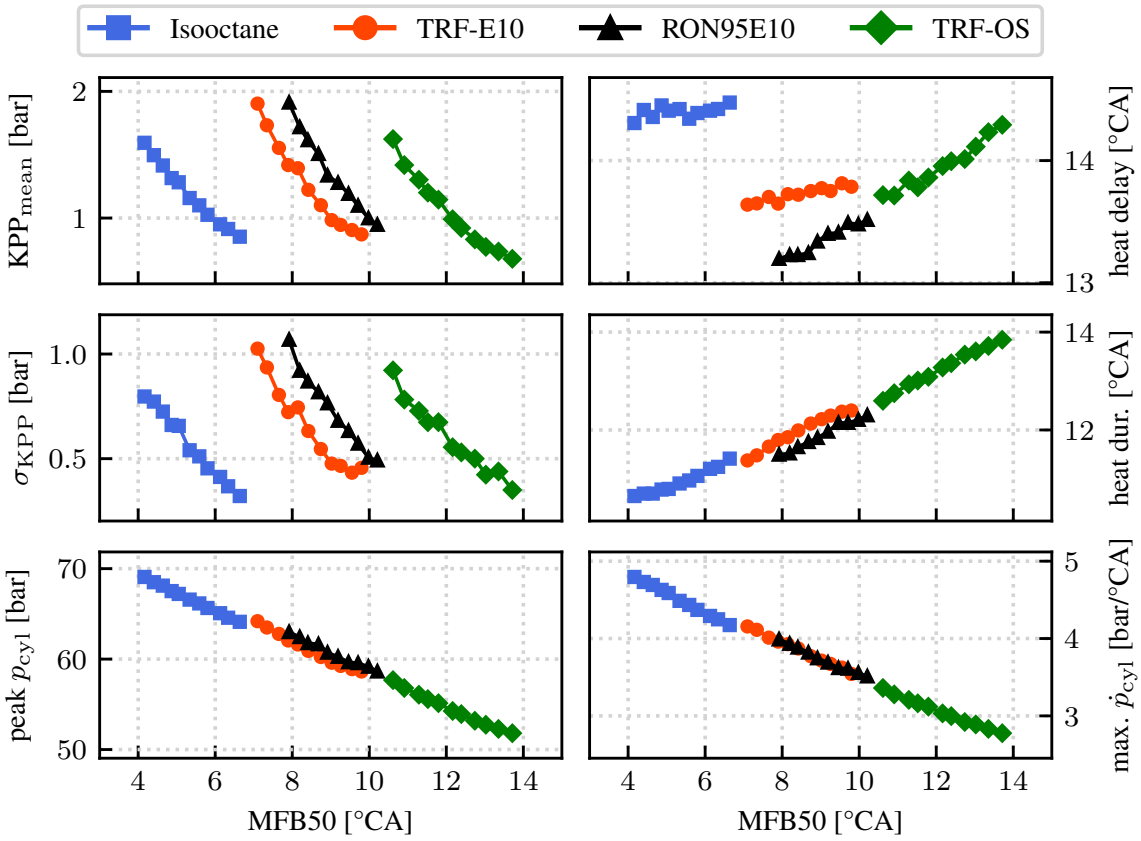

Figure 5.2.: Overview of the experimental knock quantities for the four fuels under investigation at OP2500 (see Table 3.2).

relative increase in knock resistance of TRF-OS results in knock behavior more similar to that of RON95E10 and TRF-E10 at OP2500. This also suggests an NTC influence in OP1500, which is investigated in the model-based analysis.

Similar to OP1500, TRF-E10 generally exhibits knock and combustion behavior very similar to RON95E10. They closely match in terms of heat duration, although combustion starts somewhat slower for TRF-E10, as indicated by the higher heat delay.

In summary, the experimental data show good agreement between the TRF-E10 surrogate and the RON95E10 for most relevant parameters at both engine speeds. As expected, the order of fuels in terms of knock resistance correlates with their respective RON at both operating points. Isooctane reaches the earliest MFB50 at comparable mean knock intensities due to its high knock resistance, which strongly increases with engine speed. Considering its composition, TRF-OS shows an unexpectedly low knock resistance for OP1500, increasing, however, for OP2500. As this is attributed to potential NTC influence, investigation of the NTC behavior of the fuels as a potential source of the different knock limits of the surrogate fuels is a particular aspect of the subsequently conducted model-based analysis.

5.2. Model-based analysis

For the model-based analysis, a reduced number of operating points of the experimental database (see Figures 5.1 and 5.2) is chosen. For every surrogate fuel, a late (LST), an intermediate (IST), and an early spark timing (EST) are investigated to cover the ranges of MFB50 and knock intensity. The selection aims for similar knock intensities of the fuels for the respective spark timings and is summarized in Table 5.1.

Table 5.1.: Summary of operating points investigated in the model-based analysis.

		OP1500		OP2500	
Fuel	Alias	MFB50 [°CA]	KPP_{mean} [bar]	MFB50 [°CA]	KPP_{mean} [bar]
Isooctane	LST	13.0	0.45	6.6	0.85
	IST	11.6	0.60	5.3	1.16
	EST	9.6	1.01	4.1	1.60
TRF-E10	LST	13.0	0.50	9.5	0.87
	IST	11.5	0.76	8.4	1.22
	EST	9.9	1.28	7.0	1.90
TRF-OS	LST	17.8	0.48	12.3	0.92
	IST	16.2	0.74	10.9	1.41
	EST	14.7	1.18	10.6	1.62

From a modeling perspective, knocking combustion is characterized by the two competing processes of flame propagation and auto-ignition (see Figure 1.1). By relating these to important fuel properties, namely the laminar burning velocity s_L of the mixture and the auto-ignition delay time τ, the influence of fuel chemistry can be investigated.

To retrieve the laminar burning velocities and auto-ignition delay times for the thermodynamic conditions of the operating points investigated, 1-D laminar freely propagating flame and 0-D homogeneous reactor calculations are performed. The same software is used that is also used to create the combustion and auto-ignition manifolds (see Section 2.2). In addition, the same detailed mechanism [86] is used for all surrogate fuels. As thermodynamic conditions, the average pressure of the measured 1000 cycles per operating point is used along with the unburned temperature and the global combustion progress retrieved from a pressure trace analysis with the *Three Pressure Analysis* (TPA) incorporated in the engine simulation tool *GT-Power*.

In further analysis of the experimental data, the fuel influence on the heat duration is investigated. Subsequently, the auto-ignition delay times are analyzed under the engine operating conditions. The section closes with a discussion of the NTC influence on a potential auto-ignition event.

5.2.1. Fuel influence on heat duration

The flame propagation speed inside an engine is influenced by the spark ignition in the initial phase of combustion, while heat transfer at the cylinder wall is important in the final phase. For the in-between interval, the flame propagates freely. Assuming similar turbulent intensities for all operating conditions, the laminar burning velocity s_L at MFB50 serves as an estimate for the flame propagation speed [106]. In Figure 5.3, the laminar burning velocity s_L is depicted, together with the experimental heat duration (see Figures 5.1 and 5.2) to investigate the fuel influence on the mass burn rate. This analysis is performed for all OPs (see Table 5.1), where the calculations of s_L are based on the pressures and unburned temperatures at the respective MFB50 (see Figure 5.4 (circles)).

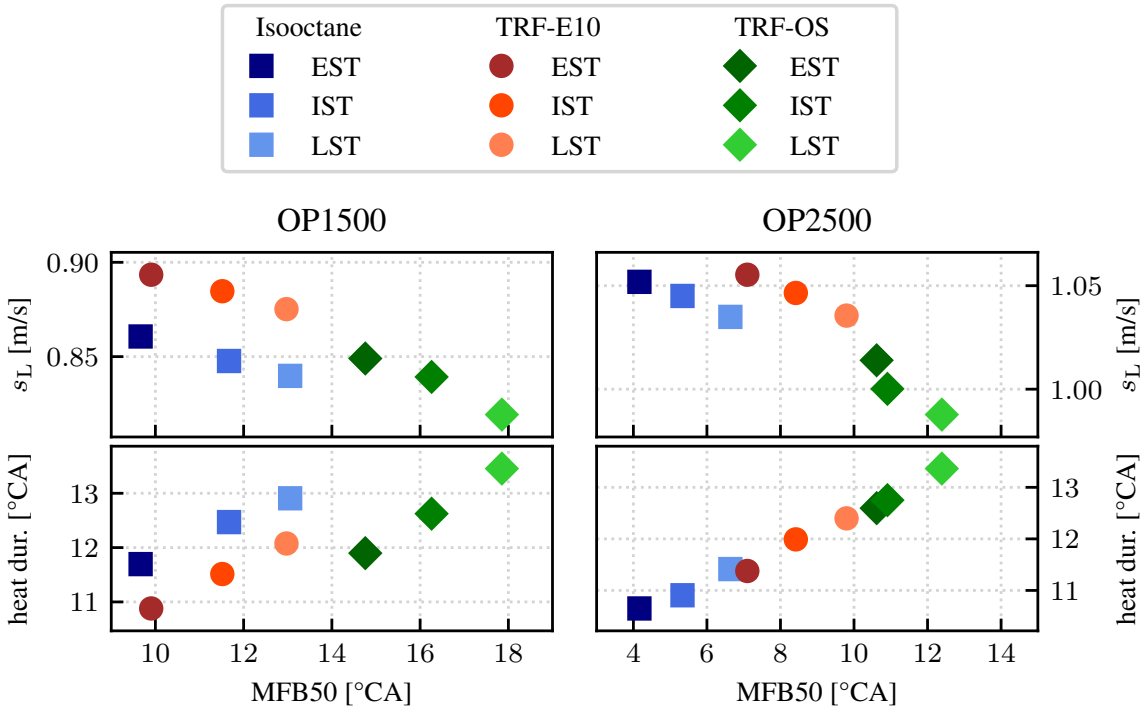

Figure 5.3.: Analysis of laminar burning velocity s_L and heat duration for OP1500 and OP2500.

The different knock limits of the fuels lead to different thermodynamic conditions at MFB50. For the individual fuels, an advance of the spark timing correlates with higher pressures and peak temperatures at MFB50 (see Figure 5.4 (circles)) leading to higher laminar burning velocities.

For OP1500, the TRF-E10 shows the highest s_L. This correlates well with the lowest heat duration, hence the cycle with the highest mass burn rate observed in the experiments. Isooctane shows slightly higher values of s_L than the TRF-OS, which matches with the lower heat durations. However, for the TRF-OS, a stronger decrease in s_L with later MFB50 is observed. This trend agrees with the steeper increase in the heat duration.

For OP2500, similar trends can be observed. The lowest s_L of the TRF-OS agrees well with the

longest heat duration. Isooctane shows a higher sensitivity to the engine speed than TRF-E10. As a result, the laminar burning velocities of these are similar at OP2500. However, in the case of isooctane, the heat duration is affected somewhat more by the change in engine speed than the laminar burning velocity.

In summary, the discussed correlations between laminar burning velocity and heat duration show the fuel influence on the mass burn rate.

5.2.2. Auto-ignition delay times under engine operation

The fuel influence on auto-ignition delay times under engine operating conditions is investigated for the unburned temperatures and pressures during the combustion process from MFB1 to MFB99. The potential relevance of the NTC regime is assessed by plotting these as trajectories in addition to the general sensitivity of the auto-ignition delay times τ to unburned temperature T_u and pressure p (see Figure 3.4). The analysis for all operating points as listed in Table 5.1 is depicted in Figure 5.4. Isooctane is depicted in the left column, TRF-E10 in the middle column and TRF-OS in the right column. The top row shows results for OP1500 and the bottom row for OP2500. The darkest color corresponds to the earliest spark timing and the lightest color to the latest spark timing. The center of the combustion process (MFB50) and MFB90 are marked for every trajectory. The onset of knock is located in the vicinity of the peak pressure in the experiments. For the OPs under investigation, this corresponds to approximately MFB85. Beyond MFB90, no knock initiation was detected in the experiments. Therefore, this interval is not discussed in the following.

As expected, the respective higher pressures and unburned temperatures resulting from earlier spark timings lead to lower auto-ignition delay times during combustion. The relative difference between the fuels correlates with the respective combustion peak pressure. At OP1500, TRF-E10 shows the highest peak pressure and thus the lowest auto-ignition delay times, TRF-OS has the highest auto-ignition delay times, and isooctane is between the other fuels. At OP2500, the generally earlier spark timing results in more critical thermodynamic conditions. The differences in auto-ignition delay times are larger due to the larger differences in peak pressure. Now, isooctane shows the lowest auto-ignition delay times, followed by TRF-E10 and TRF-OS.

The order of the auto-ignition delay times does not reflect the order of knock resistance observed in the experiments. While TRF-OS has the lowest knock resistance, it shows the highest auto-ignition delay times for the investigated operating points. Hence, no direct correlation of a lower knock resistance due to lower auto-ignition delay times can be drawn here. However, it is obvious that the thermodynamic conditions of all operating points during combustion are at least partially within the NTC regime. At OP1500, the trajectory of the latest spark timing (LST) of TRF-OS stays within the NTC regime until shortly before the end of combustion. For all other operating points, the tip of the trajectory between MFB50 and MFB90 is just outside the NTC regime. At OP2500, as a consequence of the higher T_u and p, a relevant part of the trajectories is beyond the upper NTC limit. However, the initial combustion phase is within the NTC regime for all fuels. Therefore, it is further analyzed how the NTC behavior can affect the auto-ignition process and potentially explain differences in the knock limit.

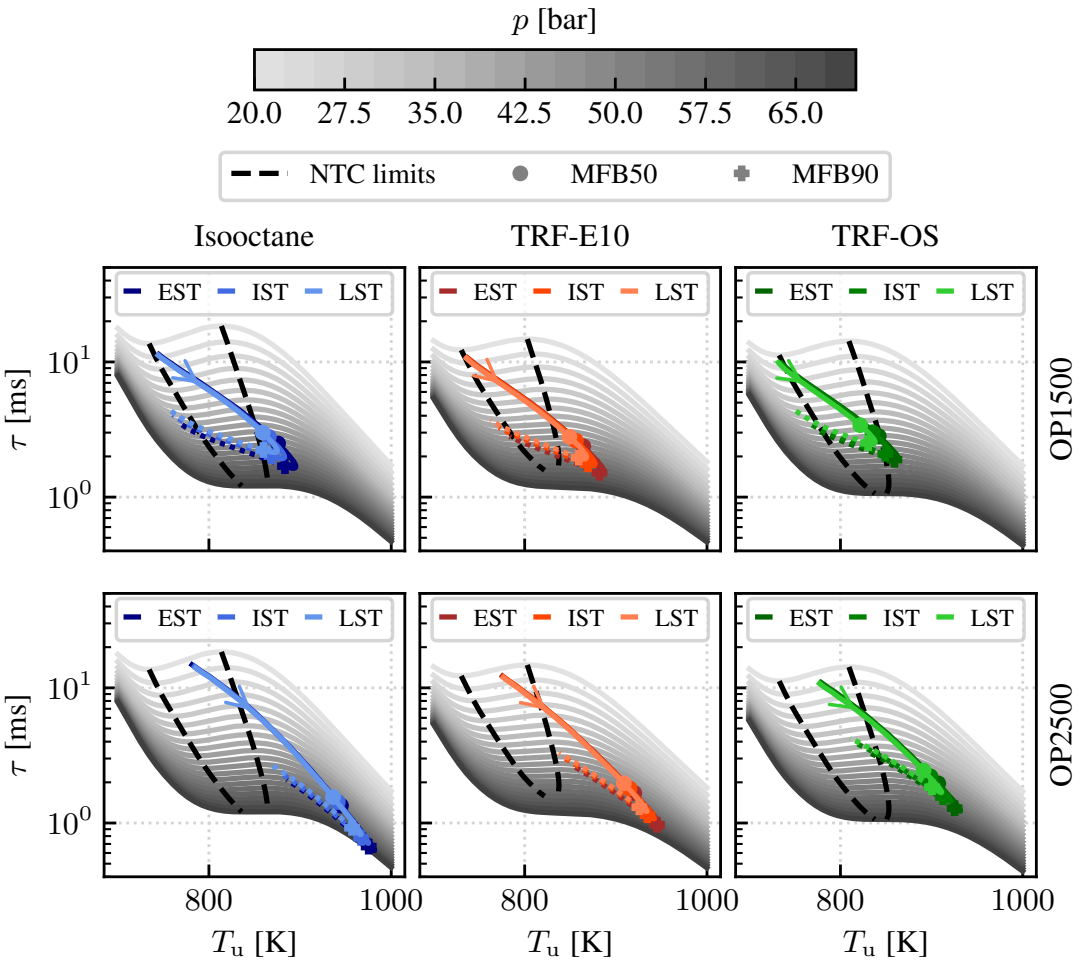

Figure 5.4.: Trajectories of thermodynamic conditions during combustion for isooctane (left), TRF-E10 (center), and TRF-OS (right). OP1500 is shown in the top row and OP2500 in the bottom row. The earliest ignition timing in each case is shown in a darker color, the latest in a lighter color.

5.2.3. NTC influence on auto-ignition

First, the influence of fuel chemistry on the auto-ignition process is discussed based on a 1-D hot spot configuration as commonly used in numerical auto-ignition studies [16, 35]. As values for the size of the hot spot and the magnitude of the temperature gradient are not known for the specific conditions, an exemplary hot spot is shown in Figure 5.5 to provide a more general assessment.

Within the hot spot radius ($x \leq 1$ cm), the temperature decreases linearly from the peak temperature $T_u = 920$ K to the uniform temperature of the surrounding $T_u = 860$ K, as shown by the solid black line. At a pressure of 40 bar, these temperatures are outside the NTC regime for the

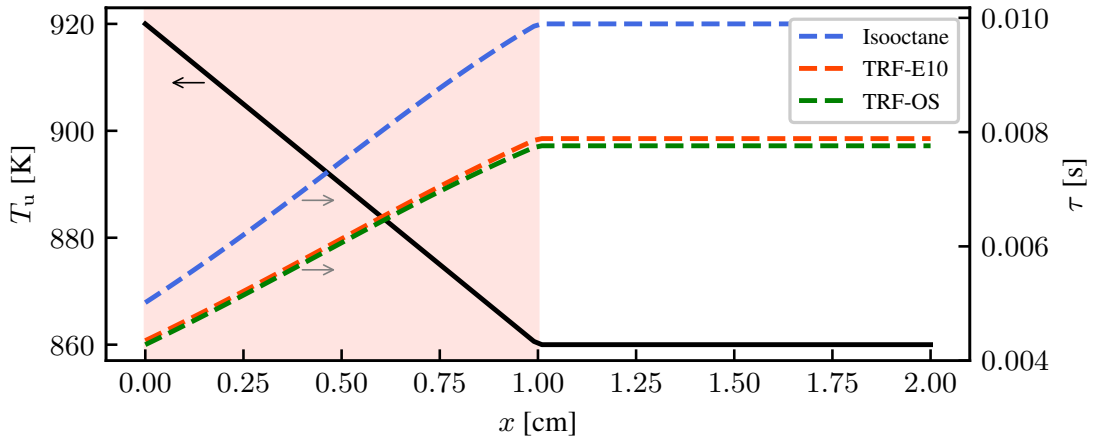

Figure 5.5.: Exemplary hot spot at p=40 bar defined by a linear temperature gradient within the interval highlighted in light red. Corresponding auto-ignition delay times of the three surrogate fuels are shown as dashed lines. Temperatures are outside the NTC regime for all three surrogate fuels.

surrogates investigated. The spatial gradient of the auto-ignition delay time $\partial\tau/\partial x$ results from the product of the spatial temperature gradient $\partial T_u/\partial x$ and the gradient of the auto-ignition delay times with respect to the unburned temperature $\partial\tau/\partial T_u$ (see Figure 3.4):

$$\frac{\partial\tau}{\partial x} = \frac{\partial T_u}{\partial x}\frac{\partial\tau}{\partial T_u}\,. \tag{5.1}$$

Thus, the spatial gradient of the auto-ignition delay time is fuel-dependent for a given temperature gradient, as shown by the dashed lines in Figure 5.5. The lowest auto-ignition delay times are observed where the temperature is highest. Therefore, the left boundary of the hot spot auto-ignites first.

The findings of Dai et al. [35] have shown that for fuels with NTC behavior, cool spots may initiate auto-ignition in addition to hot spots. Figure 5.6 shows an exemplary configuration for such a cool spot. The temperature increases linearly from 760 K at the left boundary, to 820 K at the edge of the cool spot. At a pressure of 25 bar, the three surrogates show NTC behavior, where the auto-ignition delay times increase with increasing temperature. Thus, the reversed sign of $\partial\tau/\partial T_u$ leads to the same sign for the spatial gradient of auto-ignition delay times as for the hot spot, discussed previously. Consequently, the left boundary of the cool spot auto-ignites first, again.

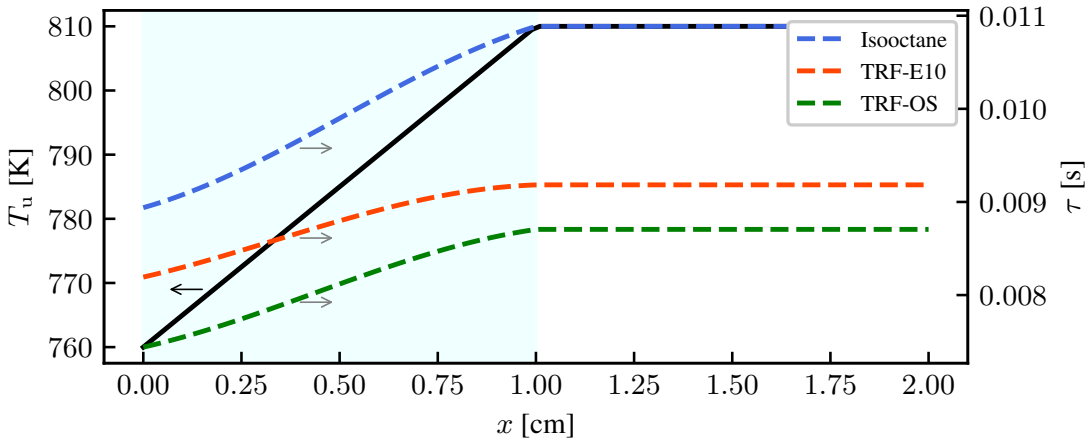

Figure 5.6.: Exemplary cool spot at p=25 bar defined by a linear temperature gradient within the interval highlighted in light blue. Corresponding auto-ignition delay times of the three surrogate fuels are shown as dashed lines. Temperatures are inside the NTC regime for all three surrogate fuels.

5.2.4. Critical temperature gradient analysis

The propagation velocity u_a of an auto-igniting mixture is crucial for the evolution of the propagation mode after auto-ignition. Neglecting mass diffusion and heat conduction, it is directly proportional to the spatial gradient of the auto-ignition delay time [19]:

$$u_a = \left(\frac{\partial \tau}{\partial x} \right)^{-1} . \tag{5.2}$$

A coupling between the auto-ignition front and the generated pressure wave can occur when the reaction front propagates approximately at the speed of sound a. With this and Equation (5.1), a critical temperature gradient can be defined as:

$$\left(\frac{dT_u}{dx} \right)_c = a^{-1} \left(\frac{d\tau}{dT_u} \right)^{-1} . \tag{5.3}$$

A positive sign of the critical temperature gradient indicates that a cool spot is required to initiate an auto-ignition front, while a negative sign signifies that a hot spot is needed. Based on 1-D simulations, Dai et al. [35] showed that the subsequent propagation front after a cool spot auto-ignition can evolve into the same modes as those known from hot spot auto-ignition, and concluded that cool spots may cause knocking combustion in engines operating within the NTC regime.

In engine operation with homogeneous mixtures, temperature gradients are the main influencing factor for the auto-ignition delay. It is assumed that temperature stratification is mainly influenced by the heat transfer in the cylinder. However, even with the same temperature stratifi-

cation, fuel differences in $\partial\tau/\partial T_\mathrm{u}$ lead to different critical temperature gradients. Hence, knock may develop at different thermodynamic conditions. To further investigate this hypothesis, the critical temperature gradient is calculated over the duration of the combustion process based on the thermodynamic conditions retrieved for the characterization of the operating points (see Figure 5.4).

Figure 5.7 shows the critical temperature gradient for all fuels and OP1500 at the respective latest spark timing (LST). MFB50 and MFB90 are marked as vertical lines.

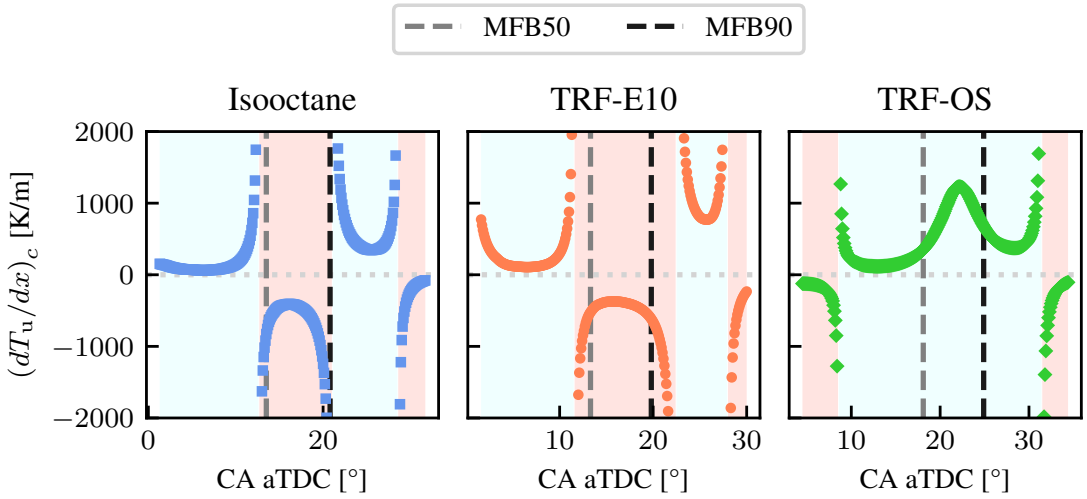

Figure 5.7.: Critical temperature gradient over crank angle for the three surrogate fuels at OP1500 and the latest spark timing each (see Table 5.1). Intervals with a positive value for the critical temperature gradient are highlighted in light blue, for a negative value in light red. MFB50 and MFB90 are marked with dashed lines for orientation.

For isooctane and TRF-E10, the development of the critical temperature gradient is similar. At the start of combustion, the gradient has a positive sign, indicating that a cool spot would initiate auto-ignition, which is highlighted by a light blue background. Just before MFB50, the thermodynamic conditions leave the NTC region (see Figure 5.4), leading to a singularity. Until shortly after MFB90, the critical temperature gradient is negative. A hot spot would initiate auto-ignition for these thermodynamic conditions, which is illustrated by a light red background. The critical temperature gradient of TRF-OS differs significantly. As shown in Figure 5.4, the thermodynamic conditions remain within the NTC regime during combustion. As a result, the critical temperature gradient is positive throughout the phase of interest. With this, the thermodynamic conditions may lead to auto-ignition initiated by a cool spot. This suggests, that although the fuels exhibit a comparable knock intensity, this may result from a different initiation process for TRF-OS.

Figure 5.8 shows the same analysis as before but for the three different spark timings of TRF-OS at OP1500. At advanced spark timing (see IST and EST), the combustion trajectory leaves the NTC regime. As for the other fuels, the critical temperature gradient between MFB50 and

MFB90 is negative. However, the respective interval is smaller than for the other surrogates. This indicates that auto-ignition at a cool spot may occur at a later stage of the combustion process.

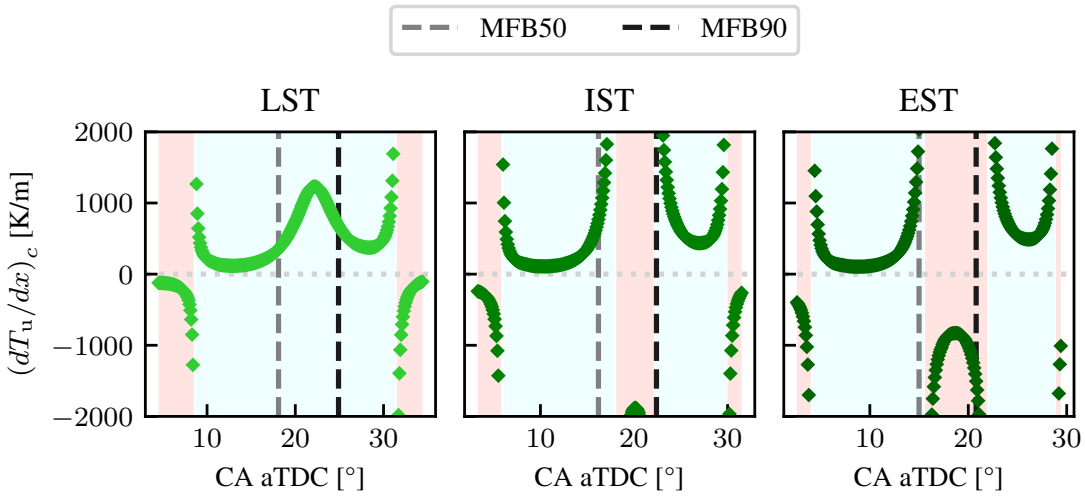

Figure 5.8.: Critical temperature gradient over crank angle for TRF-OS at OP1500 and all three spark timings. Intervals with a positive value for the critical temperature gradient are highlighted in light blue, for a negative value in light red. MFB50 and MFB90 are marked with dashed lines for orientation.

At the higher engine speed of OP2500, combustion of all three surrogates occurs mainly at thermodynamic conditions beyond the NTC regime (see Figure 5.4). As a result, the critical temperature gradient is mostly negative for all fuels, as exemplified in Figure 5.9 for the latest spark timing (LST). Again, isooctane and TRF-E10 show very similar behavior, while TRF-OS differs slightly, showing the first singularity closer towards MFB50.

In summary, the critical temperature gradient analysis shows that auto-ignition may be initiated by different mechanisms due to the NTC behavior of the surrogate fuels. For OP2500, hot spot auto-ignition appears to be predominant due to thermodynamic conditions outside the NTC. For OP1500, especially for TRF-OS, cool spot auto-ignition may occur. This suggests that auto-ignition may start in different areas of the cylinder, which could explain the different knock resistances observed. However, a detailed evaluation of the significance of auto-ignition initiated by cool spots or hot spots for the conditions studied can not be conducted as information on the local temperature distribution cannot be derived with sufficient accuracy from the available experimental data. Therefore, the influence of local inhomogeneities is investigated in Chapter 6 using engine LES.

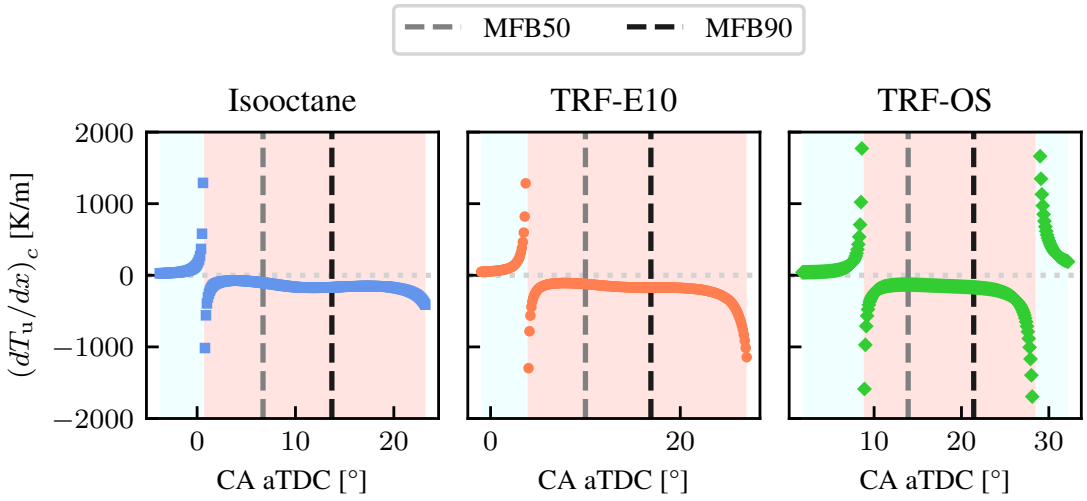

Figure 5.9.: Critical temperature gradient over crank angle for the three surrogate fuels at OP2500 and the latest spark timing each. Intervals with a positive value for the critical temperature gradient are highlighted in light blue, for a negative value in light red. MFB50 and MFB90 are marked with dashed lines for orientation.

5.2.5. Conclusions on model-based analysis

The experimental findings (see Section 5.1) suggested a potential influence of NTC behavior as a source of the differences in the knock limits. This aspect is investigated in a model-based analysis and the experimental findings are complemented as follows:

- Differences in the heat duration are correlated with the laminar burning velocity of the surrogate fuels.
- The observed trends in auto-ignition delay times do not reflect the order of knock resistance observed in the experiments.
- During combustion, the temperature and pressure of the unburned mixture are mostly within the NTC regime at the lower engine speed and are mostly above the NTC regime at the higher engine speed.
- Analysis of the critical temperature gradient indicates that the NTC behavior may lead to different mechanisms of auto-ignition initiation. At the lower engine speed, cool spot auto-ignition may occur. At the higher engine speed, auto-ignition is assumed to be initiated by hot spots. These different mechanisms could explain the different knock resistances observed.

The analysis shows a potential influence of NTC behavior on the global auto-ignition process. A more detailed investigation on this is conducted subsequently for the surrogate fuel TRF-OS.

5.3. Influence of NTC behavior on auto-ignition in engine operation

Based on the previous findings, an existing precursor auto-ignition model is extended to capture the non-linear auto-ignition process of surrogate fuels with NTC behavior (see Section 2.2.2). This model is applied and validated in 0-D configurations to investigate the auto-ignition process under homogeneous engine-relevant conditions. First, the operating conditions are discussed (see Section 5.3.1). For further characterization, the auto-ignition process of the surrogate fuel TRF-OS is analyzed under homogeneous conditions in 0-D simulations. These are performed under engine operating conditions first (see Section 5.3.2) and for the variable unburned temperature and pressure of the mean engine cycle thereafter (see Section 5.3.3).

5.3.1. Characterization of operating conditions

For the subsequent analysis, the late spark timing (LST) of OP1500 is investigated for the surrogate fuel TRF-OS (see Table. 5.1). In Figure 5.10 the evolution of the respective unburned temperature T_u, pressure p and the mass fraction burned (MFB) are shown. The start of combustion expressed as 1% of the mass fraction burned (MFB1), and the end of combustion (MFB99) are marked for orientation. After the onset of combustion at approximately 5° CA, the pressure and unburned temperature increase to about 840 K and 45 bar (around 20° CA) and then decrease until the end of combustion at about 33° CA and beyond.

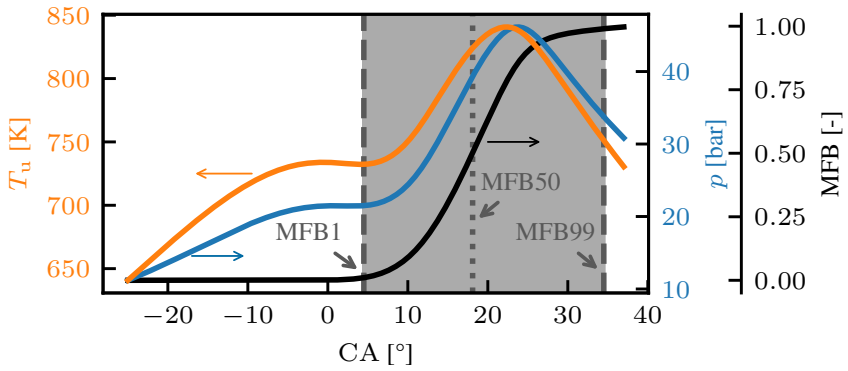

Figure 5.10.: Evolution of unburned temperature T_u, pressure p and the mass fraction burned (MFB) for the mean experimental cycle. MFB1, MFB50 and MFB99 are marked for orientation.

The trajectory of the auto-ignition delay times resulting from these thermodynamic conditions depicted in Figure 5.4 (see light green line) clearly shows that a major part is located within the NTC regime. In an n-heptane-based study, Law et. al indicated that a two-stage auto-ignition process can be observed for thermodynamic conditions in the NTC regime [31]. The existence of such behavior for the surrogate fuel TRF-OS used in this study is examined in the next section.

5.3.2. Auto-ignition process under engine operating conditions

The auto-ignition process under representative thermodynamic conditions is further analyzed with respect to the precursor modeling. Therefore, a homogeneous reactor simulation using a detailed mechanism [86] is initialized with stoichiometric conditions at unburned temperature and pressure corresponding to MFB50 of the mean cycle (see Figure 5.10). The obtained temperature evolution during the auto-ignition process is depicted in Figure 5.11. The upper plot shows the evolution of the auto-ignition progress variable $Y_{c_{I,u}}$, and the lower plot shows its source term $\dot{\omega}_{Y_{c_{I,u}}}$.

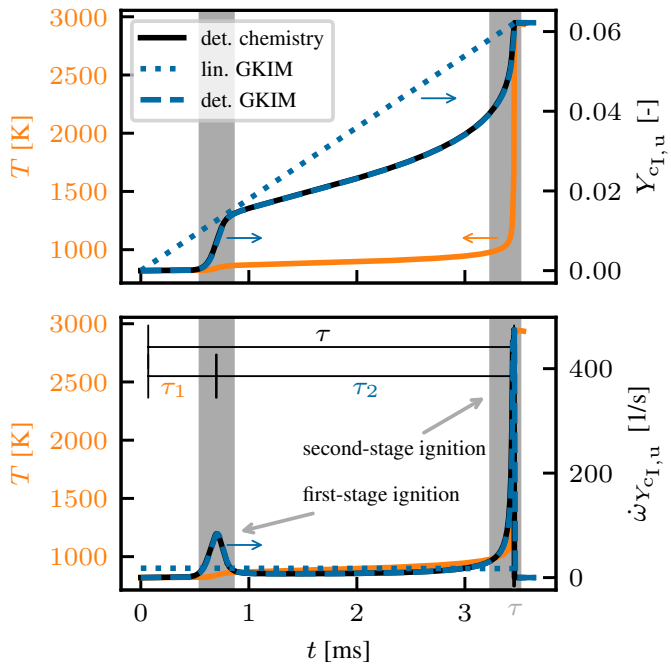

Figure 5.11.: Auto-ignition process for thermodynamic conditions of MFB50. Development of temperature, auto-ignition progress variable (top) and source term of auto-ignition progress variable (bottom). Results for a coupled simulation applying the auto-ignition modeling are shown in blue; the results of the *detailed gKIM* are shown as dashed lines, and those of the *linear gKIM* as dotted lines. The intervals defining total, first-stage and second-stage auto-ignition delay times (τ, τ_1 and τ_2, respectively) are illustrated in the bottom plot.

The temperature evolution exhibits the expected two-stage auto-ignition behavior. The first-stage ignition results in a temperature rise of approximately 45 K. During the second-stage ignition, the temperature increases significantly by 1600 K. The two-stage behavior is reflected in the evolution of the auto-ignition progress variable, which is shown as a solid black line. Both, the first-stage and the second-stage auto-ignition are characterized by the increased formation of $Y_{c_{I,u}}$ and a corresponding peak in the source term. This source term is used in the *detailed gKIM* (see Section 2.2.2). When applying the auto-ignition modeling in a coupled simulation to

a homogeneous reactor under the same thermodynamic conditions, the detailed gKIM is able to reproduce the evolution of the auto-ignition progress variable $Y_{c_{I,u}}$ with very high accuracy, as shown by the dashed blue line. The simplified source term assumption of the *linear gKIM* leads to a linear increase of the auto-ignition progress variable $Y_{c_{I,u}}$ until auto-ignition (see dotted blue line). While the auto-ignition delay time is correctly reproduced, the two-stage auto-ignition is obviously not captured by this model.

The analysis confirms, that for the representative thermodynamic conditions inside the NTC regime, a two-stage auto-ignition occurs under homogeneous conditions for the investigated surrogate fuel. This is consistent with the detailed analysis for n-heptane performed by Law et al [31]. They showed, in particular, that inside the NTC regime, the first-stage auto-ignition determines the total auto-ignition delay time by changing the initial conditions of the second-stage auto-ignition. Adopting the methodology used by Law et al [31], the auto-ignition delay times of the two stages are analyzed for the TRF-OS at the highest and lowest pressure investigated before, see Figure 5.12. The total and first-stage auto-ignition delay times are shown in black and orange, respectively. The second-stage auto-ignition delay time is defined by the difference between the total and the first-stage auto-ignition delay time (see Figure 5.11) and is shown in blue. Squares refer to 20 bar and circles to 60 bar pressure. In accordance with the findings of Law et al [31], the first-stage auto-ignition delay times decrease with increasing temperature, while the second-stage auto-ignition delay times increase. This results in increasing total auto-ignition delay times in the NTC regime. This behavior is also observed for higher pressures but with lower first-stage auto-ignition delay times and the NTC regime shifted to higher temperatures.

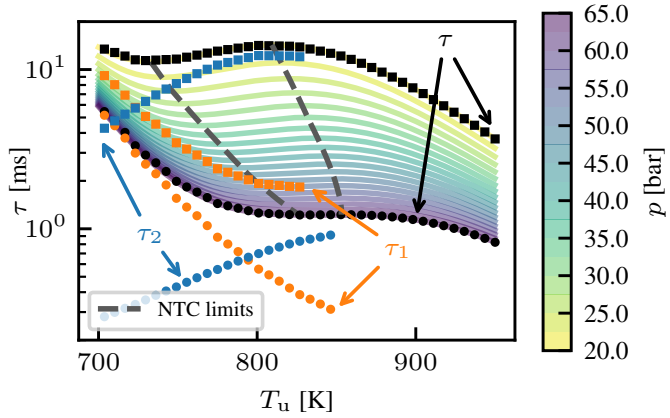

Figure 5.12.: Analysis of total (τ, black), first-stage (τ_1, orange) and second-stage (τ_2, blue) auto-ignition delay times for 20 bar (squares) and 60 bar (circles).

This analysis demonstrates that two-stage auto-ignition behavior determines the NTC behavior for the TRF-OS investigated. The relevance of two-stage auto-ignition for the variable thermodynamic conditions of the mean engine cycle is investigated in the next section.

5.3.3. Auto-ignition process during the mean engine cycle

The auto-ignition process is further investigated under variable engine-relevant thermodynamic conditions in an *a-priori* 0-D configuration. Based on the pressure and the unburned temperature of the mean experimental cycle (see Figure 5.10) and stoichiometric mixture, the source term for the precursor modeling is extracted from the auto-ignition manifold (see Section 2.2.2). With that, Equations (2.40) and (2.41) are solved to obtain the evolution of the auto-ignition progress variable $Y_{c_{I,u}}$, which is then normalized to $c_{I,u}$ (see Section 2.2.2). The methodology is illustrated in Figure 5.13.

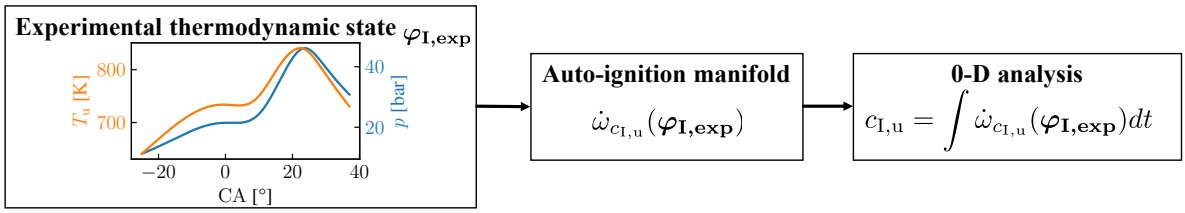

Figure 5.13.: Methodology of 0-D analysis: the thermodynamic state of the mean experimental cycle $\varphi_{I,exp}$ is used to access the auto-ignition manifold. The extracted source term is integrated over time to retrieve the normalized auto-ignition progress variable $c_{I,u}$.

The upper plot of Figure 5.14 shows the evolution of the normalized auto-ignition progress variable, and the lower plot the respective source term. Additionally, the imposed pressure is depicted for orientation.

The importance of non-linear auto-ignition chemistry for the variable thermodynamic conditions can be illustrated by comparing the two different approaches for the source term of the precursor models (see Section 2.2.2). Without the incorporation of the two-stage auto-ignition characteristics in the *linear gKIM* (see Figure 5.11), the final value of the progress variable is below unity and hence no auto-ignition is predicted. Given the knocking operating conditions, this is not reasonable. Therefore, the *linear gKIM* is not considered in the further analysis. The prediction of the *detailed gKIM*, incorporating complex auto-ignition chemistry, is shown as solid lines. A two-stage ignition behavior can be observed. Around TDC (0.0° CA), first-stage ignition is predicted. At this time, the normalized auto-ignition progress variable increases to around 0.5 since the source term shows a respective local maximum. At peak pressure, the source term has a second peak and $c_{I,u}$ reaches unity, predicting second-stage ignition.

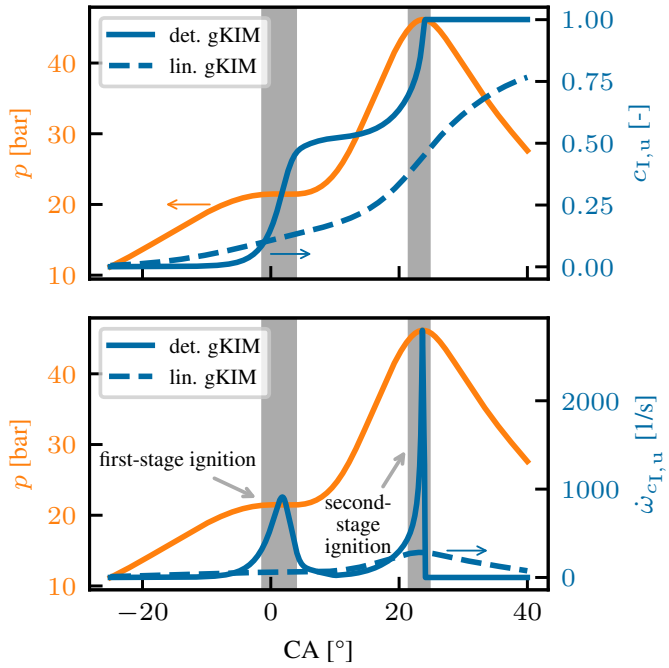

Figure 5.14.: 0-D analysis of auto-ignition modeling based on the thermodynamic conditions of the average experimental cycle. Imposed pressure, normalized auto-ignition progress variable (top) and source term of auto-ignition progress variable (bottom). The *detailed gKIM* is shown as solid lines, and the *linear gKIM* as dashed lines.

5.3.4. Conclusions on influence of NTC behavior on auto-ignition

The extended auto-ignition precursor model is applied in 0-D configurations for the investigations of the auto-ignition process of TRF-OS under homogeneous conditions based on the mean experimental cycle. The main findings are summarized as follows:

- A two-stage auto-ignition behavior is observed in a representative homogeneous reactor simulation as well as under the engine-relevant variable thermodynamic conditions
- A non-linear source term formulation is needed to capture the two-stage auto-ignition behavior.
- While the second-stage auto-ignition delay time increases with temperature in the NTC regime, the first-stage auto-ignition delay time decreases.

Although giving valuable insights, the performed analysis based on 0-D configurations cannot describe spatial stratification and the influence of turbulent flame propagation. This particular aspect is analyzed in the engine LES studies conducted in the following.

6. LES investigation of knocking combustion initiation

The previous analysis showed, that a two-stage auto-ignition process is likely to occur when engine combustion takes place under NTC-relevant conditions. However, the influence of NTC behavior on the local auto-ignition process in engine operation under knocking conditions has not been investigated yet. In particular, the question remains how temperature stratification and flame propagation affect the local auto-ignition process under thermodynamic conditions in the NTC regime. Furthermore, it is of interest how cycle-to-cycle variations influence the auto-ignition process under these knocking combustion conditions. To investigate these aspects, two multi-cycle LES studies are conducted employing the extended auto-ignition model. The first study discussed in Section 6.1 focuses on the NTC influence on the local auto-ignition process. The second study discussed in Section 6.2 analyzes the correlations of cycle-to-cycle variations of flow, combustion and auto-ignition.

6.1. Influence of NTC behavior on local auto-ignition[1]

In this section, a multi-cycle engine LES[2] is performed to investigate the influence of turbulent flame propagation and temperature stratification on the local auto-ignition process under the NTC related thermodynamic conditions investigated. This includes the demonstration of the applicability of the detailed gKIM model in the context of an engine LES under such operating conditions.

A description of the experimental setup is given in Chapter 3. The numerical setup and modeling are discussed in Chapter 4. The same operating conditions as in Section 5.3 are investigated. The operating point OP1500 of the surrogate fuel TRF-OS at late spark timing is further characterized in Section 5.3.1.

After validating the engine LES combustion methodology (see Section 6.1.1), the process of flame propagation and auto-ignition is investigated for a selected LES realization (see Section 6.1.2). Subsequently, the model predictions in terms of the onset of auto-ignition and the mass affected by it (critical mass) are compared to experimentally recorded pressure traces including cycle-to-cycle variations (see Section 6.1.3). Further investigations on cycle-to-cycle

[1] This section is partly taken from the publication by Kircher et al. [P2] which was created during the work on this thesis. In [P2], I was the main author of the parts used.

[2] More details on the approach used in this study are given in Section 4.1.2.

variations are conducted to analyze the spatial distribution and temporal evolution of the critical mass (see Section 6.1.4) and the influence of combustion progress on the unburned mass at knock onset 6.1.5.

6.1.1. Combustion process

At first, experimental and LES pressure traces are depicted in Figure 6.1. The pressure traces of the 1000 single cycles recorded in the experiment are shown in gray. After spark ignition, the pressure traces show large cycle-to-cycle variations. Faster combustion cycles lead to higher peak pressures, with differences in the peak pressure of around 20 bar compared to the slowest cycles. The 17 LES realizations are shown in blue. The variation in the timing of the start of combustion results in different mass burning rates. With that, both the fast and the slow cycles can be properly reproduced, and almost the entire experimental envelope is captured by the LES.

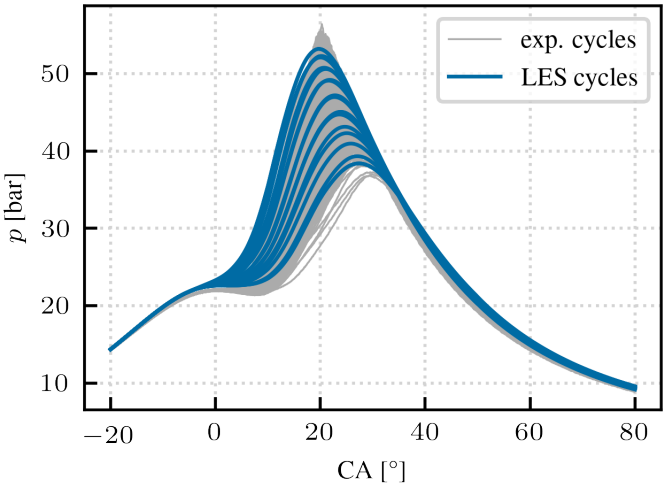

Figure 6.1.: Pressure traces of experiments and LES realizations.

6.1.2. Local auto-ignition process and flame propagation

The local auto-ignition process and the influence of flame propagation are investigated in the following. In particular, the fastest burning LES cycle is considered due to its relevance for auto-ignition, since experimental cycles with a comparable pressure trace show knock.

The analysis depicted in Figure 6.2 is based on a horizontal slice through the cylinder with a vertical position of 2.5 mm above the TDC of the piston, cutting the lower electrode of the spark plug. A perspective from above is chosen, with the engine geometry shown transparently for orientation. The times −9.0° CA, 0.0° CA, 9.0° CA and 18° CA (from top to bottom)are considered, covering the relevant time span of the flame propagation and the auto-ignition

process. The left column shows the unburned temperature distribution and the right column depicts the results of the precursor model. The flame front defined by $\widetilde{c} = 0.5$ is shown as a white iso-line to illustrate the influence of flame propagation on auto-ignition in the unburned gas. The mean cylinder pressure $\langle \overline{p} \rangle_{\mathrm{cyl}}$ is given for reference.

Already prior to spark ignition ($-9.0°$ CA), the $\widetilde{c}_{\mathrm{I}}$-field shows the onset of auto-ignition. The influence of unburned temperature on the first-stage auto-ignition delay time in the NTC regime, observed under homogeneous conditions in Section 5.3, is also visible for the auto-ignition process in the engine under temperature stratification. In particular, the first-stage auto-ignition progress is highest ($\widetilde{c}_{\mathrm{I}} \approx 0.15$) in the regions of the highest unburned temperatures ($\widetilde{T}_{\mathrm{u}} \approx 780$ K), due to the lowest first-stage auto-ignition delay times (see Figure 5.12).

At TDC, shortly after spark ignition (0.0° CA), a widespread first-stage auto-ignition is observed. The increased mean unburned temperature and pressure are associated with lower first-stage auto-ignition delay times (see Figure 5.12). Thus, regions where auto-ignition had not yet progressed, undergo a more pronounced first-stage auto-ignition. For regions that have already undergone first-stage auto-ignition, the further progress is related to the second-stage auto-ignition delay time. Since these increase towards the upper NTC limit at approximately 850 K, the auto-ignition process is decelerated in regions with higher unburned temperatures. Thus, as a result of the NTC behavior, the highest values of $\widetilde{c}_{\mathrm{I}}$ are observed in regions of intermediate temperatures of approximately 750 K.

With further combustion progress at 9.0° CA, the previously not-ignited areas of the unburned mixture now reached unburned temperatures high enough ($\widetilde{T}_{\mathrm{u}} \approx 750$ K) to undergo first-stage auto-ignition. Again it is more pronounced due to the increased pressure, while at higher unburned temperatures the auto-ignition process is prolonged. Now almost the entire unburned mixture is in an auto-igniting state. However, the propagating flame reduces the unburned mass and terminates the auto-ignition process in the burned mixture ($\widetilde{c}_{\mathrm{I}}$=0).

At a time close to peak pressure (18.0° CA), the majority of the mixture is consumed by the flame, leaving only pockets of unburned gas. Within those, the value of $\widetilde{c}_{\mathrm{I}}$ is almost uniform, due to the previously widespread first-stage auto-ignition. In particular, the further pressure increase lowered the second-stage auto-ignition delay times and hence a relevant part of the remaining unburned mass is predicted to undergo second-stage auto-ignition. This is indicated by values of $\widetilde{c}_{\mathrm{I}} > \varepsilon$ and contributes to the critical mass (see Section 2.2.2), which can be related to knock intensity as discussed in the next section.

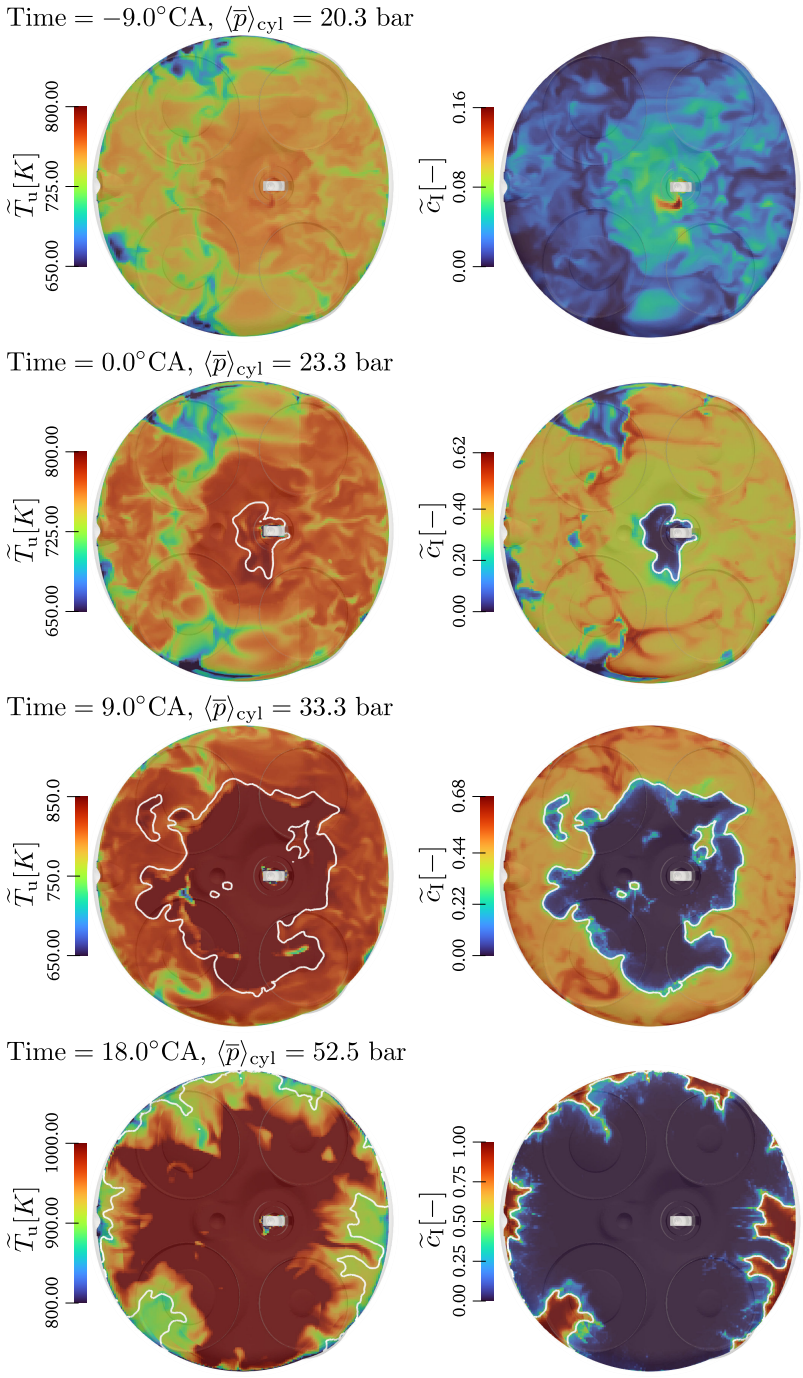

Figure 6.2.: Time series of local auto-ignition process and flame propagation. Horizontal slice at 2.5 mm above the TDC position of the piston; view from above, with engine geometry shown transparently. Analysis of local auto-ignition process for four different instants in time: prior to spark ignition, shortly after spark ignition, early combustion phase and close to peak pressure. The earliest time is at the top, the latest at the bottom. The plots show unburned temperature, $\widetilde{T}_{\mathrm{u}}$, on the left side and auto-ignition progress, $\widetilde{c}_{\mathrm{I}}$, on the right. The flame front is visualized based on $\widetilde{c} = 0.5$ as a white iso-line. The mean cylinder pressure, $\langle \overline{p} \rangle_{\mathrm{cyl}}$, is given for reference.

6.1.3. Global knock characteristics

For operation at the knock limit, the knock intensity is directly proportional to the mass consumed during auto-ignition [25]. For the precursor modeling utilized in this work, this mass is given by the critical mass, and the peak of its temporal evolution indicates the crank angle of knock onset, as shown in a previous work [A1].

The experimental unfiltered pressure signal p and the respective knock amplitude p' are depicted on the left-hand side of Figure 6.3 for representative fast, medium and slow cycles, with three individual cycles each. For faster cycles, the peak pressure appears closer to TDC (0.0° CA) and the knock amplitudes increase. The highest amplitudes, associated with the mean knock onset, appear in the vicinity of the crank angle of peak pressure. The overall knock intensity is low.

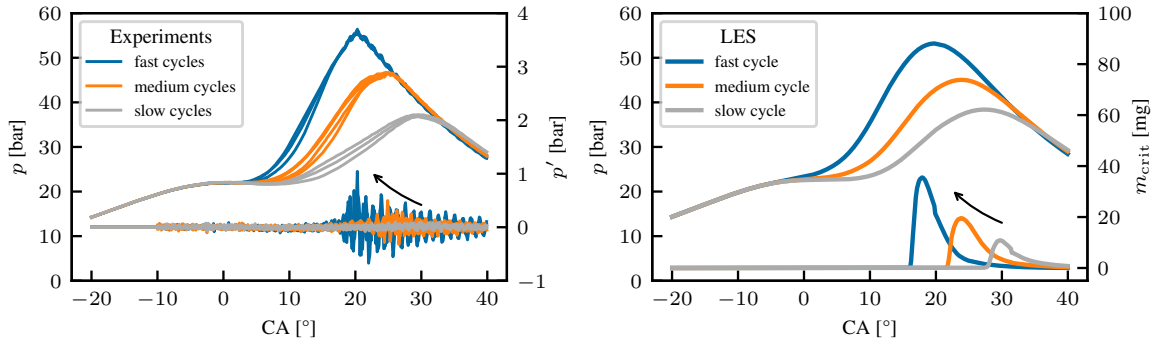

Figure 6.3.: Experimental unfiltered pressure signal and knock amplitude for three levels of peak pressure with three cycles each (left). Pressure traces and development of critical mass for three LES realizations (right).

The pressure traces of three corresponding LES cycles are shown on the right-hand side of Figure 6.3. Additionally, the development of the critical mass over the engine cycle is shown. For all three cycles, the peak of the critical mass is close to the crank angle of peak pressure. Furthermore, it is located closer to TDC for the fast cycle. With that, location and sensitivity are in good agreement with the experimental knock onset. The maximum critical mass increases with faster combustion, meaning a higher amount of unburned mixture is predicted to undergo auto-ignition. The trend of increasing critical mass agrees well with the increasing knock amplitudes in the experiment.

Thus, the amount of critical mass and the time at which its maximum is observed serve as indicators of the knock amplitude and its onset for the fuel under investigation with operating conditions in the NTC regime. Furthermore, the amount of critical mass and its temporal evolution are shown to be affected by differences in the mass burning rates. Both aspects are further considered in the next section, based on the local distribution of the critical mass.

6.1.4. Local distribution of critical mass

The further investigation of the local evolution of the critical mass and the influence of the propagating flame is based on a time series, where the crank angle of the maximum critical mass, defining the knock onset, is considered as the reference time. For that, the set of critical cells, Ω_{crit} (see Section 2.2.2), is extracted for the three representative LES realizations shown in the last section (see Figure 6.3). In Figure 6.4, the critical cells are highlighted in red color in an isometric view of the cylinder for the fast (left), medium (middle) and slow cycle (right). The flame front ($\widetilde{c} = 0.5$) is visualized as a gray iso-contour. The reference time is shown in the third row, while the first, second and last rows correspond to 2.0° CA and 1.0° CA before and 1.0° CA after this reference time, respectively.

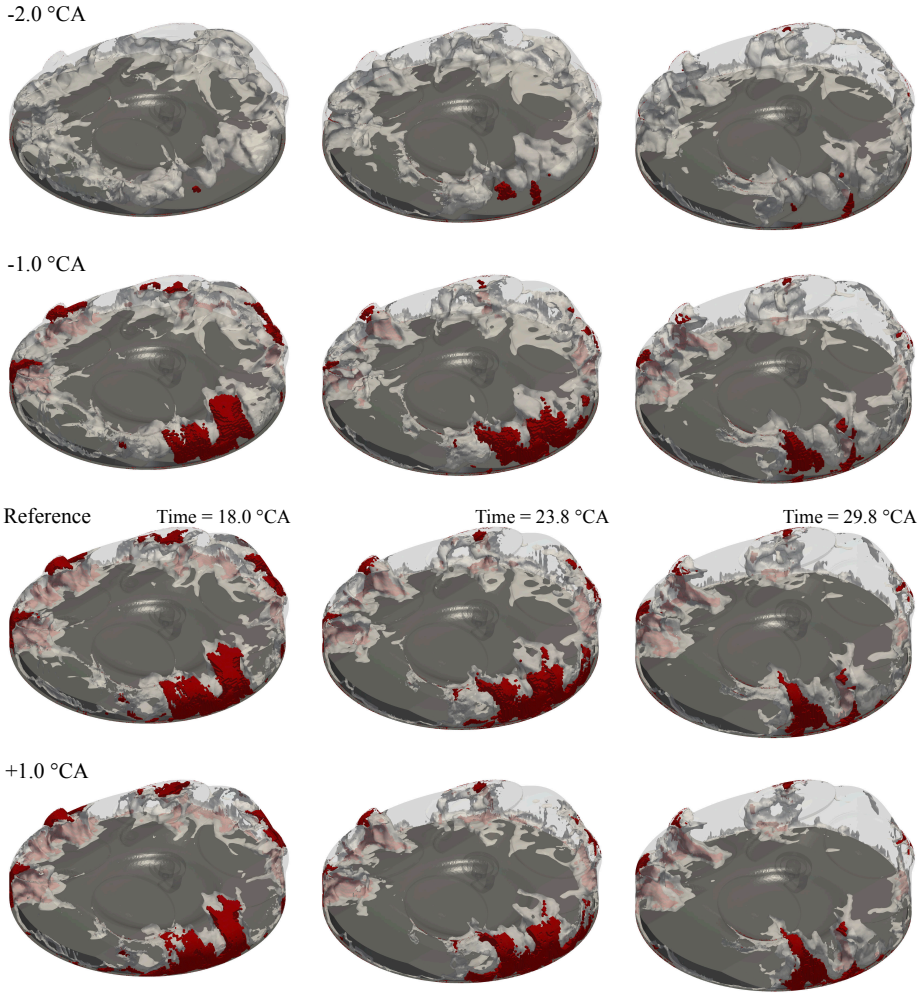

Figure 6.4.: Isometric view of fast (left), medium (middle) and slow cycle (right). The spatial distribution of critical cells is shown in red color. Flame front ($\widetilde{c} = 0.5$) visualized in gray. Time series for 4 crank angles each. Reference time of the peak of critical mass in the third row, 2.0° CA and 1.0° CA before and 1.0° CA after reference time in the first, second and last row, respectively.

The temporal development of critical cells is comparable for all three LES realizations, based on the common reference time. At 2.0° CA before knock onset (top row), the first critical cells appear in the unburned mixture ahead of the flame front. Within the time of 1.0° CA (second row), a relevant part of the volume enclosed by the cylinder walls and the wrinkled flame front reaches a critical state ($\widetilde{c}_{\mathrm{I}} > \varepsilon$) due to the NTC related widespread second-stage auto-ignition (see Section 6.1.2). Thus, the turbulent flame propagation, which defines the regions of the unburned mixture, is an important factor in determining the auto-ignition locations. At the time of knock onset (third row), the distance between the flame front and auto-ignition spots is small. Therefore, the propagating flame starts to consume the auto-ignited mass within the next 1° CA (see bottom row) and the critical mass reduces (see Figure 6.3). With the short time available for a potential reaction front to develop from the auto-ignition locations before being consumed by the flame front, detonation waves are unlikely to occur. This explains the direct relation between knock intensity observed in the experiments and the amount of critical mass, as shown in the previous section.

6.1.5. Unburned mass at knock onset

Besides these similarities in the temporal evolution of the critical mass, different mass burning rates result in different flame front propagation as suggested in Figure 6.4. At the reference time of knock onset (third row), the largest distance of the flame front to the walls is observed for the fast cycle, which indicates less combustion progress at knock onset. To further investigate this observation, the global combustion and auto-ignition process is shown in Figure 6.5. The upper plot depicts the MFB for the three LES cycles discussed in the last section in solid lines, and the respective MFB at knock onset (MFBKO) is indicated by a dot. In addition, the mean value of the auto-ignition progress variable in the unburned mixture is depicted as a dashed line. The lower plot shows the pressure trace (solid) and the mean unburned temperature of the unburned mixture (dashed).

Prior to spark ignition, the (first-stage) auto-ignition process is solely controlled by the increasing pressure and unburned temperature resulting from the compression caused by the piston movement. This leads to similar mean auto-ignition progress for all three cycles in this time span. However, the variation in the onset of combustion results in differences in the subsequent auto-ignition progress. With decreasing crank angle of combustion onset, higher mass burn rates are observed, leading to stronger compression heating. As a result, pressure and temperature increase earlier and more rapidly. This in turn increases the reactivity in the unburned mixture, leading to earlier second-stage auto-ignition and thus knock onset. Thus, despite the higher mass burn rate, the earlier knock onset results in a higher fraction of the unburned mixture at knock onset. With that, the MFBKO is lowest for the fast cycle (74.7%), resulting in the highest unburned mass at knock onset $m_{\mathrm{u,KO}}$ (see Figure 6.5 and Table 6.1). Since a relevant part of the unburned mass auto-ignites, the critical mass at knock onset $m_{\mathrm{crit,KO}}$ correlates with $m_{\mathrm{u,KO}}$. With that, the highest peak of critical mass of the fast cycle (see Figure 6.3) can be related to the lowest MFBKO.

Hence, the NTC behavior affects the local auto-ignition process in the unburned mixture, in particular leading to a widespread two-stage auto-ignition process. Here, the second-stage

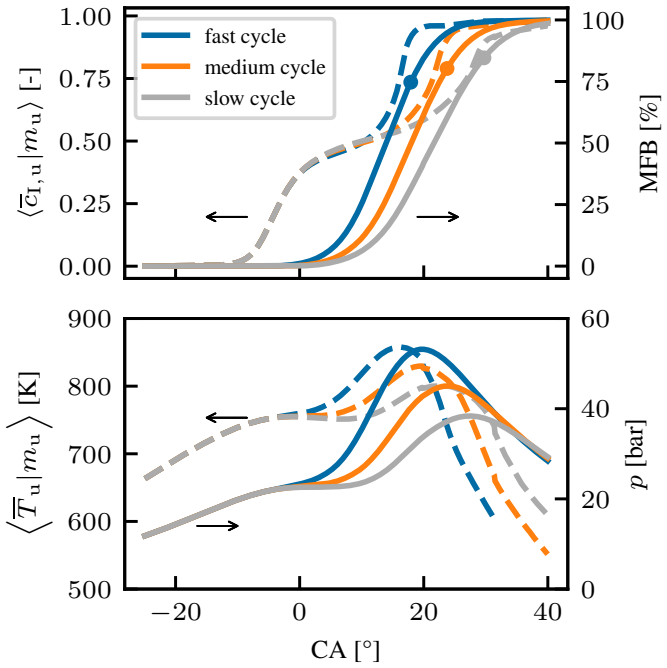

Figure 6.5.: Evolution of combustion (solid lines) and auto-ignition progress (dashed lines) (top), as well as pressure (solid lines) and unburned temperature conditioned on the unburned mixture (dashed lines) (bottom) for three LES realizations. The dots in the upper plot indicate CA and MFB at knock onset.

Table 6.1.: Summary of combustion progress (MFBKO), unburned mass ($m_{\mathrm{u,KO}}$) and critical mass ($m_{\mathrm{crit,KO}}$) at knock onset.

Cycle	MFBKO [%]	$m_{\mathrm{u,KO}}$ [mg]	$m_{\mathrm{crit,KO}}$ [mg]
Fast	74.7	97.8	35.5
Medium	80.3	76.3	22.5
Slow	84.6	59.6	10.9

auto-ignition is mainly influenced by differences in the mass burn rate. Thus, for the operating conditions at the knock limit investigated, the flame propagation determines the location and amount of the auto-igniting mass, and thus the knock intensity.

6.1.6. Conclusions on influence of NTC behavior on local auto-ignition

The influence of turbulent flame propagation and temperature stratification on the local auto-ignition process under NTC-related thermodynamic conditions is investigated in an engine LES study. The two-stage auto-ignition of the surrogate fuel TRF-OS is captured with the *detailed gKIM* model. The main findings are summarized as follows:

- The NTC behavior affects the local auto-ignition process, leading to a widespread first-stage auto-ignition.
- A relevant part of the unburned mass undergoes second-stage auto-ignition.
- For the fastest cycle, the highest amount of mass is consumed by auto-ignition and the earliest knock onset is predicted.
- The knock intensity observed in the experiments is directly related to the mass consumed by auto-ignition.
- Detonation waves are unlikely to occur due to the fast consumption of the auto-ignited mass by the flame front.
- Higher mass burn rates lead to higher reactivity of the unburned mixture and thus to earlier knock onset.
- The auto-ignited mass correlates with the combustion progress at knock onset.

The results clearly show that the NTC behavior affects the local auto-ignition process in the unburned mixture. However, mainly the flame propagation determines the knock intensity for the operating conditions at the knock limit.

With regard to cycle-to-cycle variations, the aspect of different mass burning rates is investigated. However, the engine LES approach employed prohibits the analyses of flow influences on the local auto-ignition process. Therefore, this particular aspect is investigated in the multi-cycle LES study described in the following.

6.2. Influence of cycle-to-cyle variations on knocking combustion initiation

In this section, a multi-cycle engine LES is performed to investigate the influence of cycle-to-cycle variations in flow and combustion on the knocking combustion initiation. As before, the auto-ignition process is modeled with the *detailed gKIM* model. Here, a multi-cycle strategy is employed in which different initial flow conditions are taken into account[3]. With that, correlations between flow, combustion and auto-ignition are investigated. Thereby, deeper insights into the knocking combustion initiation at the knock limit are retrieved from a joint analysis as described in the following.

The study is based on the second measurement campaign conducted by the research partner (see Section 3.1). Here, a fiber-optical spark plug has been inserted to provide additional local information. The same reference operating points and fuels as previously are investigated (see Table 3.2). In the simulations, OP1500 is considered for TRF-OS and isooctane with a comparable $\mathrm{KPP_{mean}}$. The main findings are comparable, so in the following analysis, as before, only TRF-OS is considered, unless otherwise stated. The respective operating point of TRF-OS is characterized by an experimental spark timings of -6° CA resulting in an MFB50 of 14.0 °CA, a $\mathrm{KPP_{mean}}$ of 1.04 bar and a σ_{KPP} of 0.51 bar[4].

6.2.1. Cycle-to-cycle variations of combustion and auto-ignition

The cycle-to-cycle variations within the combustion process lead to differences in associated quantities such as pressure and knock characteristics. These are discussed in the following.

Variations in pressure

The differences in heat release associated with different mass burning rates result in different pressure traces p_{exp} as shown in Figure 6.6. For the operating condition investigated, the mean pressure trace $\overline{p}_{\mathrm{exp}}$ of all cycles peaks at 53.9 bar. Considering the extreme values of all 1000 cycles the peak pressures range from 43.3 to 65.2 bar. The n cycles with the highest and lowest peak pressures are averaged as estimators for the 1-, 2- and 3-σ intervals around the mean, where n is 3, 46 and 318 respectively. Within the 1-σ interval, the peak pressures range between 51.0 and 58.7 bar.

The peak pressures of the 18 LES cycles conducted range from 46.8 to 58.9 bar. The mean LES cycle pressure $\overline{p}_{\mathrm{LES}}$ reaches 52.8 bar. Thus, the multi-cycle LES study covers a substantial portion of the cycle-to-cycle variations observed in the experiments and is in good agreement with the mean experimental pressure trace. The difference in the mean peak pressures is attributed to the combustion initiation routine used in the simulation. Here, the numerical spark timing does

[3] More details on the approach used in this study are given in Section 4.1.2. Adjustments to the combustion simulation framework previously used are discussed in Section A.2

[4] For isooctane the experimental spark timing is -7° CA, MFB50 is 13.2 °CA, $\mathrm{KPP_{mean}}$ is 0.93 bar and σ_{KPP} is 0.62 bar. Respective pressure traces of experiments and LES are shown in Section A.2.2

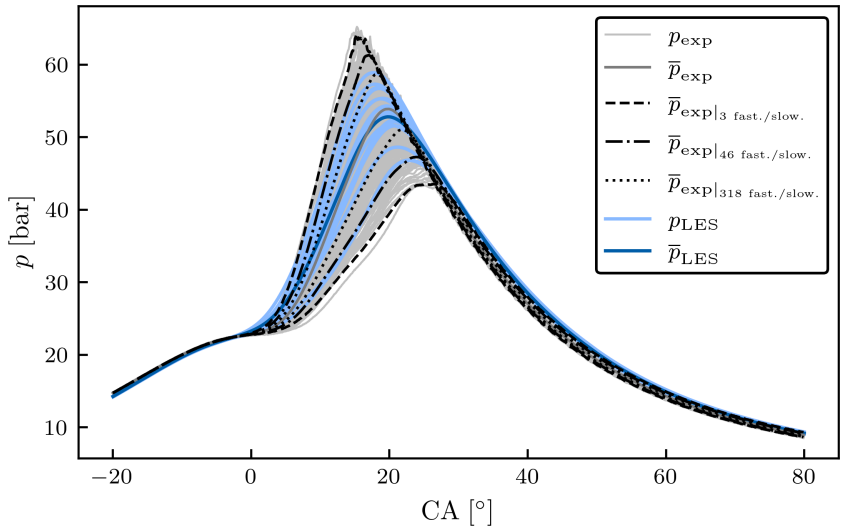

Figure 6.6.: Pressure traces of experiments p_{exp} (light gray) and LES realizations p_{LES} (light blue). In addition, the mean pressure traces $\overline{p}_{\mathrm{exp}}$ and $\overline{p}_{\mathrm{LES}}$ are shown (gray and blue, respectively). The black lines indicate estimators for the experimental 1-, 2- and 3-σ intervals (dotted, dash-dotted and dashed, respectively).

not necessarily correspond to the experimental value and is therefore not known in advance. The difference of about 1.0 bar is considered insignificant given the number of cycles conducted.

Further comparison is based on the relative frequency and the cumulative relative frequency of the respective peak pressures p_{max} as shown in Figure 6.7. The same conclusions as before can be drawn. The LES histogram shows a reasonable variation of p_{max}, which is comparable to the bulk of the experimental histogram data. The shift in the mean p_{max} is apparent here as well. In the experiments, the frequency increases continuously up to 56.75 bar before decreasing again. In contrast, the histogram of the LES shows a local maximum for the lowest bin, which is attributed to the comparably low number of samples available from the LES. The cumulative relative frequency has the same shift. However, the agreement in the slope between the simulation and the experiment indicates, that the available number of LES cycles captures the variance in combustion with reasonable agreement and thus can be used for further comparison with the experiment.

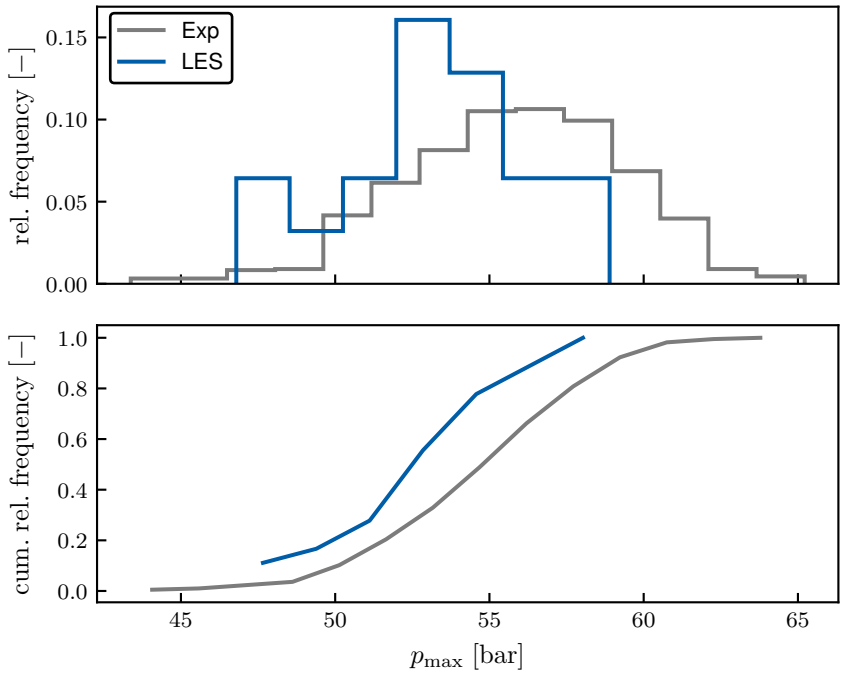

Figure 6.7.: Histograms of peak pressures $p_{\max}$ of experiments (gray) and LES realizations (blue). The top shows a relative frequency, and the bottom a cumulative relative frequency histogram.

Variations in knocking combustion

The variations in combustion consequently lead to a variation in the knocking behavior of the 1000 individual experimental cycles. Based on the signal of the in-cylinder pressure transducer, the knock amplitude KPP (see Section 3.2.1) is determined. In addition, the filtered pressure signal is used to determine the crank angle of knock onset $\mathrm{CA}_{\mathrm{KO}}$. It is defined here as the crank angle at which the value of the high-frequency pressure oscillations exceeds a threshold of 0.25 bar for the first time considering only cycles with a KPP > 0.4 bar. As shown in Figure 6.8, the variation in knock onset spans an interval from about 13.8 to 25.2° CA, with the 2-σ-interval ranging from 14.6° to 22.5° CA. Relating this to the crank angle of the peak pressure $\mathrm{CA}_{p_{\max}}$, it is observed that most cycles have a knock onset before the peak pressure is reached (cf. dash-dotted black line). Applying a linear least-square fit shows that the mean knock onset is closer to the peak pressure for later knock onsets.

For the simulations, the knock onset $\mathrm{CA}_{m_{\mathrm{crit,max}}}$ is determined based on the critical mass [P2]. The variation in knock onset ranges from 15.6° to 23.3°CA. The 2-σ-interval of the experiments is well captured, with 89% of the LES cycles showing knock onset between 14.2° and 22.6°CA. In addition, the LES captures the knock onset relative to the peak pressure with very good agreement. The slope of the linear fit is in agreement with the experiment and all LES samples are within the experimental 95% confidence band.

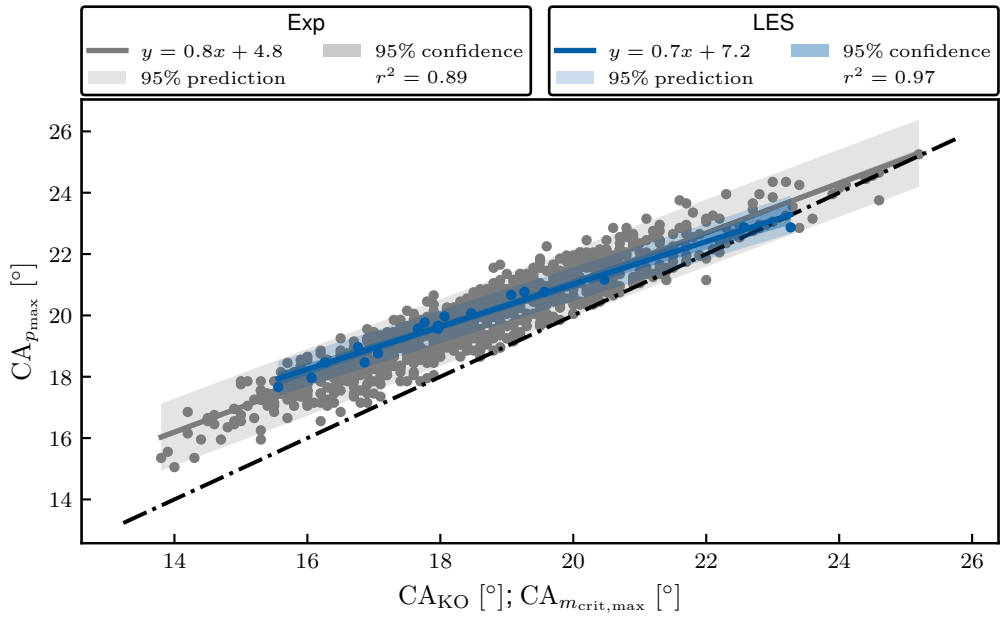

Figure 6.8.: Crank angle of peak pressure $\mathrm{CA}_{p_{\max}}$ as function of crank angle of knock onset of experiment $\mathrm{CA}_{\mathrm{KO}}$ (gray) and simulation $\mathrm{CA}_{m_{\mathrm{crit,max}}}$ (blue), respectively. A linear least-square fit of the data is shown as a solid line. The corresponding prediction and confidence bands are shown with transparency of the respective colors. The black dash-dotted line depicts the identity for orientation.

Besides the variations in knock onset, the knock intensity KPP varies from cycle to cycle as shown in Figure 6.9. Each cycle has an individual value pair for KPP and $\mathrm{CA}_{\mathrm{KO}}$. While cycles with a KPP below the $\mathrm{KPP}_{\mathrm{mean}}$ of 1.04 bar show a wide range in $\mathrm{CA}_{\mathrm{KO}}$, higher values of KPP only appear for earlier $\mathrm{CA}_{\mathrm{KO}}$.

In agreement with Robert et al. [25], the study discussed in the previous section has shown, that mainly the mass consumed by the auto-ignition determines the knock intensity at the knock limit. For the auto-ignition model, this mass is reflected by the maximal critical mass $m_{\mathrm{crit,max}}$ [P2, A1]. Due to the comparatively limited data set, it is not possible to conclusively assess whether the simulations can capture the trend toward higher knocking intensity with an earlier knock onset. However, for the available samples, the lowest observed $\mathrm{m}_{\mathrm{crit,max}}$ increases with earlier $\mathrm{CA}_{m_{\mathrm{crit,max}}}$. Here, the LES realizations capture variations in the knock intensity; different values of $m_{\mathrm{crit,max}}$ are observed for similar $\mathrm{CA}_{m_{\mathrm{crit,max}}}$. This indicates, that local differences lead to variations in the global knock behavior, which is a particular focus of the subsequent analysis.

The variations of knocking combustion discussed above show the global response to the local process of auto-ignition in the unburned gas. No local information is available in the usual solely pressure-based measurement campaigns (e.g., the study described in Section 6.1). The use of a fiber-optical spark plug in this measurement campaign enables the determination of the most likely knock initiation direction for each cycle (see Section 3.2.2). The respective circumferential

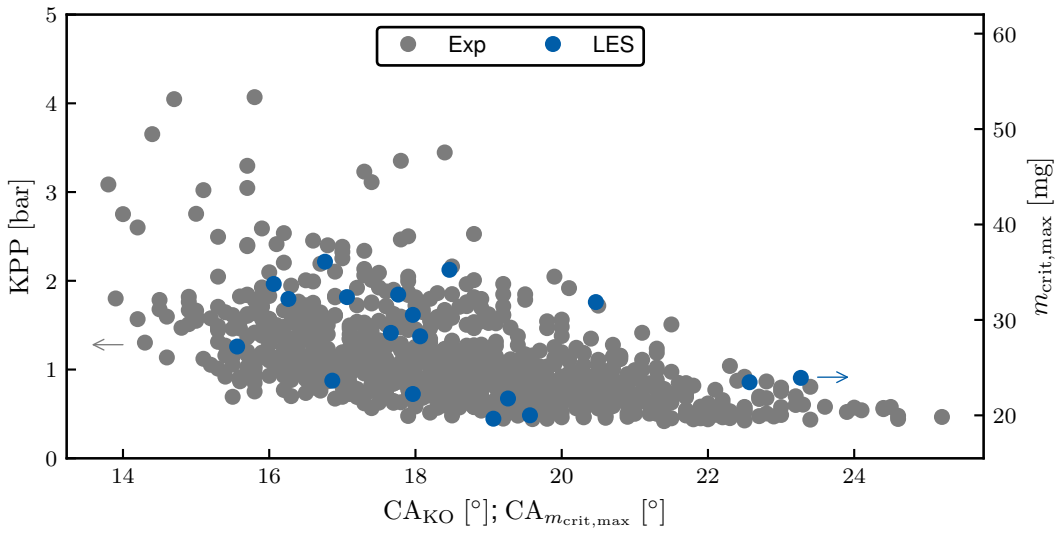

Figure 6.9.: Knock intensity KPP (experiments (Exp), shown in gray) and maximal critical mass $m_{\mathrm{crit,max}}$ (LES, shown in blue) as a function of knock onset $\mathrm{CA_{KO}}$ and $\mathrm{CA}_{m_{\mathrm{crit,max}}}$, respectively.

distribution is shown in Figure 6.10. For orientation purposes, the inlet valves (IV) and exhaust valves (EV) are shown in the illustration centered around the spark plug. The view is along the axis of the spark plug. Each bin reflects the acceptance cone of the corresponding optical channel (see Figure 3.1). The height of each bar corresponds to the number of experimental cycles N_{exp} for which the respective knocking combustion initiation direction has been determined.

The knock initiation is not evenly distributed around the circumference of the engine. Most cycles show knock initiation between the exhaust valves (EV1 and EV2) and slightly fewer cycles between the intake valves (IV1 and IV2). In contrast, there are regions of less knock initiation between the exhaust valve and the intake valve on either side.

For the LES, the data is transformed into cylindrical coordinates aligned with the experimental configuration of the fiber-optical spark plug. Instead of acceptance cones, wedges are used for circumferential binning. As a first estimate, the most likely knock initiation direction is determined using the bin with the highest $m_{\mathrm{crit,max}}$ at the time of knock onset $\mathrm{CA}_{m_{\mathrm{crit,max}}}$. The respective histogram is shown in Figure 6.10. The majority of the LES realizations show the highest $m_{\mathrm{crit,max}}$ towards the region between the exhaust valves. Knock initiation towards the intake valves is predicted for only one cycle. In general, this reflects the trend of the experimental observations. However, it is difficult to draw a general conclusion with statistical significance as to whether this approach is suitable for estimating the most probable knock initiation direction.

Thus, the entire auto-igniting mass at the time of knock onset is considered in the following analysis. The respective circumferential distribution of the critical mass of each LES realization is shown in Figure 6.11. The bars are plotted with an alpha value of 0.1, so the overlap of 10 bars results in total opacity. The mean value of all distributions is plotted as a dashed line.

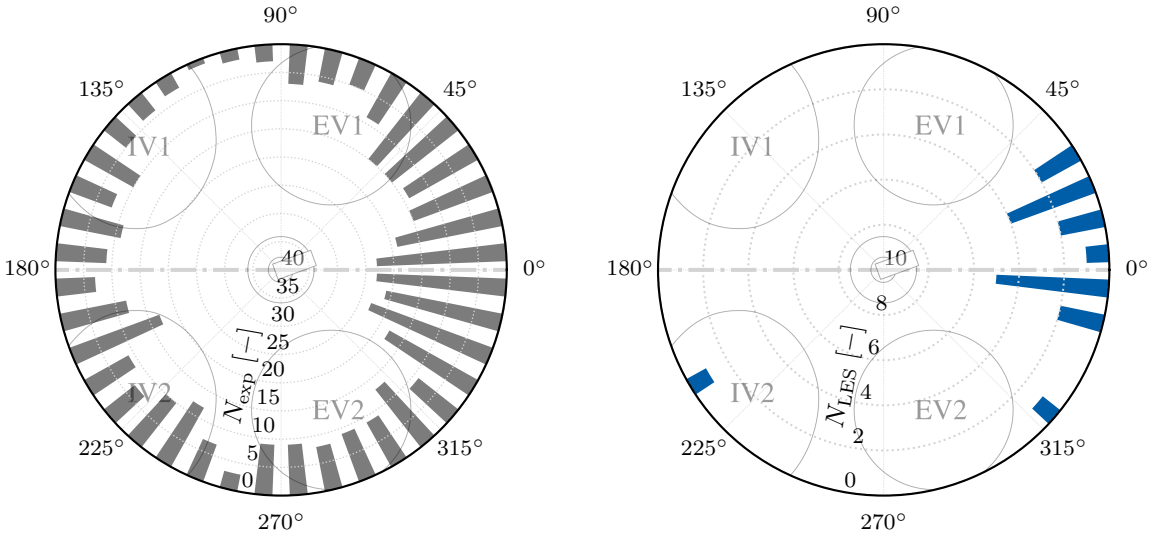

Figure 6.10.: Circumferential distribution of knock initiation direction. Experiments are shown on the left, LES on the right side. For orientation, intake valves (IV) and exhaust valves (EV) are shown in the illustration centered around the spark plug. The view is along the axis of the spark plug.

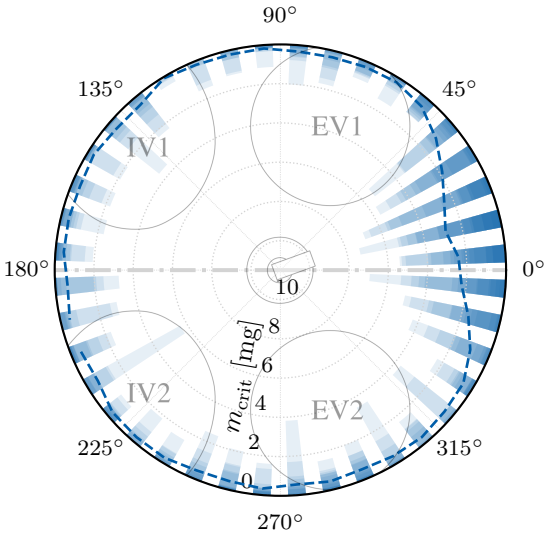

Figure 6.11.: Circumferential distribution of critical mass at the time of knock onset of each LES realization. Individual bars have a transparency alpha value of 0.1. The dashed line indicates the mean distribution.

The mean distribution shows the highest auto-igniting mass between the exhaust valves which is in agreement with the analysis of the knock initiation direction. However, the individual bars indicate, that there is also considerable auto-igniting mass in other regions. For the region between the intake valves, there are more cycles with higher auto-igniting mass than for the regions between the intake and the exhaust valves on either side. This agrees with the experimentally observed knock initiation directions.

A similar trend is observed for the respective comparison of experimental knock initiation direction and distribution of auto-igniting mass for isooctane as shown in Figure 6.12. Compared to TRF-OS, more frequent knock initiation between the intake valves and less frequent knock initiation between the valves on either side is observed in the experiments. Corresponding observations are made based on the circumferential distribution of the auto-ignition mass. There are higher peaks of auto-igniting mass between the intake valves and less auto-igniting mass between the valves on either side. This indicates that the circumferential distribution of the auto-igniting mass may be a good indicator of the experimentally determined frequencies of knock initiation direction even with a low number of LES realizations. Alternatively, a different definition of the numerical knock initiation direction discussed above could be the subject of further studies.

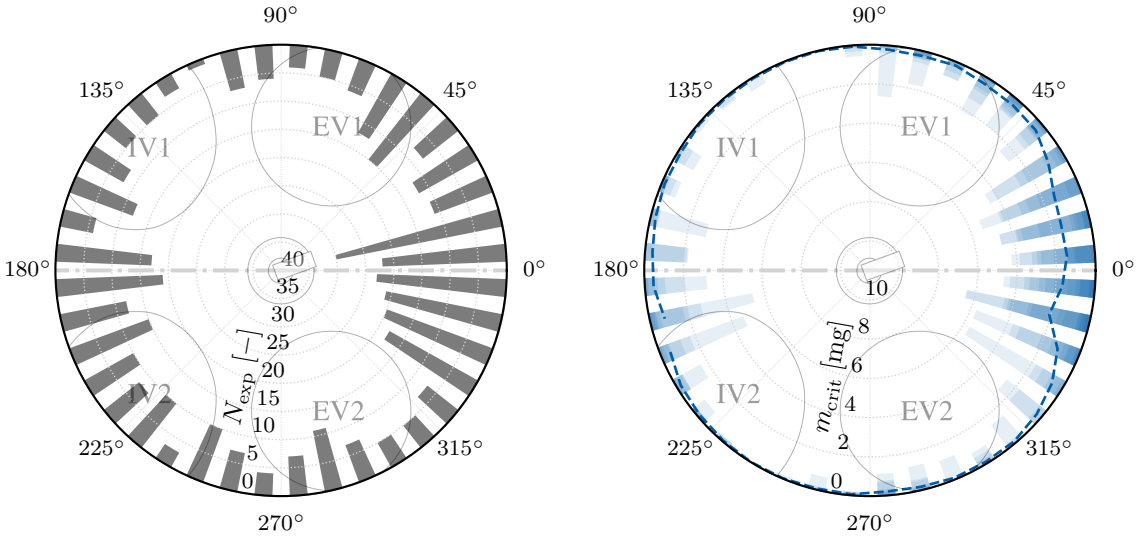

Figure 6.12.: Circumferential distribution of experimentally determined knock initiation direction for isooctane shown on the left side. The right side depicts the circumferential distribution of critical mass at the time of knock onset of each LES realization of isooctane.

In general, the LES results capture the experimental trends in combustion, flame propagation and auto-ignition with good agreement. With that, the LES results form a valuable data set to further investigate the causes of cycle-to-cycle variations as discussed in the next sections.

6.2.2. Global correlations of flow, combustion and auto-ignition

Global correlations of flow, combustion and auto-ignition are analyzed based on the LES data using the Pearson correlation coefficient $R_{x,y}$:

$$R_{x,y} = \frac{\sum_{i=1}^{n}(x_i - \overline{x})(y_i - \overline{y})}{\sqrt{\sum_{i=1}^{n}(x_i - \overline{x})^2}\sqrt{\sum_{i=1}^{n}(y_i - \overline{y})^2}} \,. \tag{6.1}$$

Here, x_i, y_i are individual samples and $\overline{x}, \overline{y}$ the respective means. For the correlation analysis conducted in the following, a set of features based on global and local information is defined. A linear fit is applied to the cycle-individual values of the features x and y. The square of the correlation coefficient, R^2, is used hereafter as an indicator for a linear correlation between the two different features.

Feature selection

A distinct set of features is described for each of the aspects of flow, combustion and auto-ignition. These are listed in Table 6.2 and discussed in detail in the following.

Table 6.2.: List of features used in the correlation analysis. The flow features are listed in the first segment, combustion features in the second segment and auto-ignition features in the last segment. In the following, the colors light grey, grey and dark grey are used to indicate the group to which the features belong. For the positioning of tumble, middle and horizontal plane, see Figure 6.13.

flow	$\lvert\overline{u}\rvert^{\mathrm{SP}}$	Magnitude of velocity
	$\lvert\overline{k}\rvert^{\mathrm{SP}}$	Magnitude of turbulent kinetic energy
	$\alpha_{xy,\overline{u}^{\mathrm{SP}}}$	Angle of velocity components on respective projection planes
	$\alpha_{xz,\overline{u}^{\mathrm{SP}}}$	
	$\alpha_{yz,\overline{u}^{\mathrm{SP}}}$	
combustion	p_{max}	Peak pressure
	$\mathrm{CA}_{\mathrm{p_{max}}}$	Crank angle of peak pressure
	$\mathrm{MFB}^{0.0^\circ\mathrm{CA}}$	Fuel mass fraction burned at TDC
	$\mathrm{MFB}^{16.5^\circ\mathrm{CA}}$	Fuel mass fraction burned at 16.5° CA
	$\Delta x_{\widetilde{c}}^{\mathrm{TP},0.0^\circ\mathrm{CA}}$	Flame width on tumble plane (x-direction)
	$\Delta y_{\widetilde{c}}^{\mathrm{MP},0.0^\circ\mathrm{CA}}$	Flame width on middle plane (y-direction)
	$\Delta x_{\widetilde{c}}^{\mathrm{HP},16.5^\circ\mathrm{CA}}$	Flame width on horizontal plane (z-direction)
auto-ignition	$m_{\mathrm{crit,max}}$	Maximal critical mass
	$\mathrm{CA}_{m_{\mathrm{crit,max}}}$	Crank angle of maximal critical mass
	$\alpha_{xy,m_{\mathrm{crit,max}}}$	Angle of maximal critical mass on horizontal plane

The flow features are based on the convective velocity u and turbulent kinetic energy k in the spark plug gap vicinity at the numerical spark timing ($^{\mathrm{SP}}$). These have been reported to influence the combustion process, e.g. in [21, 63–65, 107]. In this study, velocity and turbulent kinetic energy are time-averaged with an interrogation window of 5° CA to smooth out small-scale turbulent structures. Following Trffuin et al. [64], a radius of 1 mm around the spark plug gap center is considered for the calculation of the features.

The combustion features are divided into two groups distinguishing between the early and late combustion phases. The early combustion phase is assumed up to the time of TDC, at 0.0° CA. The time of 16.5° CA is considered representative of the later combustion phase close to knock onset. As global features, the peak pressure p_{max}, its crank angle $\mathrm{CA}_{\mathrm{p_{max}}}$ and the mass fraction burned $\mathrm{MFB}^{0.0°\mathrm{CA}}$ and $\mathrm{MFB}^{16.5°\mathrm{CA}}$ are considered. Further features are based on the local field of the progress variable $\widetilde{c}$. Three sample planes through the cylinder are considered as shown in Figure 6.13. On the tumble plane (TP, blue), middle plane (MP, red) and horizontal plane (HP, green), the flame is approximated by the $\widetilde{c} = 0.5$ iso-line. Based on this, the distances Δx and Δy, being the difference between the left-most and right-most point in the respective coordinate direction, are calculated as estimates for the flame width. These local features are extracted at TDC, consistently with the first MFB feature. In addition, the evaluation on the horizontal plane is taken at 16.5° CA.

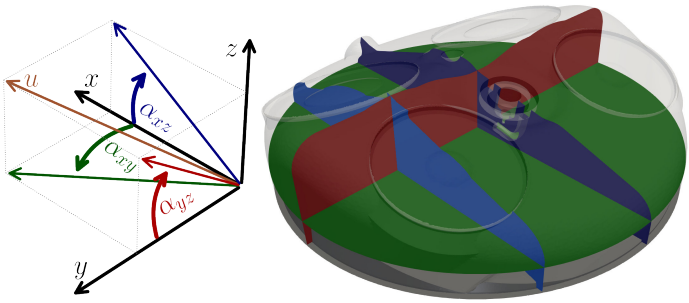

Figure 6.13.: Three sample planes are shown on the right side: tumble plane (blue), middle plane (red) and horizontal plane (green, z-value corresponds to TDC position). The valve plane shown in light blue is considered in the analysis in Section 6.2.3. The left side shows the respective coordinate system and the definition of the angles of the velocity vector (see Table 6.2).

The auto-ignition features are based on the predictions of the auto-ignition model. As global information the maximal critical mass $m_{\mathrm{crit,max}}$ and the respective crank angle $\mathrm{CA}_{m_{\mathrm{crit,max}}}$ are considered as indicators for the knock intensity and the knock onset, respectively. As previously, the most likely knock initiation direction is determined by the circumferential bin with the highest $m_{\mathrm{crit,max}}$ at $\mathrm{CA}_{m_{\mathrm{crit,max}}}$. Following the notation used for the flow features, the direction on the horizontal plane is referred to as $\alpha_{xy,m_{\mathrm{crit,max}}}$.

In the analysis discussed in the following, a permutation of the presented features is used to correlate each feature with all the others. This is used to identify correlations within one group of features and correlations between features from different groups, e.g. flow and combustion features.

Correlations of flow features

At first, the correlations of the flow features are investigated. The R^2 values of all permutations are presented in Table 6.3. The table is colored according to the R^2-value: values of R^2<0.3 are considered uncorrelated, from 0.3 to 1.0 the saturation of green increases linearly. Selected correlations are discussed in the following. The respective scatters of the data and the corresponding linear fits are shown in Figure 6.14.

Table 6.3.: Correlations of flow (light gray) with combustion (gray) and auto-ignition (dark gray) features. The cells are colored according to the respective R^2-value: values of R^2<0.3 are white, and from 0.3 to 1.0 the saturation of green increases linearly.

	$\lvert\overline{u}\rvert^{\mathrm{SP}}$	$\lvert\overline{k}\rvert^{\mathrm{SP}}$	$\alpha_{xy,\overline{u}^{\mathrm{SP}}}$	$\alpha_{xz,\overline{u}^{\mathrm{SP}}}$	$\alpha_{yz,\overline{u}^{\mathrm{SP}}}$
$\lvert\overline{u}\rvert^{\mathrm{SP}}$		0.31	0.0	0.31	0.0
$\lvert\overline{k}\rvert^{\mathrm{SP}}$	0.31		0.07	0.13	0.07
$\alpha_{xy,\overline{u}^{\mathrm{SP}}}$	0.0	0.07		0.01	0.41
$\alpha_{xz,\overline{u}^{\mathrm{SP}}}$	0.31	0.13	0.01		0.01
$\alpha_{yz,\overline{u}^{\mathrm{SP}}}$	0.0	0.07	0.41	0.01	
p_{max}	0.04	0.0	0.01	0.14	0.08
$\mathrm{CA}_{p_{\mathrm{max}}}$	0.07	0.0	0.0	0.18	0.1
$\mathrm{MFB}^{0.0^\circ\mathrm{CA}}$	0.05	0.02	0.03	0.06	0.03
$\mathrm{MFB}^{16.5^\circ\mathrm{CA}}$	0.06	0.0	0.0	0.17	0.08
$\Delta x_{\widetilde{c}}^{\mathrm{TP},0.0^\circ\mathrm{CA}}$	0.01	0.01	0.0	0.12	0.01
$\Delta y_{\widetilde{c}}^{\mathrm{MP},0.0^\circ\mathrm{CA}}$	0.16	0.03	0.02	0.15	0.0
$\Delta x_{\widetilde{c}}^{\mathrm{HP},16.5^\circ\mathrm{CA}}$	0.06	0.0	0.12	0.03	0.01
$m_{\mathrm{crit,max}}$	0.13	0.04	0.03	0.18	0.0
$\mathrm{CA}_{m_{\mathrm{crit,max}}}$	0.1	0.01	0.0	0.19	0.06
$\alpha_{xy,m_{\mathrm{crit,max}}}$	0.01	0.05	0.15	0.0	0.05

Within the flow segment, there is a correlation between $\lvert\overline{u}\rvert^{\mathrm{SP}}$ and $\lvert\overline{k}\rvert^{\mathrm{SP}}$. Higher magnitudes in the resolved convective velocity result in higher sub-grid turbulent kinetic energy (see Figure 6.14). This is not surprising and is associated with the turbulent energy cascade [75]. However, the correlation is not too strong since the instationary nature of the in-cylinder engine flow may lead to the spatial separation between turbulence production and dissipation.

The linear fit in Figure 6.14 suggests that for the flow components projected onto the tumble plane, convection of lower magnitude $\lvert\overline{u}\rvert^{\mathrm{SP}}$ is more likely to be directed towards the cylinder head as indicated by the higher values of $\alpha_{xz,\overline{u}^{\mathrm{SP}}}$. A flow positively deflected from the tumble plane is more likely to be directed towards the cylinder head rather than the piston as indicated by the correlation between the velocity directions $\alpha_{xy,\overline{u}^{\mathrm{SP}}}$ and $\alpha_{yz,\overline{u}^{\mathrm{SP}}}$ (see Figure 6.14).

The absence of clear correlations between the flow and the combustion features is somewhat unexpected. Several publications found correlations between the spark plug velocity magnitude

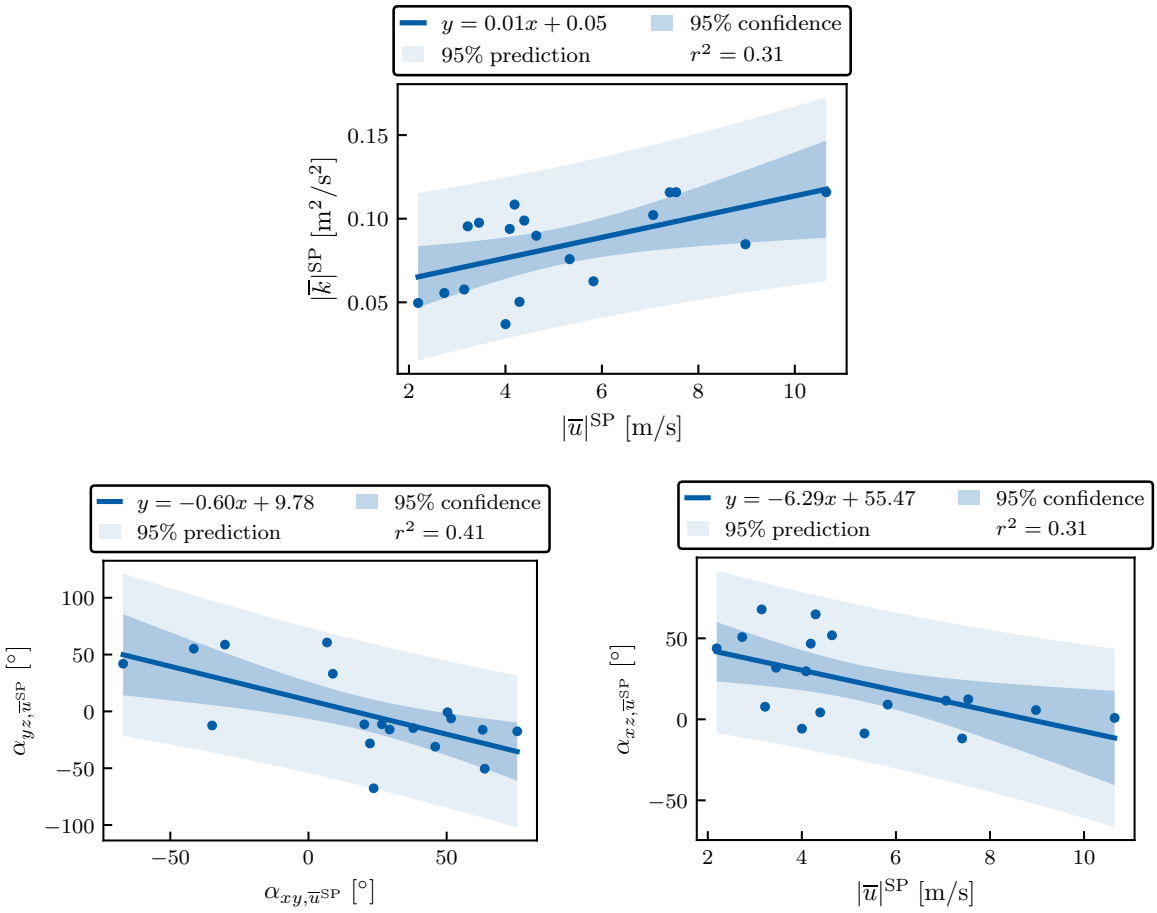

Figure 6.14.: Scatter and linear fit with confidence interval (very light blue) and prediction interval (light blue) for the combination of two flow features (see Table 6.2). Top plot shows velocity magnitude $|\overline{u}|^{\mathrm{SP}}$ and turbulent kinetic energy $|\overline{k}|^{\mathrm{SP}}$. Bottom left shows the velocity directions $\alpha_{xy,\overline{u}^{\mathrm{SP}}}$ and $\alpha_{yz,\overline{u}^{\mathrm{SP}}}$. Bottom right depicts $|\overline{u}|^{\mathrm{SP}}$ and $\alpha_{xz,\overline{u}^{\mathrm{SP}}}$.

and the burning rate (indicated by $p_{\max}$ or MFB), e.g. [21, 63–65, 107]. However, it is important to emphasize that none of these publications claim that the correlations found are generally valid. In contrast, e.g. [64] found different relevance of the investigated features even on the same engine for different operating conditions. This indicates, that the found correlations are not universal and the detailed causes of CCV may vary between engines and operating conditions.

A particular difference results from the engine geometry. The engine investigated in [63, 64] featured a flat piston and a recess between the valves that lead to a tumble-induced vortex structure directly at the spark plug. For the engine investigated in this study, the shaped piston in conjunction with the cylinder head (see Figure 3.1) leads to a different tumble flow.

At the spark timing, the ensemble-averaged velocity magnitude $\langle \overline{u} \rangle$ indicates that the mean tumble center is about 9 mm to the left of the spark plug gap as shown in Figure 6.15. More importantly, this is also the region that exhibits the highest variations in resolved velocity $\langle \overline{u}'^2 \rangle$. Directly to the left of the lower spark electrode, is another area with high variations. However, this area is around 4 mm away from the sphere, which is considering the spark plug vicinity in the feature evaluation.

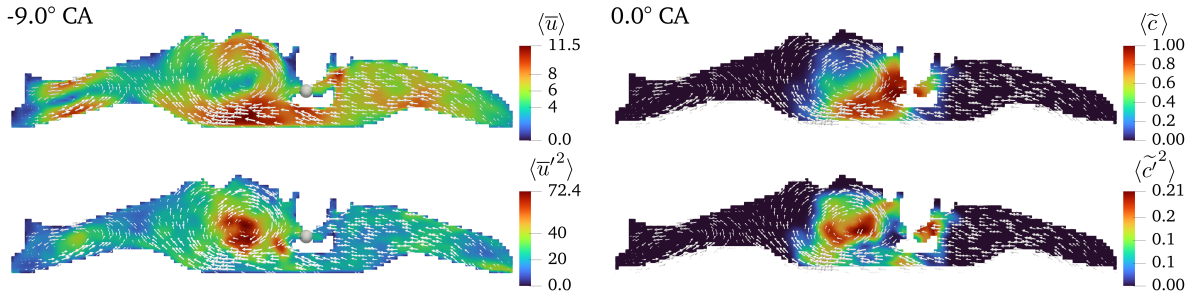

Figure 6.15.: The left side shows the ensemble average of the velocity magnitude $\langle \overline{u} \rangle$ (top) and the respective variations $\langle \overline{u}'^2 \rangle$ (bottom) at spark timing. The arrows indicate the velocity vector and their size is scaled with the velocity magnitude. The sphere considered for the determination of the spark plug features is shown in light gray. The right side depicts the ensemble average of the progress variable $\langle \widetilde{c} \rangle$ (top) and the respective variations $\langle \widetilde{c''^2} \rangle$ (bottom) at TDC. The velocity field at spark timing is indicated by the arrows for orientation.

The influence of these flow structures on flame propagation is apparent considering the tumble plane at TDC, which is shown in Figure 6.15. The ensemble-averaged progress variable $\langle \widetilde{c} \rangle$ can be interpreted as a flame probability here. The mean flame is sucked in by the tumble motion and pushed towards the piston (cf. the velocity arrows that indicate the velocity at spark timing). With that, the main flame volume is left of the spark plug. The highest variations in the flame propagation, expressed as $\langle \widetilde{c''^2} \rangle$, are observed at the position of the mean tumble center at spark timing.

To the right of the spark plug gap, only a small area shows a higher flame probability together with considerable fluctuations. However, the covered area is comparatively smaller, which indicates, that the variations induced by the tumble vortex may have a higher influence on the flame area and hence the burn rate. This may explain, why the convective flow in the spark plug gap is of minor importance for the engine investigated. This hypothesis is further evaluated in Section 6.2.3.

Since there are no clear correlations between the selected flow and combustion features, it is not surprising that no correlations were found between flow and auto-ignition features, since auto-ignition is somewhat of a downstream process from combustion. The respective correlations of the combustion features are discussed in the next paragraph.

Correlations of combustion features

The correlations of the combustion features are summarized in Table 6.4. The correlations between combustion and flow features are discussed above and thus are not included in this table. Selected correlations between the combustion features are discussed below. The respective scatters of the data and the corresponding linear fits are shown in Figure 6.16.

Table 6.4.: Correlations of combustion (gray) and auto-ignition (dark gray) features. The cells are colored according to the respective R^2-value: values of R^2<0.3 are white, and from 0.3 to 1.0 the saturation of green increases linearly.

	p_{max}	$\mathrm{CA}_{p_{\mathrm{max}}}$	$\mathrm{MFB}^{0.0°\mathrm{CA}}$	$\mathrm{MFB}^{16.5°\mathrm{CA}}$	$\Delta x_{\widetilde{c}}^{\mathrm{TP},0.0°\mathrm{CA}}$	$\Delta y_{\widetilde{c}}^{\mathrm{MP},0.0°\mathrm{CA}}$	$\Delta x_{\widetilde{c}}^{\mathrm{HP},16.5°\mathrm{CA}}$
p_{max}		0.96	0.59	0.98	0.39	0.3	0.57
$\mathrm{CA}_{p_{\mathrm{max}}}$	0.96		0.59	0.99	0.33	0.39	0.49
$\mathrm{MFB}^{0.0°\mathrm{CA}}$	0.59	0.59		0.61	0.51	0.31	0.49
$\mathrm{MFB}^{16.5°\mathrm{CA}}$	0.98	0.99	0.61		0.37	0.37	0.53
$\Delta x_{\widetilde{c}}^{\mathrm{TP},0.0°\mathrm{CA}}$	0.39	0.33	0.51	0.37		0.01	0.3
$\Delta y_{\widetilde{c}}^{\mathrm{MP},0.0°\mathrm{CA}}$	0.3	0.39	0.31	0.37	0.01		0.14
$\Delta x_{\widetilde{c}}^{\mathrm{HP},16.5°\mathrm{CA}}$	0.57	0.49	0.49	0.53	0.3	0.14	
$m_{\mathrm{crit,max}}$	0.09	0.2	0.05	0.17	0.0	0.48	0.01
$\mathrm{CA}_{m_{\mathrm{crit,max}}}$	0.95	0.97	0.59	0.98	0.35	0.4	0.58
$\alpha_{xy,m_{\mathrm{crit,max}}}$	0.05	0.02	0.05	0.03	0.06	0.0	0.15

At first, correlations of global combustion features are considered. The linear relation between p_{max} and $\mathrm{CA}_{\mathrm{p_{max}}}$ is known for stable engine operation [108] and reproduced by the LES study (see Figure 6.16). The correlation of the mass fraction burned at 16.5° CA, $\mathrm{MFB}^{16.5°\mathrm{CA}}$ with p_{max} and $\mathrm{CA}_{\mathrm{p_{max}}}$ is attributed to the $\mathrm{MFB}^{16.5°\mathrm{CA}}$ ranging between 40 and 80%. With that, the combustion progressed to a substantial part and hence correlates with the pressure-related features. With the strong interconnection of p_{max}, $\mathrm{CA}_{\mathrm{p_{max}}}$ and $\mathrm{MFB}^{16.5°\mathrm{CA}}$, the feature set may be reduced in future studies.

The indicator for early combustion progress $\mathrm{MFB}^{0.0°\mathrm{CA}}$ ranges between 0.5 and 1.5% in this study. Several studies have shown, that the peak pressure of an individual cycle is determined within the early combustion phase. The correlation of $\mathrm{MFB}^{0.0°\mathrm{CA}}$ to the later-stage combustion feature p_{max} shows, that this is also valid for the operating conditions under investigation here (similar correlations are found to $\mathrm{CA}_{\mathrm{p_{max}}}$ and $\mathrm{MFB}^{16.5°\mathrm{CA}}$). However, the scatter around the linear fit (see Figure 6.16) indicates, that there are relevant influences after this very early combustion stage.

For the flame features based on the local progress variable field $\widetilde{c}$, weak correlations exist between the global mass fraction burned $\mathrm{MFB}^{0.0°\mathrm{CA}}$ and $\mathrm{MFB}^{16.5°\mathrm{CA}}$ and the flame extents at the respective timings $\Delta x_{\widetilde{c}}^{\mathrm{TP},0.0°\mathrm{CA}}$, $\Delta y_{\widetilde{c}}^{\mathrm{MP},0.0°\mathrm{CA}}$ and $\Delta x_{\widetilde{c}}^{\mathrm{HP},16.5°\mathrm{CA}}$. Figure 6.16 exemplarly shows, that the relation between the mass fraction burned $\mathrm{MFB}^{0.0°\mathrm{CA}}$ and the flame width $\Delta x_{\widetilde{c}}^{\mathrm{TP},0.0°\mathrm{CA}}$ is scattered around the linear fit. With that, features based on the projection of the flame onto a plane cannot generally be used as an indicator of the global combustion progress.

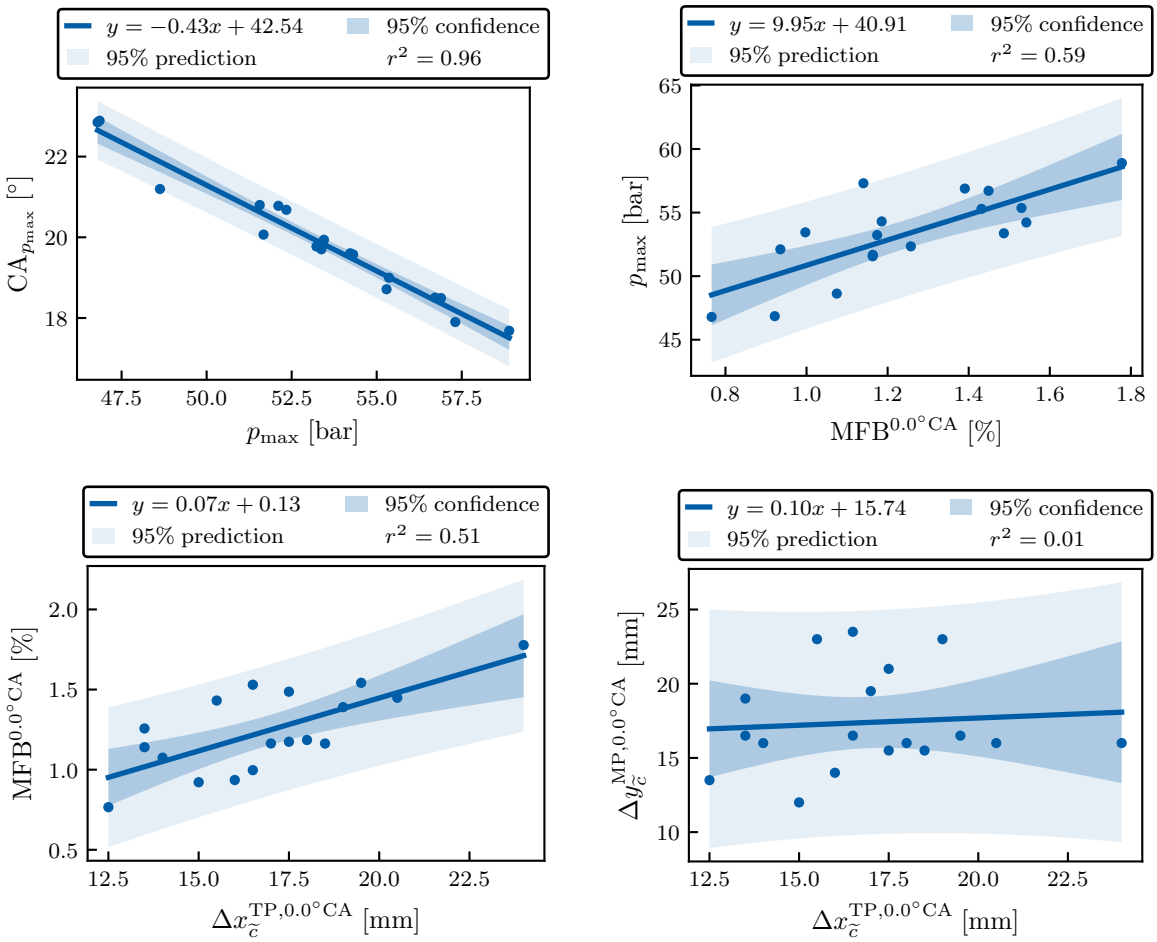

Figure 6.16.: Scatter and linear fit with confidence interval (very light blue) and prediction interval (light blue) for a combination of two combustion features (see Table 6.2). Top left shows peak pressure p_{max} and crank angle of peak pressure $\mathrm{CA}_{p_{max}}$. The top right shows the mass fraction burned at TDC $\mathrm{MFB}^{0.0°\mathrm{CA}}$ and peak pressure p_{max}. The bottom left shows the flame width on the tumble plane (x-direction) at TDC $\Delta x_{\widetilde{c}}^{\mathrm{TP},0.0°\mathrm{CA}}$ and $\mathrm{MFB}^{0.0°\mathrm{CA}}$. Bottom right depicts $\Delta x_{\widetilde{c}}^{\mathrm{TP},0.0°\mathrm{CA}}$ and the flame width on the middle plane (y-direction) at TDC $\Delta y_{\widetilde{c}}^{\mathrm{HP},0.0°\mathrm{CA}}$.

This is attributed to the non-symmetric flame propagation in the direction of the tumble plane and perpendicular to it, which is indicated by the absence of correlation between $\Delta x_{\widetilde{c}}^{\mathrm{TP},0.0°\mathrm{CA}}$ and $\Delta y_{\widetilde{c}}^{\mathrm{HP},0.0°\mathrm{CA}}$ (see Figure 6.16).

Finally, the correlations to the auto-ignition features are discussed. The close relationship between the auto-ignition and the combustion process is reflected in the correlation between the crank angle of knock onset $\mathrm{CA}_{m_{crit,max}}$ and all combustion features. High correlations are found to global or late-combustion features, e.g., p_{max} and $\mathrm{MFB}^{16.5°\mathrm{CA}}$. Weaker correlations

exist to the local or early-combustion features, e.g., $\mathrm{MFB}^{0.0°\mathrm{CA}}$ and $\Delta x_{\widetilde{c}}^{\mathrm{TP},0.0°\mathrm{CA}}$. Given the previous findings, this is reasonable.

No correlations are found for the direction of the highest critical mass at knock onset $\alpha_{xy,m_{\mathrm{crit,max}}}$. This indicates, that the variations observed in the knock initiation direction are not attributed to the global combustion process but rather to local processes. In this regard, the correlation between the maximum critical mass $m_{\mathrm{crit,max}}$ and the flame width in the y-direction projected on the middle plane at TDC $\Delta y_{\widetilde{c}}^{\mathrm{MP},0.0°\mathrm{CA}}$ is of interest. The linear fit shown in Figure 6.17 suggests that higher early flame width in y-direction (perpendicular to the tumble plane) leads to higher critical mass at knock onset. This is further investigated in Section 6.2.3.

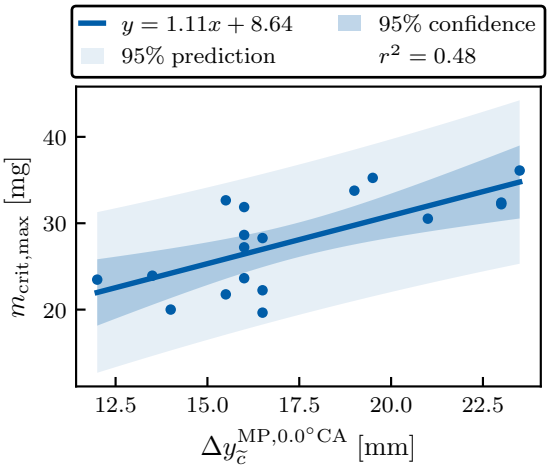

Figure 6.17.: Scatter and linear fit with confidence interval (very light blue) and prediction interval (light blue) for the flame width on the middle plane (y-direction) at TDC $\Delta y_{\widetilde{c}}^{\mathrm{MP},0.0°\mathrm{CA}}$ and the maximal critical mass $m_{\mathrm{crit,max}}$.

Correlations of auto-ignition features

The correlations of the auto-ignition features are summarized in Table 6.5. The correlations to combustion and flow features have been discussed previously and thus are not included in this table.

Table 6.5.: Correlations of auto-ignition features (dark gray). The cells are colored according to the respective R^2-value: values of R^2<0.3 are white.

	$m_{\mathrm{crit,max}}$	$\mathrm{CA}_{m_{\mathrm{crit,max}}}$	$\alpha_{xy,m_{\mathrm{crit,max}}}$
$m_{\mathrm{crit,max}}$		0.2	0.03
$\mathrm{CA}_{m_{\mathrm{crit,max}}}$	0.2		0.02
$\alpha_{xy,m_{\mathrm{crit,max}}}$	0.03	0.02	

The absence of correlations between the individual auto-ignition features is reasonable and expected based on the discussion of the results in Section 6.2.1. However, it indicates potential limitations of the correlation method. It is well known that knock onset and knock intensity are not linearly related, however, higher knock intensities are only observed at earlier knock onsets (see Figure 6.9). A manual inspection of all permutations is required as such trends cannot be captured with the linear fit applied, and improved regression models taking into account non-linearity may be needed [64]. Hanuschkin et al. demonstrated that the usage of machine learning techniques for such purposes is possible [60], which could be employed in future studies.

Conclusions

The correlation analysis provides a good global characterization of flow, combustion and auto-ignition for the operating conditions under investigation. However, two aspects point to the importance of local structures for the observed knocking combustion. Firstly, the convective flow in the spark plug gap vicinity does not correlate with the global combustion progress. It is hypothesized that the local tumble velocity field is of greater importance here. Secondly, the early-stage flame propagation perpendicular to the tumble plane correlates with the auto-igniting mass. Both aspects are examined in greater detail in the following.

6.2.3. Local correlations of flow, combustion and auto-ignition

In a further analysis, the previously described correlation analysis is extended. Now, the correlation coefficient R (see Equation 6.1) is calculated for every cell of the 2-D domain resembling the sample planes shown in Figure 6.13. Here, the scalar features described in Table 6.2 are correlated to the fields of velocity $\overline{u}$, combustion progress $\widetilde{c}$ and auto-ignition progress $\widetilde{c}_\mathrm{I}$ for selected time-steps to identify local structures of correlations. In addition, a H_0-hypothesis test is performed based on the t-distribution of the test statistics. A significant correlation is assumed only for $p\text{-values}$ lower than the significance level of 0.05.

Relevance of tumble flow

First, the correlation of spark plug convective velocity at spark timing and the early flame propagation at TDC is analyzed. The respective velocity fields and flame probabilities have been shown in Figure 6.15.

The correlation $R_{\widetilde{c}\leftrightarrow|\overline{u}|^\mathrm{SP}}$ shown in Figure 6.18 indicates that the combustion progress c does not correlate with the spark plug velocity magnitude $|\overline{u}|^\mathrm{SP}$ for the majority of the area with a high flame probability (see Figure 6.15). A region with a strong correlation is located to the right of the spark plug. However, the area of significant correlation (outlined in white) is very small. Thus, only a minor part of the overall early flame propagation is influenced, so that no significant influence on early- and thus later-stage combustion is expected, which supports the previous findings.

Figure 6.18.: Correlation coefficient $R_{\widetilde{c}\leftrightarrow|\overline{u}|^\mathrm{SP}}$ between combustion progress $\widetilde{c}$ and spark plug velocity magnitude $|\overline{u}|^\mathrm{SP}$ on the tumble plane at TDC. The outlines of areas considered significantly correlated ($p\text{-value} < 0.05$) are shown in white color.

On the other hand, correlations between the velocity field at spark timing (see Figure 6.15) and flame features imply the relevance of the tumble motion for the combustion progress. Figure 6.19 shows the correlations between the z-component of velocity $\overline{u}_z$ with the early flame propagation feature $\Delta y_{\widetilde{c}}^{\mathrm{MP},0.0°\mathrm{CA}}$ and the late-combustion feature p_max. For both, the main correlations are found within the tumble motion region. In contrast, for the spark plug gap vicinity, there are no significant correlations. The correlation $R_{\overline{u}_z\leftrightarrow\Delta y_{\widetilde{c}}^{\mathrm{MP},0.0°\mathrm{CA}}}$ appears in the area of highest velocity fluctuations within the tumble center, whereas the correlation $R_{\overline{u}_z\leftrightarrow p_\mathrm{max}}$ is highest within the area of highest velocity magnitude of the tumble motion. With that, both the tumble strength as well as fluctuations of the tumble position seem to influence the combustion process.

To illustrate the response of the early flame propagation on different tumble motions, two single cycles are compared in Figure 6.20. The velocity at spark timing is illustrated by the white arrows, that are scaled with the velocity magnitude. The cycles have the same $\mathrm{MFB}^{0.0°\mathrm{CA}}$ of

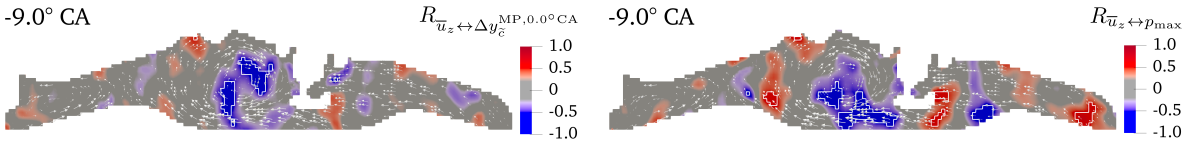

Figure 6.19.: Correlation coefficients $R_{\overline{u}_z \leftrightarrow \Delta y_{\widetilde{c}}^{\mathrm{MP},0.0^\circ\mathrm{CA}}}$ (left) and $R_{\overline{u}_z \leftrightarrow p_{\max}}$ (right) on the tumble plane at -9.0° CA. The outlines of areas considered significantly correlated (p-value < 0.05) are shown in white color. The arrows indicate the velocity vector and their size is scaled with the velocity magnitude.

1.2% but a different $\Delta y_{\widetilde{c}}^{\mathrm{MP},0.0^\circ\mathrm{CA}}$ (15.5 and 19.5 mm, respectively; see Table 6.6). This indicates the same global early flame propagation, albeit with local differences.

For *Cycle A* (shown on the top), the tumble center is close to the middle plane and at the same height as the spark plug gap. The downward-directed flow of the tumble pushes the flame toward the piston. It is first stretched along the piston surface and then follows the upward-directed tumble flow. The projection on the middle plane shows a flame elongated in the y-direction (perpendicular to the tumble plane) with a low height (extent in the z-direction).

Cycle B (shown on the bottom) experiences a different flow field. The tumble center is close to the top of the cylinder head and relatively far away from the spark plug. The flame follows the main flow direction along the piston surface. In the middle plane projection, the flame surface area is larger with greater extents in both y- and z-direction.

While these differences in the local early flame propagation do not significantly influence the global burn rate and result in a similar peak pressure (51.6 and 51.7 bar, respectively), they may influence the local and thus the global auto-ignition progress as discussed in Section 6.2.3.

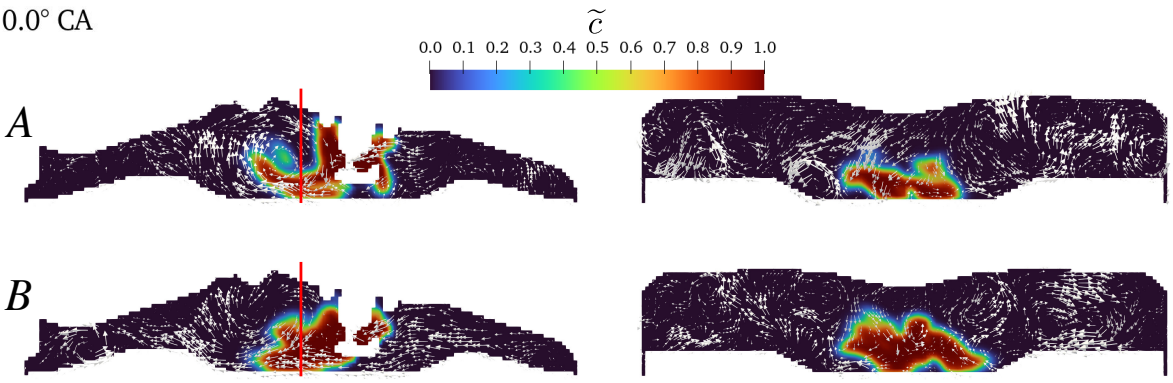

Figure 6.20.: Combustion progress $\widetilde{c}$ at TDC on tumble plane (left) and middle plane (right) for two different LES realizations. Top shows *Cycle A*, bottom *Cycle B* (see Table 6.6). The location of the middle plane on the tumble plane is illustrated by a vertical red line. The arrows indicate the velocity vectors at spark timing and their size is scaled with the velocity magnitude.

In summary, it seems that the tumble motion at the time of spark ignition influences the

combustion. However, the tumble motion is essentially a large-scale flow structure that develops after the intake valves have opened, particularly during the compression phase. It is therefore further investigated whether flow structures that occur earlier than the spark timing also show correlations with the combustion progress.

At -190.7° CA, the piston is close to BDC and the ensemble-averaged velocity magnitude $\langle \overline{u} \rangle$ indicates the existence of a strong tumble motion, as shown in Figure 6.21. For the correlations of the z-component of velocity $\overline{u}_z$ with the flame width in x-direction at TDC $\Delta x_{\widetilde{c}}^{\mathrm{TP},0.0°\mathrm{CA}}$ an alignment with the tumble motion is observed. This indicates that a stronger upward-directed velocity leads to a more stretched flame at TDC in the x-direction.

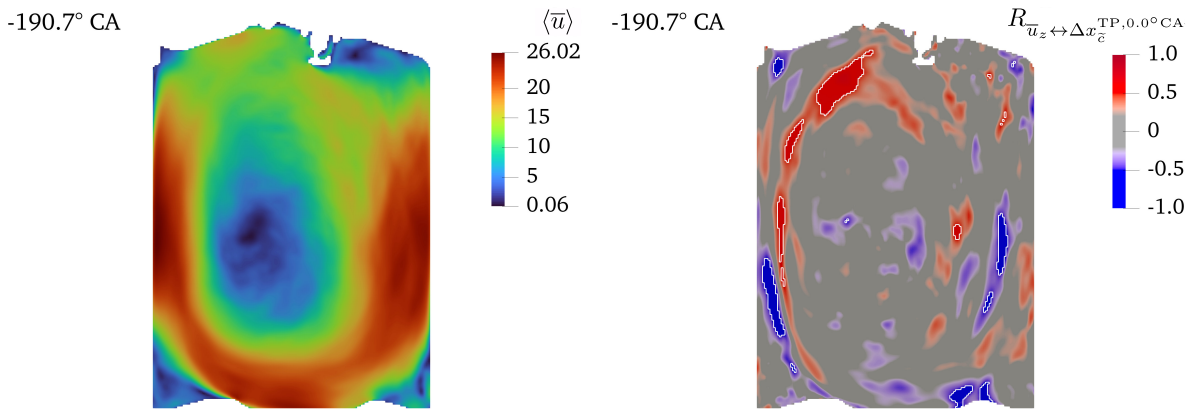

Figure 6.21.: Ensemble average of the velocity magnitude $\langle \overline{u} \rangle$ (left) and correlation coefficient $R_{\overline{u}_z \leftrightarrow \Delta x_{\widetilde{c}}^{\mathrm{TP},0.0°\mathrm{CA}}}$ (right) on the tumble plane at -190.7° CA. The outlines of areas considered significantly correlated (p-value < 0.05) are shown in white color.

For the time of -276.8° CA, the intake valves are open and an intake valve jet has formed. The respective ensemble-averaged velocity field $\langle \overline{u} \rangle$ on the valve plane (see Figure 6.13) is shown in Figure 6.22. The correlation of the z-component of velocity and flame width in x-direction at TDC is aligned to the valve jet structure. With that, as early as during the intake valve open phase, local large-scale flow structures are observed to correlate with the following combustion phase.

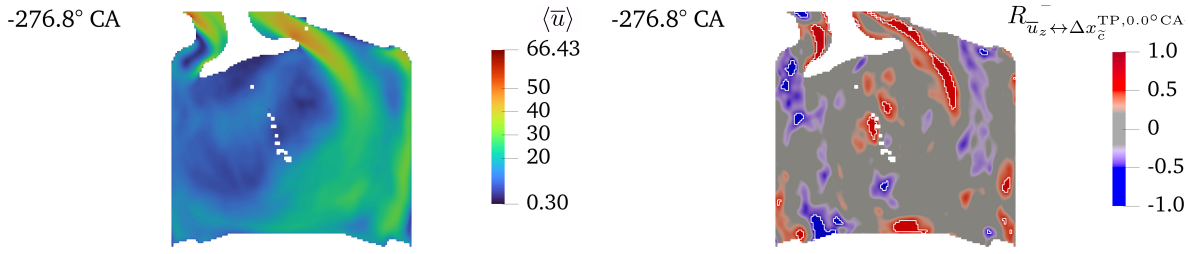

Figure 6.22.: Ensemble average of the velocity magnitude $\langle \overline{u} \rangle$ (left) and correlation coefficient $R_{\overline{u}_z \leftrightarrow \Delta x_{\widetilde{c}}^{\mathrm{TP},0.0°\mathrm{CA}}}$ (right) on the valve plane at -276.8° CA. The outlines of areas considered significantly correlated (p-value < 0.05) are shown in white color.

The current analysis is limited to exemplary time steps. For future studies, a methodology similar to that of Engelmann et al. [109] could be employed, in which Lagrangian particles are traced to capture the spatially and temporally resolved convective history. Alternatively, the tracing of the tumble center [110] or flow features based on coherent vortex structures [67] may provide further insides.

Correlation between early flame propagation and auto-igniting process

The correlation analysis in Section 6.2.2 suggests a relation between the flame width in y-direction on the middle plane (see Figure 6.13) at TDC $\Delta y_{\widetilde{c}}^{\mathrm{MP},0.0^\circ\mathrm{CA}}$ and the amount of mass undergoing auto-ignition $m_{\mathrm{crit,max}}$. This relation is further investigated in the following.

The ensemble-averaged auto-ignition progress variable $\langle \widetilde{c}_\mathrm{I} \rangle$ is shown in Figure 6.23 for the horizontal plane at 16.5° CA. The main auto-ignition progress is observed on the exhaust valve side around the tumble plane. This agrees with the circumferential distribution of critical mass for the individual cycles (see Figure 6.11), where the respective time of knock onset has been considered. The close relationship between auto-ignition and combustion progress is evident when considering the flame probability $\langle \widetilde{c} \rangle$ (see Figure 6.23). Auto-ignition progress is observed for the entire region between the flame front and the liner, as the pockets of the unburned mixture undergo auto-ignition. The high probability of auto-ignition between the exhaust valves seems related to the flame propagation that reaches this part of the cylinder later than other regions. Although showing comparably low flame probability, the regions between the exhaust and intake valve on either side show less auto-ignition probability. This aspect is further investigated in the following.

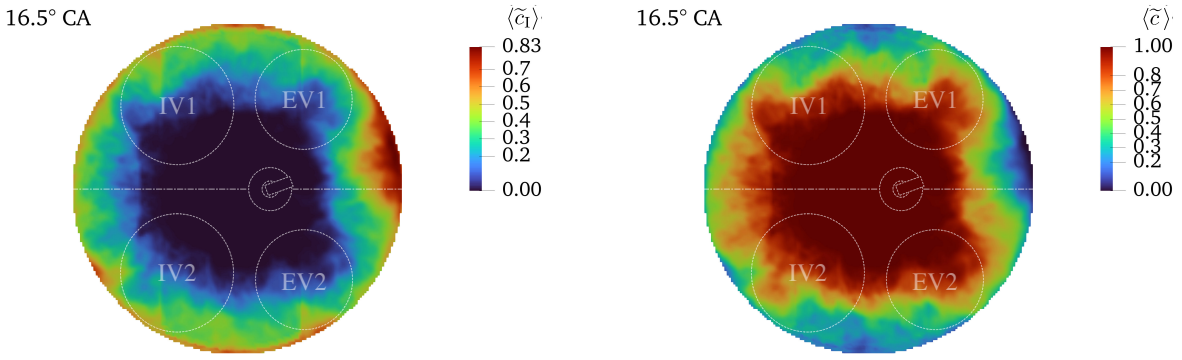

Figure 6.23.: Ensemble average of the auto-ignition progress $\langle \widetilde{c}_\mathrm{I} \rangle$ (left) and the combustion progress $\langle \widetilde{c} \rangle$ (right) on the horizontal plane at 16.5° CA. The view is in the direction of the cylinder head. Locations of the valves and the spark plug are illustrated for orientation. The dash-dotted line indicates the tumble plane.

s

First, the correlation between the local auto-ignition progress $\widetilde{c}_\mathrm{I}$ and the global maximum critical mass $m_{\mathrm{crit,max}}$ is investigated. The respective correlation field $R_{\widetilde{c}_\mathrm{I} \leftrightarrow m_{\mathrm{crit,max}}}$ is shown in Figure 6.24. The region of the highest average auto-ignition progress $\langle \widetilde{c}_\mathrm{I} \rangle$ (see Figure 6.23) is positively correlated to the maximal critical mass, as expected. Interestingly, another distinctive

area of correlation $R_{\widetilde{c}_\mathrm{I} \leftrightarrow m_\mathrm{crit,max}}$ is found in the region between the intake and exhaust valve (IV1 and EV1, see Figure 6.24). However, the sign is reversed, i.e., a higher local auto-ignition progress $\widetilde{c}_\mathrm{I}$ in this area, correlates with a lower global critical mass.

The auto-ignition progress in this particular region in turn is correlated to the flame width $\Delta y_{\widetilde{c}}^{\mathrm{MP},0.0^\circ\mathrm{CA}}$. Hence, a higher flame propagation perpendicular to the tumble plane in the early-combustion phase correlates with a lower auto-ignition progress in this region in the late-combustion phase. This is a link to the previously discussed global correlation between $\Delta y_{\widetilde{c}}^{\mathrm{MP},0.0^\circ\mathrm{CA}}$ and $m_\mathrm{crit,max}$ in Section 6.2.2.

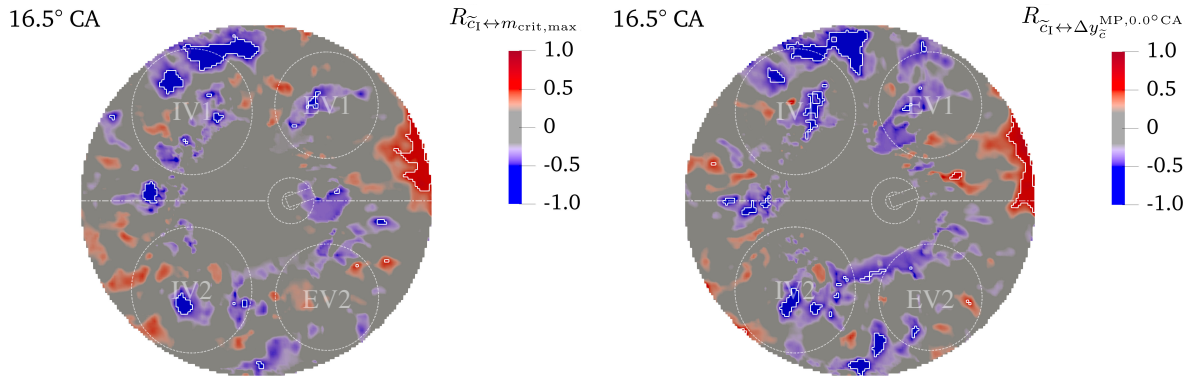

Figure 6.24.: Correlation coefficients $R_{\widetilde{c}_\mathrm{I} \leftrightarrow m_\mathrm{crit,max}}$ (left) and $R_{\widetilde{c}_\mathrm{I} \leftrightarrow \Delta y_{\widetilde{c}}^{\mathrm{MP},0.0^\circ\mathrm{CA}}}$ (right) on the horizontal plane at 16.5° CA. The outlines of areas considered significantly correlated (p-value < 0.05) are shown in white color. The view is in the direction of the cylinder head. Locations of the valves and the spark plug are illustrated for orientation. The dash-dotted line indicates the tumble plane.

The further investigation of this correlation is based on the comparison of two individual cycles. The same cycles as considered for the investigation of the influence of the tumble on the early flame propagation (see Figure 6.20) are chosen. The selection ensures a similar global early- and later-stage combustion progress (cf. $\mathrm{MFB}^{0.0^\circ\mathrm{CA}}$ and p_max or $\mathrm{MFB}^{18.5^\circ\mathrm{CA}}$, respectively). The reference time of 18.5° CA is chosen based on the predicted slightly earlier knock onset of *Cycle A*. The main differences are the early flame width $\Delta y_{\widetilde{c}}^{\mathrm{MP},0.0^\circ\mathrm{CA}}$ and the amount of critical mass, following the implications of the previously found correlation. The individual values for the mentioned features are summarized in Table 6.6.

Table 6.6.: Values of features of single cycles *A* and *B*

	$\mathrm{MFB}^{0.0^\circ\mathrm{CA}}$ [%]	$\mathrm{MFB}^{18.5^\circ\mathrm{CA}}$ [%]	p_max [bar]	$\Delta y_{\widetilde{c}}^{\mathrm{MP},0.0^\circ\mathrm{CA}}$ [mm]	$m_\mathrm{crit,max}$ [mg]	$\mathrm{CA}_{m_\mathrm{crit,max}}$ [°]
Cycle A	1.2	72.1	51.6	15.5	21.8	19.3
Cycle B	1.2	74.0	51.7	19.5	35.3	18.5

For the time of 18.5° CA, flame propagation and auto-ignition progress are compared based on the horizontal plane (see Figure 6.13). In Figure 6.25, the flame front is defined by $\widetilde{c} = 0.5$ and visualized as a white iso-line. The coloring of the auto-ignition $\widetilde{c}_\mathrm{I}$ is adjusted to highlight solely the areas contributing to the critical mass ($\widetilde{c}_\mathrm{I} \geq 0.95$).

The global combustion progress $\mathrm{MFB}^{18.5°\mathrm{CA}}$ is comparable and so is the global flame propagation on the horizontal plane. However, the different local flame propagation leads to different locations and sizes of the pockets of unburned mixture ahead of the flame front. A substantial part of the unburned mixture is identified as auto-igniting in the pockets in the direction of the exhaust valves and the intake valves. In contrast, the pockets towards the region between the exhaust and intake valve on either side contribute little to nothing to the critical mass despite their comparable size. The difference in the auto-ignition progress is attributed to the slight difference in the unburned temperature $\widetilde{T}_\mathrm{u}$. The unburned temperature is above 850 K and thereby it is outside of the NTC limit. Hence, relatively small temperature differences can lead to a strong change in reactivity (see Figure 3.4). As a result, the higher temperatures towards the respective ends of the tumble plane lead to faster auto-ignition than in the pockets between the exhaust and intake valve on either side. The local differences in the unburned temperature are presumably related to the non-uniform shape of the piston (see Figure 3.1), which leads to different distances between the auto-ignition areas and the cooled piston surface and thus influences the heat losses to the cold wall.

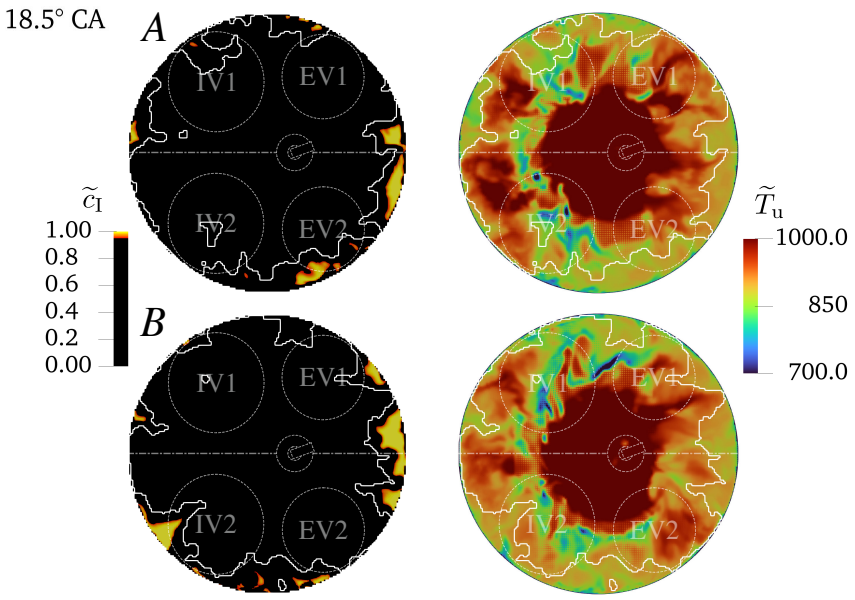

Figure 6.25.: Auto-ignition progress $\widetilde{c}_\mathrm{I}$ (left) and unburned temperature $\widetilde{T}_\mathrm{u}$ (right) for two different LES realizations on the horizontal plane at 18.5° CA. Top shows *Cycle A*, bottom *Cycle B* (see Table 6.6). The flame front defined by $\widetilde{c} = 0.5$ is visualized as a white iso-line. For $\widetilde{c}_\mathrm{I} \geq 0.95$, colors are defined, and the values below are black. The view is in the direction of the cylinder head. Locations of the valves and the spark plug are illustrated for orientation. The dash-dotted line indicates the tumble plane.

Consequently, the local flame propagation is influencing the amount of unburned mixture undergoing auto-ignition. For the same global burn rate, faster flame propagation perpendicular to the tumble plane (in y-direction) leads to lower consumption of unburned mixture in the direction of the tumble plane (x-direction). Thus, pockets of unburned mixture with a relatively slow auto-ignition process (between the exhaust and intake valve on either side) are consumed while pockets of high reactivity persist (in the direction of the exhaust valves and intake valves). The correlation found between $m_{\mathrm{crit,max}}$ and $\Delta x_{\widetilde{c}}^{\mathrm{MP},0.0^{\circ}\mathrm{CA}}$ indicates that this imbalance in flame propagation has already developed in the early combustion phase. Therefore, the cycle-to-cycle variations in the local early flame propagation influence the cycle-to-cycle variations in the global auto-ignition process.

6.2.4. Conclusions on influence of cycle-to-cyle variations on knocking combustion initiation

The influence of cycle-to-cycle variations on knocking combustion initiation is investigated in a multi-cycle LES study taking into account different initial flow conditions. The surrogate fuels TRF-OS and isooctane are investigated, whereby the discussion is mainly based on the former due to comparable findings. The experimental observations on combustion and auto-ignition are captured with good agreement. This applies to both the main trends and the cycle-to-cycle variations. The circumferential distribution of the auto-igniting mass predicted by the LES is identified as a promising indicator of the experimentally determined frequencies of the knock initiation direction for both surrogate fuels. Subsequently, the correlations between flow, combustion and auto-ignition are investigated. The main findings are summarized as follows:

- The overall burn rate of an individual cycle is determined by the early combustion phase.
- The flow near the spark plug at ignition timing does not correlate with the combustion progress.
- The average early flame propagation indicates the relevance of the tumble region for cycle-to-cycle variations.
- Respective local correlations are found connecting the velocity within the tumble region at spark timing with the further combustion progress.
- Similar correlations associated with large-scale flow structures such as the intake valve jet are found for times well before combustion.
- Shortly after spark ignition, the global speed is determined at which the flame subsequently propagates in the direction of the tumble plane or perpendicular to it.
- Consequently, the location of the pockets of unburned mixture in the late combustion phase is already decided by the imbalance of the early flame propagation direction.
- The reactivity and thus the auto-ignition progress within these pockets of unburned mixture varies due to differences in heat loss to the piston surface.

In summary, the results show that cycle-to-cycle variations in the large-scale flow structures influence the flame propagation. These cycle-to-cycle variations in the local flame propagation in turn influence the subsequent local and thus the global auto-ignition process.

7. Conclusions and outlook

In this thesis, knocking combustion initiation at the knock limit for surrogate fuels with NTC behavior is systematically investigated. A comprehensive experimental database on the knocking combustion behavior of different fuels is used for further analysis of specific aspects and operating conditions based on simulations. Numerical investigations are performed to analyze the global and local auto-ignition processes and to investigate the cause-and-effect chain of cycle-to-cycle variations in knocking combustion initiation. For that, simulation setups of increasing complexity are considered and suitable models are developed.

The first analysis is based on the experimental database systematically investigating the differences in the global knocking combustion behavior between three surrogate fuels in comparison to conventional gasoline fuel. Indications are found for the influence of the NTC behavior on the knock resistance. A subsequent model-based analysis of the fuel influence on combustion and auto-ignition behavior shows, that the auto-ignition delay times of the surrogate fuels do not correspond to the order of their knock resistance. However, the thermodynamic conditions are mostly within the negative temperature coefficient (NTC) regime. There are indications that, due to the NTC behavior, a different mechanism of knocking combustion initiation may exist for the surrogate fuel TRF-OS, which showed the lowest knock resistance in the experimental campaign.

To capture the non-linear auto-ignition evolution that occurs for surrogate fuels with NTC behavior, an existing auto-ignition precursor model is extended. The respective source term formulation is evaluated based on a DNS dataset. Subsequently, this auto-ignition model is applied and validated in 0-D configurations. The observed two-stage auto-ignition process associated with the NTC behavior can only be captured properly with the modified non-linear source term formulation of the new model.

Hereafter, the auto-ignition model is applied in two multi-cycle LES studies. Again, the surrogate fuel TRF-OS is considered which showed deviations in the knock characteristics in the previous study. Using the detailed insights from the LES the influence of local influences on the knocking combustion initiation are elucidated.

The first LES study investigates the effect of temperature stratification and flame propagation on the local auto-ignition process under thermodynamic conditions in the NTC regime. The auto-ignition model captures the trends of the experimentally obtained global knock characteristics with good agreement. In addition, it is found that the NTC behavior affects the local auto-ignition process in the unburned mixture leading to a widespread two-stage auto-ignition. Subsequently, the auto-igniting mixture is rapidly consumed by the flame, which makes detonation waves

unlikely to occur. Thus, the amount of auto-igniting mass is directly related to the experimentally observed knock intensity. With that, the flame propagation determines the location and amount of the auto-igniting mass.

This aspect is further investigated in a second multi-cycle LES study which takes different initial flow conditions for the combustion phase into account. In addition to TRF-OS, isooctane is considered, whereby the discussion is mainly based on the former due to comparable findings. The focus is on the resulting cycle-to-cycle variations of turbulent flame propagation and thus the combustion and auto-ignition process. From the respective experimental campaign, in addition to global quantities, local information on the knock initiation direction is available by employing a fiber-optical spark plug. The predictions of the LES agree well with the experiments in terms of the mean values and cycle-to-cycle variations of the global properties such as peak pressure and knock onset. For statistics of the knock initiation direction, the circumferential distribution of the auto-igniting mass is identified as a promising indicator for both surrogate fuels. Subsequently, correlations between flow, combustion and auto-ignition are analyzed. These indicate that the overall burn rate is determined by the early-combustion phase. The flame propagation in turn is correlated with large-scale flow structures before spark timing and local differences in the velocity within the tumble region at spark timing. In the early-combustion phase, the global speed at which the flame subsequently propagates along the tumble plane or perpendicular to it is determined, and thus the locations of the pockets of the unburned mixture in the later stages. Due to differences in reactivity and hence in the auto-ignition process within these pockets, cycle-to-cycle variations of the local flame propagation lead to a locally and thus globally different auto-ignition process.

In summary, the insights gained in this thesis present significant advancements in understanding the cause-and-effect chain of knocking combustion initiation of surrogate fuels with NTC behavior for operating conditions at the knock limit. Future studies could either extend this to further operating conditions or different fuels. The investigation of synthetic renewable fuels is particularly promising. A more detailed understanding of the knocking behavior paves the way for an optimization of the fuel composition or the combustion process, leading to improved combustion efficiency.

A. Appendix

A.1. Evaluation of the *detailed gKIM* model based on a DNS dataset[1]

The evaluation of the *detailed gKIM* model is performed utilizing a DNS dataset[2]. The study focuses on two main aspects. First, an *a-priori* analysis is conducted followed by the investigation of the spatial turbulent fluctuations and the respective implications for the turbulence-chemistry interaction (TCI) modeling.

A.1.1. DNS setup

A DNS considering the turbulent auto-ignition process under engine-relevant conditions has been conducted by Hongchao Chu at ITV using the in-house solver *CIAO*. The setup of the DNS is based on the study of Mittal et al. [112]. The two-dimensional domain is $1.3 \times 1.3\,\mathrm{mm}$ resolved by 1024 cells in each direction. The DNS captures the turbulent auto-ignition process of a premixed stoichiometric isooctane-air mixture with 5% EGR mass fraction. As initial conditions, a pressure of $p_0 = 55\,\mathrm{bar}$ and a mean temperature of $\overline{T}_0 = 1000\,\mathrm{K}$ are chosen. Using the approach of the study by Mittal et al. [112], a stratification of $\pm 50\,\mathrm{K}$ is employed for the temperature field, and the velocity field is initialized with fluctuations of $\approx \pm 1.5\,\mathrm{m/s}$. The initial temperature field and velocity field (of the component in x-direction) of the DNS are depicted in Figure A.1.

Periodic boundary conditions and an adaptive time-stepping method are used. To capture the chemistry, a detailed reaction mechanism based on Jerzembeck et al. [113] is employed, which contains 173 species and 865 reactions. The diffusion modeling is based on the unity Lewis assumption.

A.1.2. Discussion of physical phenomena

The temporal and spatial development of the fuel mass fraction Y_f and temperature T are shown in Figure A.2. The initial velocity field leads to a distortion of the initial temperature stratification (cf. Figure A.1). At $t = 0.48\,\mathrm{ms}$ regions of higher temperature are distributed throughout the domain. The associated fuel mass fraction Y_f is below the initial stoichiometric

[1] This Section is partly based on the results of the bachelor's thesis of Andreas Lindenthal [111] that I supervised together with Matthias Steinhausen.

[2] The DNS dataset was provided by the research partners at the Institute for Combustion Technology (ITV), RWTH Aachen University.

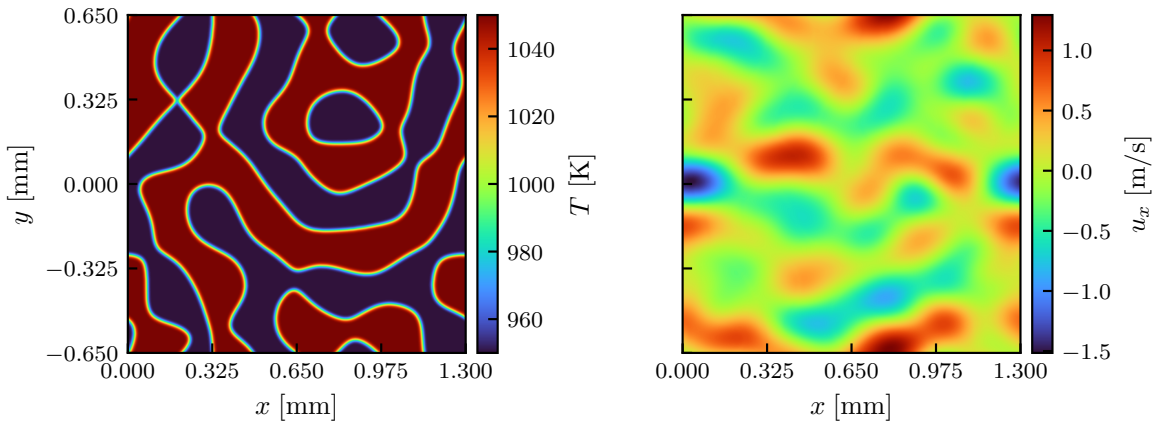

Figure A.1.: Initial temperature T_0 (left) and velocity $u_{x,0}$ (right).

value $Y_{\mathrm{f},0} = 0.0585$, indicating the onset of fuel conversion. In particular, a hot spot has developed ($x = 0.12\,\mathrm{mm}, y = 0.195\,\mathrm{mm}$) showing the highest temperature and the lowest fuel mass fraction. At $t = 0.51\,\mathrm{ms}$, the fuel is fully converted in the center of the hot spot (cf. white circle in Y_f field) indicating the first successful auto-ignition. Thereafter, the reaction front spreads from the first hot spot location, while new auto-ignition locations appear in the entire domain.

The respective temporal development of the mean as well as extreme values of Y_f, T and p are shown in Figure A.3.

- *Pre-ignition stage*: Numerical artifacts resulting from initialization decay within $t_\mathrm{init} = 0.14\,\mathrm{ms}$.
- *Auto-ignition stage*: After $t = 0.14\,\mathrm{ms}$, the fuel is consumed over time and $\overline{Y}_\mathrm{f}$ decreases accoridngly. The temperature stratification is apparent in the difference between T_min and T_max. No spatial fluctuations are observed for p, as expected. With the first successful local auto-ignition at $t_\mathrm{ign} = 0.51\,\mathrm{ms}$, the fuel is locally fully consumed and $Y_\mathrm{f,min}$ reaches zero (see Figure A.2).
- *Flame propagation stage*: After $t = 0.51\,\mathrm{ms}$, flame propagation occurs, which is not subject of the detailed gKIM model.

For the subsequent analyses, only the *auto-ignition stage* is considered.

A.1.3. A-priori analysis

An *a-priori* analysis is performed to evaluate the auto-ignition manifold used in the *detailed gKIM* model (see Section 2.2.2) based on the DNS dataset. Here, the auto-ignition progress variable is defined as the negative fuel mass fraction $Y_{\mathrm{c_{I,u}}} = -Y_\mathrm{f}$. The scalar fields from the

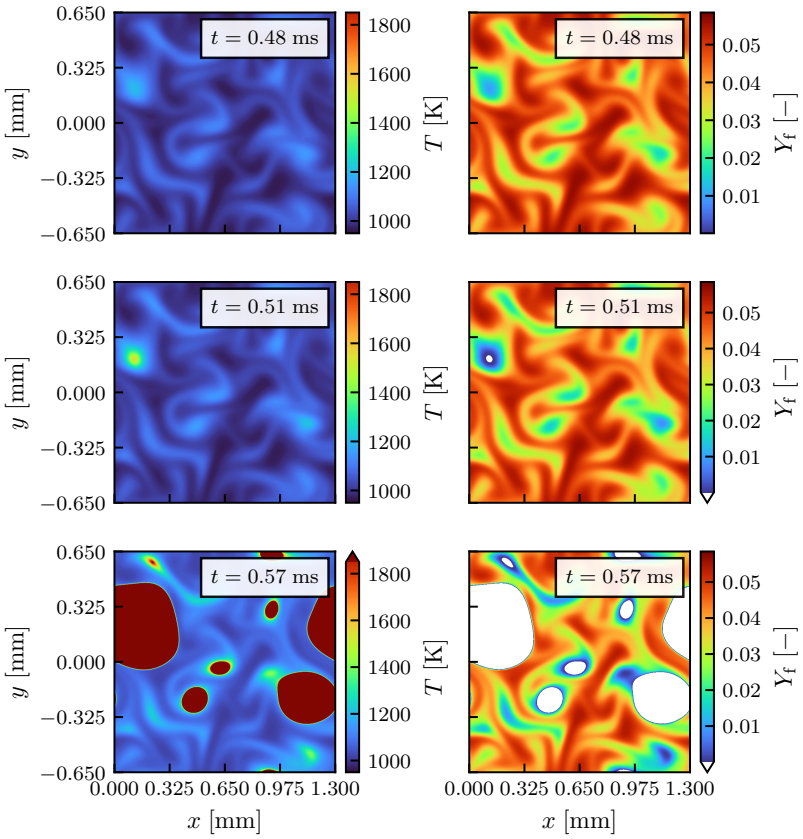

Figure A.2.: Temporal and spatial development of temperature T (left) and fuel mass fraction Y_f (right).

DNS are used to extract the source term of the *detailed gKIM* model $\dot{\omega}_{Y_{\mathrm{c_{I,u,det}}}} = \dot{\omega}^{\mathrm{FLUT3}}$ from the auto-ignition manifold:

$$\dot{\omega}^{\mathrm{FLUT}} = f\left(Y_{\mathrm{c_{I,u}}}^{\mathrm{DNS}}, p^{\mathrm{DNS}}, h^{\mathrm{DNS}}, Z^{\mathrm{DNS}}, Y_{\mathrm{EGR}}^{\mathrm{DNS}}\right) . \tag{A.1}$$

The mean source terms $\overline{\dot{\omega}}^{\mathrm{DNS}}$ and $\overline{\dot{\omega}}^{\mathrm{FLUT}}$ and the mean absolute error $\overline{\varepsilon}_{\mathrm{abs}}$ of a certain time instant are defined as:

$$\overline{\dot{\omega}}^{\mathrm{DNS}} = \frac{1}{N}\sum_{i=1}^{N}\dot{\omega}_i^{\mathrm{DNS}} \tag{A.2}$$

$$\overline{\dot{\omega}}^{\mathrm{FLUT}} = \frac{1}{N}\sum_{i=1}^{N}\dot{\omega}_i^{\mathrm{FLUT}} \tag{A.3}$$

[3]Here, FLUT is the abbreviation for flamelet look-up table and used as a synonym for the auto-ignition manifold in the following.

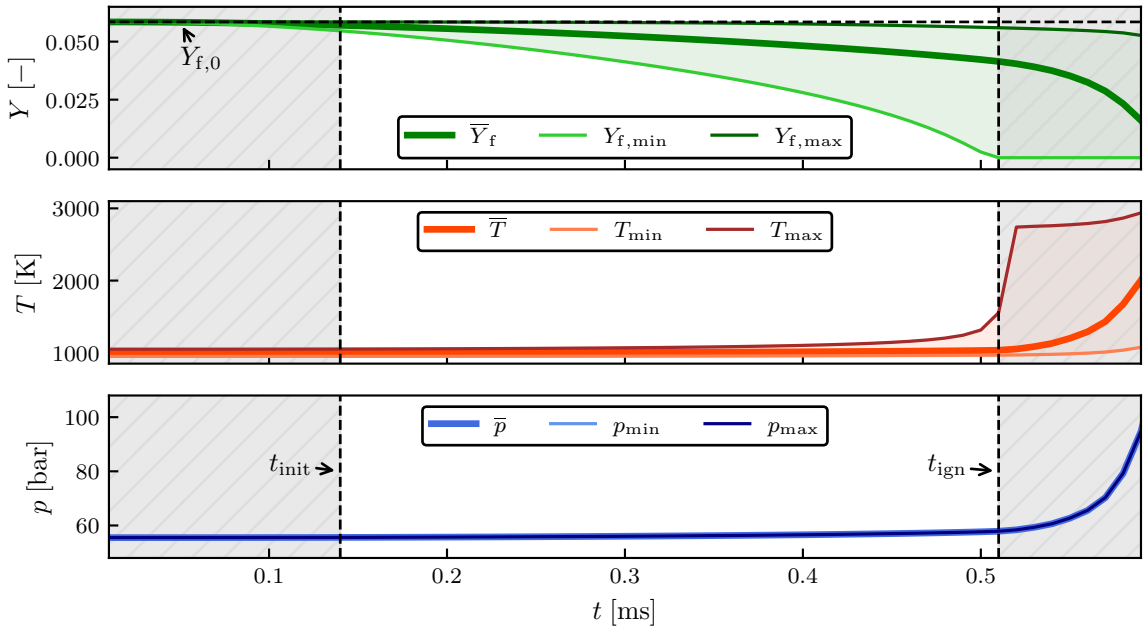

Figure A.3.: Temporal development of fuel mass fraction Y_f (top), temperature T (middle) and pressure p (bottom). The initial fuel mass fraction $Y_{\mathrm{f},0}$ as well as the characteristic times t_init and t_ign are indicated by dashed lines. Areas outside the region of interest are shaded in gray.

$$\overline{\varepsilon}_\mathrm{abs} = \frac{1}{N}\sum_{i=0}^{\mathrm{N}} \varepsilon_{\mathrm{abs},i} = \sum_{i=0}^{\mathrm{N}} \left|\dot{\omega}_i^\mathrm{DNS} - \dot{\omega}_i^\mathrm{FLUT}\right| , \tag{A.4}$$

with i being the cell number of the N total DNS cells and $\dot{\omega}_i^\mathrm{DNS}$ being the respective DNS source term of cell i.

The respective temporal development of these quantities is shown in Figure A.4 for the *auto-ignition stage*. The increasing reaction source term results from the accelerating fuel conversion process. The source term retrieved from the auto-ignition manifold consistently overpredicts the DNS source term. However, the absolute error $\overline{\varepsilon}_\mathrm{abs}$ is below $4\,1/\mathrm{s}$.

In addition to the global error, Figure A.5 shows the local prediction accuracy. Here, the temporal and spatial development of the source terms $\dot{\omega}^\mathrm{DNS}$ and $\dot{\omega}^\mathrm{FLUT}$ as well as the absolute error ε_abs are depicted. For $t = 0.31\,\mathrm{ms}$, there is a systematic yet small underprediction of the local DNS source term. With the build-up of a hot spot at $t = 0.48\,\mathrm{ms}$ (cf. Figure A.2), the auto-ignition manifold is able to reproduce the regions of highest reactivity. However, there is a slight overprediction of the local DNS source term. At $t = 0.50\,\mathrm{ms}$ all regions of higher local source term show an overprediction indicating a relation between the magnitude of the source term and the respective error.

For further characterization, the absolute error ε_abs and relative error $\varepsilon_\mathrm{rel} = \varepsilon_\mathrm{abs}/\dot{\omega}^\mathrm{FLUT}$ are

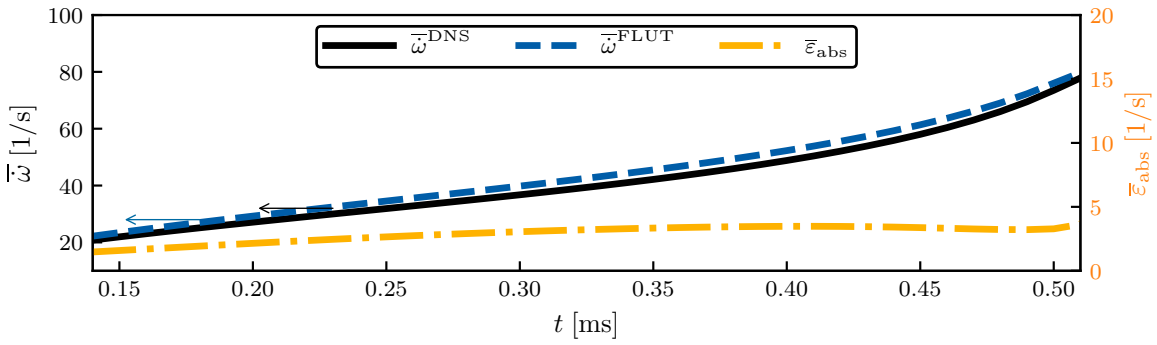

Figure A.4.: Temporal development of mean source terms of DNS $\overline{\dot{\omega}}^{\mathrm{DNS}}$ (black solid line) and FLUT $\overline{\dot{\omega}}^{\mathrm{FLUT}}$ (blue dashed line) as well as absolute error $\overline{\varepsilon}_{\mathrm{abs}}$ (dash-dotted yellow line).

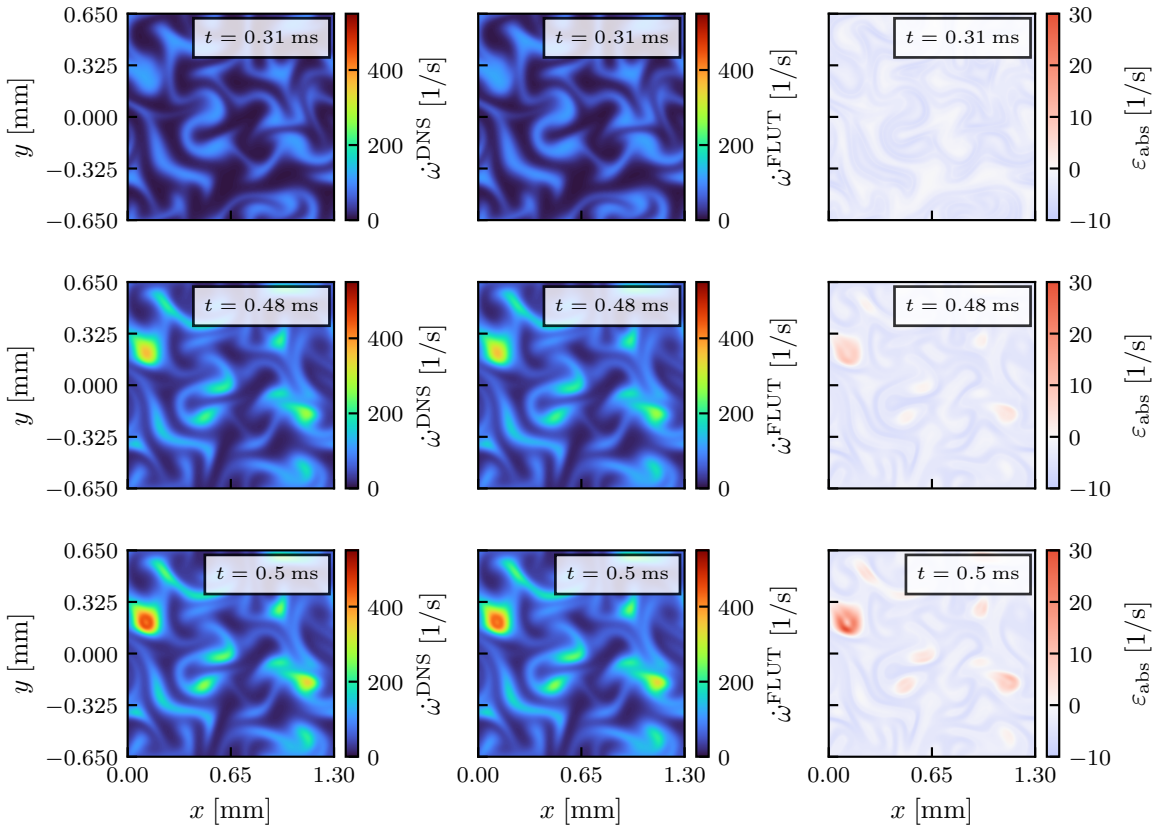

Figure A.5.: Temporal and spatial development of source terms of DNS $\dot{\omega}^{\mathrm{DNS}}$ (left) and FLUT $\dot{\omega}^{\mathrm{FLUT}}$ (center) as well as absolute error $\varepsilon_{\mathrm{abs}}$ (right). The characteristic time t_{ign} is indicated by a dashed line

shown as function of the source term $\dot{\omega}^{\mathrm{FLUT}}$ in Figure A.6. This transformation from the physical to the state space enables the simultaneous consideration of all spatial points for the entire time span under consideration. As indicated by the coloring, there is a correlation between the progress of the auto-ignition process (indicated by the normalized auto-ignition progress variable $c_{\mathrm{I,u}}$) and the respective source term: With higher auto-ignition progress, the source term increases (see Figures A.2 and A.5). The denominator of the relative error approaches values close to zero for small source terms, which complicates the interpretation. Hence, a threshold value of $\dot{\omega}_{\mathrm{thr}} = 75\,1/\mathrm{s}$ is chosen for further analysis of the error:

$$\varepsilon : \begin{cases} |\varepsilon_{\mathrm{abs}}| < 8\,1/\mathrm{s}, & \text{if } \dot{\omega}^{\mathrm{FLUT}} < \dot{\omega}_{\mathrm{thr}} \\ |\varepsilon_{\mathrm{rel}}| < 10\,\%, & \text{otherwise} \end{cases} \tag{A.5}$$

For source terms smaller than $\dot{\omega}_{\mathrm{thr}}$, the absolute error is within the bounds of $\pm 8\,1/\mathrm{s}$. For source terms higher than $\dot{\omega}_{\mathrm{thr}}$, the relative error is within a band of $\pm 10\,\%$.

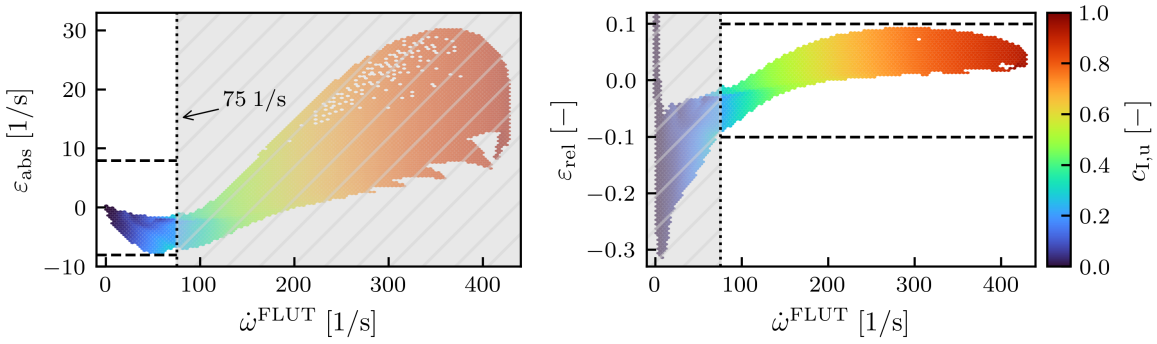

Figure A.6.: Absolute error $\varepsilon_{\mathrm{abs}}$ (left) and relative error $\varepsilon_{\mathrm{rel}}$ (right) as function of the source term extracted from the FLUT $\dot{\omega}^{\mathrm{FLUT}}$. Coloring according to the respective normalized auto-ignition progress variable $c_{\mathrm{I,u}}$. Areas outside the region of interest are shaded in gray. The respective error intervals are indicated by dashed lines, the threshold value of $75\ 1/\mathrm{s}$ by a dotted line.

In summary, the *a-priori* analysis shows that the source term extracted from the auto-ignition manifold reproduces the DNS source term with good accuracy and all spatial structures are recovered. The modeling error stays within limited bands, both in terms of relative and absolute error. With that, the *a priori* analysis indicates, that the auto-ignition modeling can capture the turbulent auto-ignition process under engine-relevant thermodynamic conditions. However, the DNS considers a simplified configuration. Definite conclusions on the applicability of the auto-ignition modeling for investigation of the knocking combustion initiation can only be drawn based on complex full-cycle engine simulations including all relevant processes.

A.1.4. Analysis of turbulent fluctuations

While the *a-priori* analysis is based on the fully resolved DNS data, the detailed gKIM model is applied in an LES framework in engine simulations. Hence, not all turbulent length scales are resolved and sub-grid scales are modeled. In the following, the spatially highly resolved DNS dataset is analyzed to characterize the turbulent fluctuations. Subsequently, the non-resolved fluctuations are incorporated in the modeling employing a turbulence-chemistry-interaction (TCI) closure and the model performance is evaluated.

Statistical analysis

The source term of the detailed gKIM model is extracted from the auto-ignition manifold based on five control variables: $Y_{\mathrm{c_{I,u}}}, p, h, Z, Y_{\mathrm{EGR}}$. For the available DNS dataset of a perfectly premixed stoichiometric isooctane-air mixture Z and Y_{EGR} are constant, while for p no spatial fluctuations are observed. Hence, in the TCI closure model only the fluctuations of the control variables enthalpy h and auto-ignition progress variable $Y_{\mathrm{c_{I,u}}}$ need to be considered.

The distributions of the DNS cell values of h and $Y_{\mathrm{c_{I,u}}}$ are shown in Figure A.7 for different time steps.

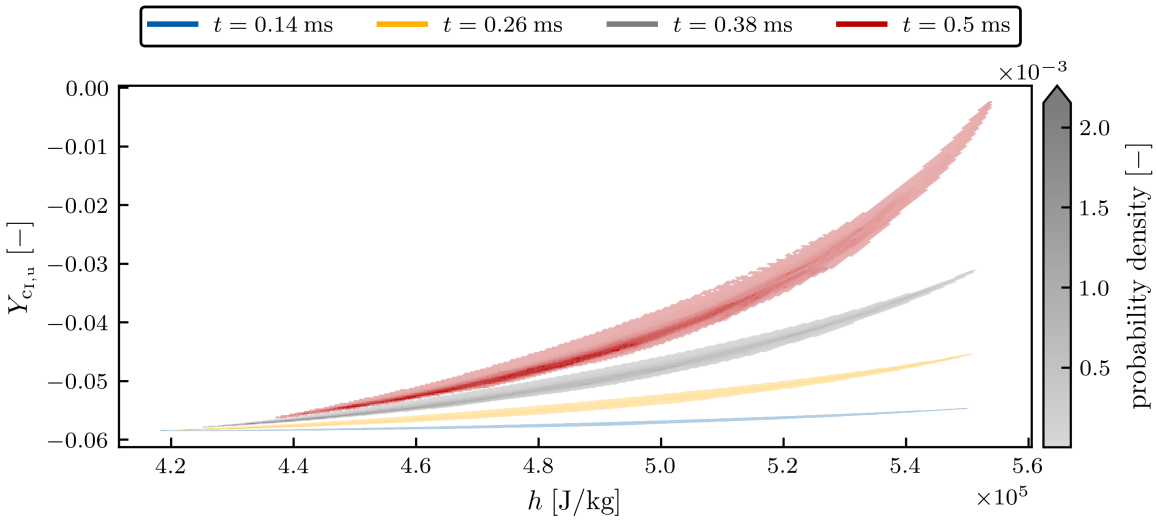

Figure A.7.: Distribution of DNS cell values over enthalpy h and auto-ignition progress variable $Y_{\mathrm{c_{I_u}}}$. Different base colors indicate the different time steps of the sampled data. Higher probability density is indicated by higher saturation of the base color.

At $t = 0.14\,\mathrm{ms}$, the fuel mass fraction is close to the initial value $Y_{\mathrm{f},0}$ in most of the domain, resulting in very low variation of $Y_{\mathrm{c_{I,u}}}$. As a result, the distribution is mainly determined by the enthalpy variation. Further time steps exhibit higher local fuel conversion, leading to an increase in $Y_{\mathrm{c_{I,u}}}$. In this context, a notable correlation exists between high auto-ignition progress and high enthalpy values. Across all time steps, the distribution appears relatively constrained in the h-$Y_{\mathrm{c_{I,u}}}$-space. To investigate the individual contribution, the histograms of $Y_{\mathrm{c_{I,u}}}$ and h are

shown in Figure A.8.

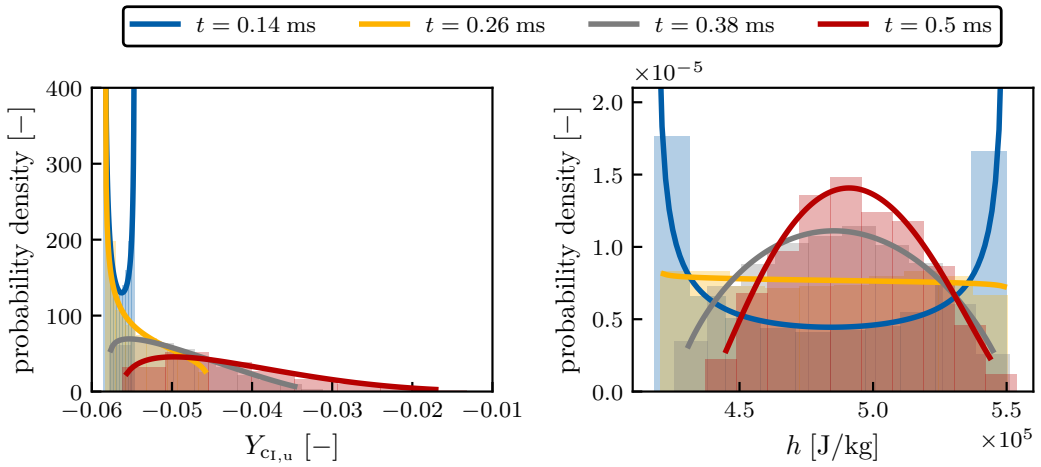

Figure A.8.: Histograms of DNS cell values over auto-ignition progress variable $Y_{c_{I_u}}$ (left) and enthalpy h (right). Solid lines represent β-PDFs fitted to the respective histogram. Different base colors indicate the different time steps of the sampled data.

At $t = 0.14\,\mathrm{ms}$, both histograms show a bimodal distribution. This is attributed to the initial temperature stratification, where regions of higher temperature show auto-ignition progress and hence a higher $Y_{c_{I,u}}$ while regions of lower temperature show no auto-ignition progress yet and hence the respective $Y_{c_{I,u}}$ corresponds to the initial value.

For the enthalpy, turbulent mixing changes the distribution. For the later times considered, the distribution converges toward a normal distribution.

The local stratification of the auto-ignition process is reflected in the temporal development of the distribution. First, the cells of higher auto-ignition progress further react due to the fuel conversion process (cf. difference between $t = 0.14\,\mathrm{ms}$ and $t = 0.26\,\mathrm{ms}$). Thereafter, the entire domain shows auto-ignition progress leading to a shift of the minimum and the mean to higher values. In addition, the distribution becomes wider, as more different auto-ignition stages co-exist.

As a first approximation, those histograms are fitted with a β-PDF:

$$f(x;a,b) = \frac{x^{a-1}\,(1-x)^{b-1}}{B(a,b)} \quad \text{with} \quad B(a,b) = \int_0^1 x^{a-1}\,(1-x)^{b-1}\,dx\,. \tag{A.6}$$

Here, a and b are shape parameters of the β-PDF and are determined based on the mean and variance of the respective distributions. For both control variables and all time steps, the β-PDF gives a reasonable approximation of the histogram. This indicates, that a β-PDF is generally suited to capture the sub-grid scale fluctuations of auto-ignition progress and enthalpy. The applicability in a presumed-PDF approach for TCI modeling is investigated in the following.

Modeling of sub-grid scale fluctuations

For the evaluation of sub-grid scale modeling strategies, the DNS domain is assumed as one single pseudo-LES cell. Hence, the variations within the DNS data are considered as sub-grid scale from the LES perspective. Subsequently, different strategies of TCI closure modeling are applied and evaluated:

- *Fully-resolved fluctuations*: The mean auto-ignition manifold source term $\overline{\dot{\omega}}^{\mathrm{FLUT}}$ based on the individual values of all DNS cells is considered as the reference.
- *No closure*: The pseudo-LES *a-priori* source term of the detailed gKIM model $\dot{\omega}^{\mathrm{pLES}}$ is retrieved from the auto-ignition manifold based on the mean DNS values of the control variables:

$$\dot{\omega}^{\mathrm{pLES}} = f\left(\overline{Y}_{\mathrm{c_{I,u}}}^{\mathrm{DNS}}, \overline{h}^{\mathrm{DNS}}, \overline{p}^{\mathrm{DNS}}, \overline{Z}^{\mathrm{DNS}}, \overline{Y}_{\mathrm{EGR}}^{\mathrm{DNS}}\right) \tag{A.7}$$

- *Presumed-PDF approach*: A presumed-PDF approach is applied for TCI modeling. Based on the previous findings that the individual distributions of auto-ignition progress variable and enthalpy can be fitted with a β-PDF, the auto-ignition manifold is integrated with the respective β-PDFs and denoted as f^* hereafter. Three modeling approaches are investigated:
  - *Enthalpy fluctuations*: The enthalpy SGS fluctuations are approximated with a β-PDF:

$$\overline{\dot{\omega}}^{\beta(h)} = \frac{1}{n_{\mathrm{s}}} \sum_{i=1}^{n_{\mathrm{s}}} f^*\left(h_i^{\beta}, \overline{Y}_{\mathrm{c_{I,u}}}, \overline{p}, \overline{Z}, \overline{EGR}\right) \ , \tag{A.8}$$

    where $h_i^{\beta} = f\left(\overline{h}, \overline{h}''^2\right)$ and the number of samples n_{s} is chosen as 10^4.
  - *Progress variable fluctuations*: The auto-ignition progress variable SGS fluctuations are considered:

$$\overline{\dot{\omega}}^{\beta(Y_{\mathrm{c_{I,u}}})} = \frac{1}{n_{\mathrm{s}}} \sum_{i=1}^{n_{\mathrm{s}}} f^*\left(Y_{\mathrm{c_{I,u}},i}^{\beta}, \overline{h}, \overline{p}, \overline{Z}, \overline{EGR}\right) \ , \tag{A.9}$$

    with $Y_{\mathrm{c_{I,u}},i}^{\beta} = f\left(\overline{Y}_{\mathrm{c_{I,u}}}, \overline{Y}_{\mathrm{c_{I,u}}}''^2\right)$.
  - *Progress variable and enthalpy fluctuations*: Individual β-PDF modeling is applied for both auto-ignition progress variable and enthalpy:

$$\overline{\dot{\omega}}^{\beta(Y_{\mathrm{c_{I,u}}}),\beta(h)} = \frac{1}{n_{\mathrm{s}}^2} \sum_{i=1}^{n_{\mathrm{s}}} \sum_{j=1}^{n_{\mathrm{s}}} f^*\left(Y_{\mathrm{c_{I,u}},i}^{\beta}, h_j^{\beta}, \overline{p}, \overline{Z}, \overline{EGR}\right) \ , \tag{A.10}$$

The respective results are shown in Figure A.9. Neglecting the sub-grid scale fluctuations of the control variables in the pseudo-LES source term $\dot{\omega}^{\mathrm{pLES}}$ leads to an underprediction of the reference source term $\overline{\dot{\omega}}^{\mathrm{FLUT}}$. The modeling of the sub-grid scale fluctuations with a presumed-PDF approach is also not able to recover $\overline{\dot{\omega}}^{\mathrm{FLUT}}$. Considering fluctuations in the enthalpy, $\overline{\dot{\omega}}^{\beta(h)}$ is able to approximate the source term $\overline{\dot{\omega}}^{\mathrm{FLUT}}$ with good accuracy for the initial phase, where the distribution is mainly dependent on the enthalpy (see Figure A.7). For later time steps,

the distribution, in addition, depends on the auto-ignition progress variable (see Figure A.7) and hence, the deviation from $\overline{\dot{\omega}}^{\mathrm{FLUT}}$ increases. Considering the fluctuation of only $Y_{\mathrm{c_{I,u}}}$ or the combined individual fluctuations of $Y_{\mathrm{c_{I,u}}}$ and h results in a source term closer to the reference for later time instants ($t > 0.35$ respectively $t > 0.45$). However, for the initial time phase considered there is no significant increase of the source term for $\overline{\dot{\omega}}^{\beta(Y_{\mathrm{c_{I,u}}}),\beta(h)}$, while $\overline{\dot{\omega}}^{\beta(Y_{\mathrm{c_{I,u}}})}$ even underpredicts the pseudo-LES source term.

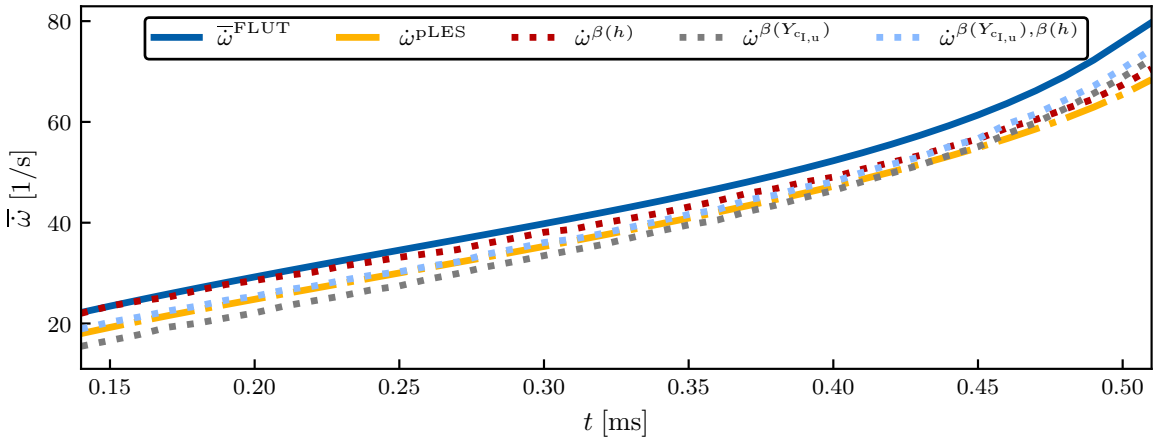

Figure A.9.: Temporal development of the mean source term based on individual DNS cell values $\overline{\dot{\omega}}^{\mathrm{FLUT}}$ (blue dashed line) and source term of pseudo-LES $\dot{\omega}_{\mathrm{pLES}}$ (yellow dash-dotted line). In addition, three different source terms incorporating a β-PDF based presumed PDF approach for enthalpy h and/or auto-ignition progress variable $Y_{\mathrm{c_{I,u}}}$ are shown as dotted lines.

In summary, these observations together with the previously described distributions indicate, that the correlation of enthalpy and auto-ignition progress variable fluctuations must be considered to correctly capture the source term. Consequently, modeling the fluctuations with a univariate β-PDF does not improve the approximation. Here, a bivariate approach may improve the modeling. However, this results in a significant increase in complexity and is therefore outside the scope of this work, but is seen as a promising approach for future development.

A.1.5. Conclusions on the evaluation of the detailed gKIM model based on a DNS dataset

Within this study, the DNS dataset of the turbulent auto-ignition process of an isooctane-air mixture was used for model evaluation. The conducted *a-priori* analysis of the auto-ignition manifold used in the detailed gKIM model showed a reasonable agreement with the reference DNS data. The statistical analysis of turbulent fluctuations shows variations in the enthalpy and the auto-ignition progress variable. Different univariate presumed-PDF approaches are tested but show no significant improvement compared to neglecting TCI modeling. Investigations on bivariate distributions are promising but out of scope for this study.

Although the study provides helpful insights, it should be noted that it is based on a single thermodynamic initial condition. Consequently, either further DNS data or application of the model in more complex configurations is required for more general conclusions.

A.2. Adjustments to the 3-D engine simulation combustion simulation framework based on parameter variation studies

The multi-cycle strategy (see Section 4.1.2) is changed between the studies described in Sections 6.1 and 6.2. The later study takes into account different initial flow fields. Thus, a fixed numerical spark timing leads to different overall combustion speeds. This presents certain challenges and opportunities. On the one hand, modifications in the combustion modeling framework can be applied to improve the prediction of the model. On the other hand, adequate sensitivity of the combustion modeling to the initial flow field must be ensured to capture cycle-to-cycle variations. For this, three different flow fields (one from each thread of the second cycle after initialization) are used as initial conditions. Computing only the initial combustion phase up to 20° CA, the parametrization of the combustion model framework can be adjusted as discussed in the following.

A.2.1. Parametrization of the combustion manifold

The combustion manifold coupled to the combustion model (see Section 2.2.1) is based on the tabulation of laminar freely propagating flames. For the first LES study, these have been calculated using the assumption of a unity Lewis number. For TRF-OS at 1500 RPM and a spark timing of -6.0° CA the respective pressure traces resulting from this modeling strategy are shown in Figure A.10 together with the experimental results.

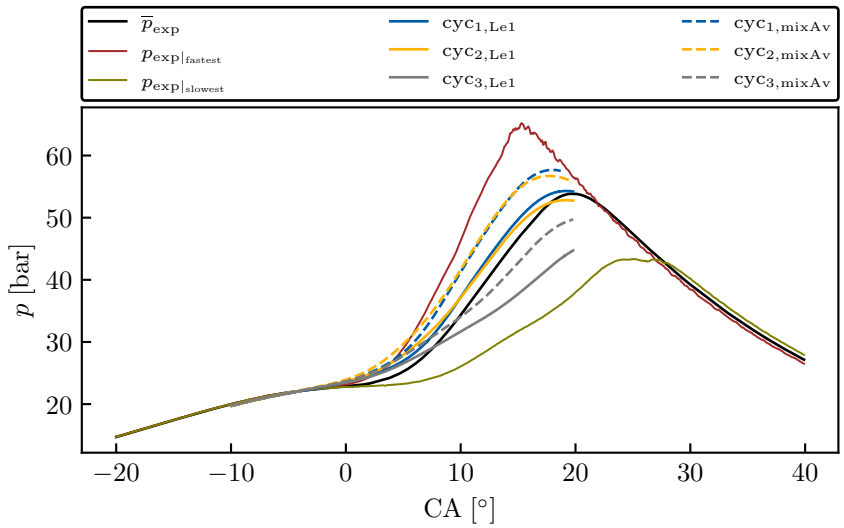

Figure A.10.: Experimental mean as well as fastest and slowest pressure trace (black, brown and olive, respectively). Pressure traces of three LES realizations are shown, where a unity Lewis assumption (solid lines) or mixture-average diffusion model (dashed lines) are used for the creation of the combustion manifold.

The numerical timing of combustion initiation required to reach a peak pressure comparable

to that of the mean experimental pressure leads to the prediction of higher pressures in the early phase around TDC. This means that the overall combustion progress predicted by the LES is too slow. To compensate for that, freely propagating flames are calculated using the mixture-average approach for diffusion modeling. This takes into account the higher diffusion fluxes and results in higher laminar burning velocities s_{L}. These are mapped onto the previously generated combustion manifold. In the study described in Section 6.2, this new manifold is coupled to the LES combustion model, increasing the overall combustion speed as desired. Consequently, the pressure traces of the LES realizations considering mixture-average diffusion show higher peak pressures (see Figure A.10, dashed lines). However, this requires adjusting the combustion initiation parameters to match the experimental envelope, as discussed below.

A.2.2. Parametrization of the combustion initiation model

The combustion initiation method of imposing a sphere of burned state in the spark plug gap is successfully applied in both LES studies (see Sections 6.1 and 6.2). However, the change in the parametrization of the combustion manifold requires a recalibration of the parameters of the combustion initiation model, for which a parameter study has been conducted. A mesh refinement region around the spark plug with a radius of 2 mm shows the best compromise between the resolution of the early combustion phase and additional computational costs. The radius of the initial sphere of burnt gas is reduced from 1.0 to 0.2 mm. The numerical combustion initiation timing is chosen as -8.5° CA. The respective pressure traces are shown in Figure A.11. The adjusted parameter set leads to a better agreement with the experimental pressure trace (cf. blue lines) and hence is used for the study discussed in Section 6.2.

The previous findings are applied to the OP1500 of isooctane with an experimental spark timing of -7.0° CA. The pressure traces of the multi-cycle LES study are shown in Figure A.12. As discussed in Section 6.2 for TRF-OS, the LES realizations show reasonable variation in combustion induced by the differences in the initial flow fields and agree well with the experiments. This indicates the applicability of the adjustment, which could be further investigated in future studies for a wider range of operating conditions.

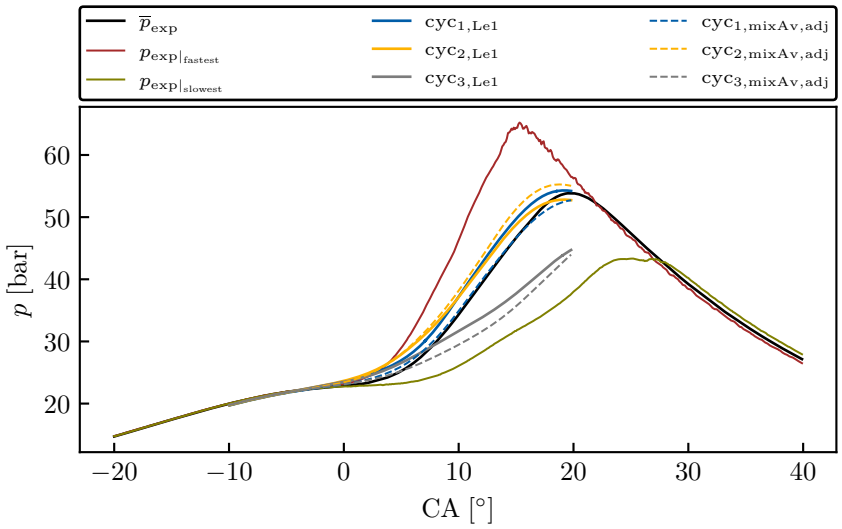

Figure A.11.: Experimental mean as well as fastest and slowest pressure trace (black, brown and olive, respectively). Three LES realizations with unity Lewis assumption (solid lines) and mixture-average diffusion model (dashed lines) used for the creation of the combustion manifold are shown. For the latter, the parameters of the combustion initiation model are adjusted.

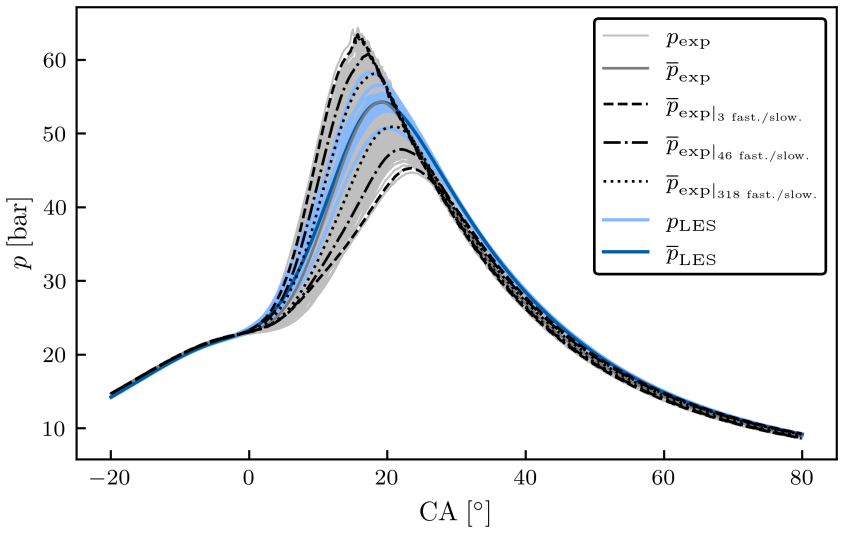

Figure A.12.: Pressure traces of experiments p_{exp} (light gray) and LES realizations p_{LES} (light blue). In addition, the mean pressure traces $\overline{p}_{\mathrm{exp}}$ and $\overline{p}_{\mathrm{LES}}$ are shown (gray and blue, respectively). The black lines indicate estimators for the experimental 1-, 2- and 3-σ intervals (dotted, dash-dotted and dashed, respectively).

Nomenclature

Abbreviation

aTDC	After top dead center
CA	Crank angle
CAI	Controlled Auto-Ignition
CCV	Cycle-to-cycle variations
CFD	Computational fluid dynamics
CHT	Conjugate heat transfer
DDT	deflagration to detonation transition
DNS	Direct Numerical Simulation
EST	Early spark timing
EU	European Union
EV	Exhaust valve
EVO	Exhaust valve opening
EX	Exhaust valve
FEVIS	FEV combustion analysis system
FLUT	Flamelet look-up table
FOSP	Fiber-optical spark plug
FSD	Flame surface density
FVM	Finite volume method
GHG	Green house gas

gKIM	Generalized knock integral method
HCCI	Homogeneous charge compression ignition
ICE	Internal combustion engine
IN	Intake valve
IST	Intermediate spark timing
IV	Intake valve
KIM	Knock integral method
KPP	Knock-Peak-Peak
LES	Large Eddy Simulation
LST	Late spark timing
MFB	Fuel mass fraction burned
MFBKO	Mass fraction bunred at knock onset
MON	Motor octane number
NTC	Negative temperature coefficient
OP	Operating point
OS	Octane sensitivity
PCA	Principle component analysis
PFI	Port-fuel injection
PIV	Particle image velocimetry
PRF	Primary Reference Fuel
RANS	Reynolds Averaged Navier Stokes
RON	Research octane number
SCRE	Single-cylinder research engine
SGS	Sub-grid scale
SI	Spark ignition

ST	Spark timing
TCI	Turbulence-chemistry interaction
TDC	Top dead center
TKI	Tabulated kinetics of ignition (model)
TME	Chair of Thermodynamics of Mobile Energy Conversion Systems
TPA	Three Pressure Analysis
TRF	Toluene Reference Fuel
URANS	Unsteady RANS

Characteristic numbers

Le	Lewis number
Pr	Prandtl number
Re	Reynolds number
Sc	Schmidt number

Greek symbols

α_t	Thermal diffusivity
α_{xy}	Angle on $x-y$-plane
φ	Thermo-chemical state
$\Delta h^0_{f,k}$	Standard enthalpy of formation
Δx	Flame width in x-direction
Δ	Characteristic sub-grid scale length
Δ	Difference
δ_{ij}	Kronecker delta
$\dot{\omega}_k$	Chemical source term
Γ	Diffusion coefficient
λ	Air/fuel ratio

λ	Thermal conductivity
μ	Dynamic viscosity
ν	Kinematic viscosity
Ω_{crit}	Set of critical cells
ϕ	Generic scalar
ρ	Density
Σ	Sub-grid flame surface density
σ	Standard deviation
σ_i	Singular value of velocity gradient tensor
τ	Auto-ignition delay time
τ_{ij}	Viscous stress tensor
$\varepsilon_{\mathrm{abs}}$	Absolute error
T_{u}	Unburned temperature
$\dot{\omega}_{Y_{\mathrm{c_{I,u}}}}$	Auto-ignition progress variable source term
$\varepsilon_{\mathrm{rel}}$	Relative error

Latin symbols

$\mathcal{D}_{kl}$	Binary diffusion coefficient of species k and l
a	Speed of sound
c	Normalized reaction progress variable
C_σ	Model constant of σ-model
c_p	Heat capacity at constant pressure
D_k	Diffusivity of species k into the mixture
$G\left(x, r\right)$	Filter kernel
g_i	Gravitational acceleration in direction i
h	Specific enthalpy

h_{norm}	Normalized enthalpy
h_k	Enthalpy of species k
h_s	Sensible enthalpy
h_t	Total enthalpy
k	Turbulent kinetic energy
M	Mean molecular weight of the mixture
m_{crit}	Critical mass
M_k	Molar mass of species k
n	Integer number
n_{s}	Number of samples
p	Cylinder pressure
p	Probability
q_j	Energy flux
R	Pearson correlation coefficient
R	Universal gas constant
r_j	Radius
S	Source term
s_{L}	Laminar burning velocity
t	Time
T_0	Reference temperature
T_{u}	Unburned temperature
u_a	propagation velocity of auto-igniting mixture
u_i	Velocity in direction i
$u_{\mathrm{g},j}$	Mesh velocity
u'_{SGS}	Unresolved turbulent velocity fluctuations

V	Volume
$V_{k,j}$	Diffusion velocity of species k
X_k	Mole fraction of species k
Y_c	Reaction progress variable
Y_EGR	Mass fraction of exhaust gas recirculation
Y_k	Mass fraction of species k
$Y_{\mathrm{c_{I,u}}}$	Auto-ignition progress variable conditioned on the unburned state
Z	Mixture fraction
$c_\mathrm{I,u}$	Normalized auto-ignition progress variable conditioned on the unburned state
c_I	Normalized auto-ignition progress variable
HP	Horizontal plane
MP	Middle plane
TP	Tumble plane

Operators

$\langle \square \rangle$	Ensemble average of quantity
$\langle \square \rangle$	Mean of filtered quantity
$\langle \square'^2 \rangle$	Ensemble average of variations of quantity
$\overline{\square}$	Filtering
$\overline{\square}$	Mean of quantity
$\widetilde{\square}$	Favre-filtering

Subscripts

cyl	Cylinder
c	Critical
i	Count variable
i, j	Direction

k	Species k
0	Initial value
cell	Cell
crit	Critical
exp	Experimental
f	Fuel
high	High knock intensity
ign	(Auto-)ignition
init	Initial
KO	Knock onset
low	Low knock intensity
max	Maximum
mean	Mean value
min	Minimum
SGS	Sub-grid
thr	Threshold
u	Unburned

Superscripts

β	β-PDF integrated
$^{\mathrm{SP}}$	Average over spark plug gap vicinity at spark timing
m	Molar
SGS	Sub-grid

List of figures

List of tables

Bibliography

Publications with own contributions

[P1] **M. Kircher**, J. Schneider, S. Popp, S. Gierth, M. Günther, and C. Hasse. Experimental and model-based analysis of combustion and auto-ignition of gasoline and three surrogate fuels in a single-cylinder research engine operated under knocking conditions. In: *Int. J. Engine Res.* 24.6 (2023), pp. 2727–2738. DOI: 10.1177/14680874221133143.

[P2] **M. Kircher**, S. Popp, S. Gierth, A. Pati, J. Schneider, M. Günther, and C. Hasse. Investigation of Engine Combustion and Auto-ignition of a Multicomponent Surrogate Fuel with NTC Behavior Under Knocking Conditions. In: *Flow, Turbul. Combust.* 110.1 (2023), pp. 149–169. DOI: 10.1007/s10494-022-00351-9.

[A1] **M. Kircher**, E. Meindl, and C. Hasse. Numerical and experimental study on knocking combustion in turbocharged direct-injection engines for a wide range of operating conditions. In: *Int. J. Engine Res.* 24.2 (2023), pp. 652–671. DOI: 10.1177/14680874211060188.

[A2] J. Schneider, M. Günther, **M. Kircher**, and S. Pischinger. Fiber-optical analysis of weak knock and pressure oscillations in a single cylinder research engine. In: *Proc. Combust. Inst.* 39.1 (2023), pp. 1387–1395. DOI: 10.1016/j.proci.2022.09.005.

Other references

[1] United Nations. *What is the Kyoto Protocol?* 1997. URL: https://unfccc.int/kyoto_protocol (visited on 2023-11-20).

[2] United Nations. *Key aspects of the Paris Agreement*. 2015. URL: https://unfccc.int/most-requested/key-aspects-of-the-paris-agreement (visited on 2023-11-20).

[3] International Energy Agency (IEA). *Electric Vehicles*. 2022. URL: https://www.iea.org/reports/electric-vehicles (visited on 2023-06-22).

[4] World Economic Forum. *1 in 7 cars sold globally now is electric*. 2023. URL: https://www.weforum.org/agenda/2023/03/ev-car-sales-energy-environment-gas/ (visited on 2023-06-22).

[5] D. Yergin. *The new map: Energy, climate, and the clash of nations*. Penguin UK, 2020.

[6] European Automobile Manufacturers' Association (ACEA). *Fuel types of new cars: battery electric 12.1%, hybrid 22.6% and petrol 36.4% market share full-year 2022*. 2023. URL: https://www.acea.auto/fuel-pc/fuel-types-of-new-cars-battery-electric-12-1-hybrid-22-6-and-petrol-36-4-market-share-full-year-2022/ (visited on 2023-06-22).

[7] N. Winton. *Electric Car Sales Will Accelerate, But Gasoline Power Will Retain Big Global Share*. 2020. URL: https://www.forbes.com/sites/neilwinton/2020/10/20/electric-car-sales-will-accelerate-but-gasoline-power-will-retain-big-global-share/ (visited on 2023-06-22).

[8] N. Fraser, H. Blaxill, G. Lumsden, and M. Bassett. Challenges for Increased Efficiency through Gasoline Engine Downsizing. In: *SAE International Journal of Engines* 2.1 (2009), pp. 991–1008.

[9] J. B. Heywood. *Internal combustion engine fundamentals*. New York: McGraw-Hill, 1988, pp. 26–0943–26–0943.

[10] Z. Wang, H. Liu, and R. D. Reitz. Knocking combustion in spark-ignition engines. In: *Prog. Energy Combust. Sci.* 61 (2017), pp. 78–112. DOI: 10.1016/j.pecs.2017.03.004.

[11] G. T. Kalghatgi. Knock onset, knock intensity, superknock and preignition in spark ignition engines. In: *Int. J. Engine Res.* 19.1 (2018), pp. 7–20. DOI: 10/k7mv.

[12] W. E. Dalby. *The internal combustion engine*. Glasgow and Bombay: Blackie and Son Limited, 1922. DOI: 10.1038/110122a0.

[13] C. Miller. *Relation between spark-ignition engine knock, detonation waves, and autoignition as shown by high-speed photography*. Tech. rep. 855. NACA, 1946, p. 68.

[14] U. Spicher, H. Kröger, and J. Ganser. Detection of knocking combustion using simultaneously high-speed schlieren cinematography and multi optical fiber technique. In: *SAE Tech. Pap.* 912312.1991 (1991), pp. 569–588. DOI: 10.4271/912312.

[15] G. König, R. R. Maly, D. Bradley, A. K. Lau, and C. G. Sheppard. Role of exothermic centres on knock initiation and knock damage. In: *SAE Tech. Pap.* 99.1990 (1990), pp. 840–861. DOI: 10.4271/902136.

[16] D. Bradley, C. Morley, X. J. Gu, and D. R. Emerson. "Amplified Pressure Waves During Autoignition: Relevance to CAI Engines". In: *SAE Tech. Pap.* December 2014. 2002. DOI: 10.4271/2002-01-2868.

[17] D. Bradley and G. T. Kalghatgi. Influence of autoignition delay time characteristics of different fuels on pressure waves and knock in reciprocating engines. In: *Combust. Flame* 156.12 (2009), pp. 2307–2318. DOI: 10.1016/j.combustflame.2009.08.003.

[18] X. J. Gu, D. R. Emerson, and D. Bradley. Modes of reaction front propagation from hot spots. In: *Combust. Flame* 133.1-2 (2003), pp. 63–74. DOI: 10.1016/S0010-2180(02)00541-2.

[19] Y. B. Zeldovich. Regime classification of an exothermic reaction with nonuniform initial conditions. In: *Combust. Flame* 39.2 (1980), pp. 211–214. DOI: 10.1016/0010-2180(80)90017-6.

[20] A. Robert, S. Richard, O. Colin, and T. Poinsot. LES study of deflagration to detonation mechanisms in a downsized spark ignition engine. In: *Combust. Flame* 162.7 (2015), pp. 2788–2807. DOI: 10.1016/j.combustflame.2015.04.010.

[21] A. Robert, K. Truffin, N. Iafrate, S. Jay, O. Colin, and C. Angelberger. Large-eddy simulation analysis of knock in a direct injection spark ignition engine. In: *Int. J. Engine Res.* 20.7 (2019), pp. 765–776. DOI: 10.1177/1468087418796323.

[22] S. Fontanesi, A. D'Adamo, and C. J. Rutland. Large-Eddy simulation analysis of spark configuration effect on cycle-to-cycle variability of combustion and knock. In: *Int. J. Engine Res.* 16.3 (2015), pp. 403–418. DOI: 10.1177/1468087414566253.

[23] S. Sarathy, A. Farooq, and G. T. Kalghatgi. Recent progress in gasoline surrogate fuels. In: *Progress in Energy and Combustion Science* 65 (2018), pp. 67–108. DOI: https://doi.org/10.1016/j.pecs.2017.09.004.

[24] E. Singh, J. Badra, M. Mehl, and S. M. Sarathy. Chemical Kinetic Insights into the Octane Number and Octane Sensitivity of Gasoline Surrogate Mixtures. In: *Energy & Fuels* 31.2 (2017), pp. 1945–1960. DOI: 10.1021/acs.energyfuels.6b02659.

[25] A. Robert, S. Richard, O. Colin, L. Martinez, and L. De Francqueville. LES prediction and analysis of knocking combustion in a spark ignition engine. In: *Proc. Combust. Inst.* 35.3 (2015), pp. 2941–2948. DOI: 10.1016/j.proci.2014.05.154.

[26] C. Pera and V. Knop. Methodology to define gasoline surrogates dedicated to auto-ignition in engines. In: *Fuel* 96 (2012), pp. 59–69. DOI: 10.1016/j.fuel.2012.01.008.

[27] M. Mehl, W. J. Pitz, C. K. Westbrook, and H. J. Curran. Kinetic modeling of gasoline surrogate components and mixtures under engine conditions. In: *Proc. Combust. Inst.* 33.1 (2011), pp. 193–200. DOI: 10.1016/j.proci.2010.05.027.

[28] D. Kim, C. K. Westbrook, and A. Violi. Two-stage ignition behavior and octane sensitivity of toluene reference fuels as gasoline surrogate. In: *Combust. Flame* 210 (2019), pp. 100–113. DOI: 10.1016/j.combustflame.2019.08.019.

[29] S. Liu, J. C. Hewson, J. H. Chen, and H. Pitsch. Effects of strain rate on high-pressure nonpremixed n-heptane autoignition in counterflow. In: *Combust. Flame* 137.3 (2004), pp. 320–339. DOI: 10.1016/j.combustflame.2004.01.011.

[30] Y. Ju, W. Sun, M. P. Burke, X. Gou, and Z. Chen. Multi-timescale modeling of ignition and flame regimes of n-heptane-air mixtures near spark assisted homogeneous charge compression ignition conditions. In: *Proc. Combust. Inst.* 33.1 (2011), pp. 1245–1251. DOI: 10.1016/j.proci.2010.06.110.

[31] C. K. Law and P. Zhao. NTC-affected ignition in nonpremixed counterflow. In: *Combust. Flame* 159.3 (2012), pp. 1044–1054. DOI: 10.1016/j.combustflame.2011.10.012.

[32] J. Pan, P. Zhao, C. K. Law, and H. Wei. A predictive Livengood-Wu correlation for two-stage ignition. In: *Int. J. Engine Res.* 17.8 (2016), pp. 825–835. DOI: 10.1177/1468087415619516.

[33] W. R. Leppard. The chemical origin of fuel octane sensitivity. In: *SAE Transactions* 99 (1990), pp. 862–876. DOI: 10.4271/902137.

[34] M. Mehl, T. Faravelli, F. Giavazzi, E. Ranzi, P. Scorletti, A. Tardani, and D. Terna. Detailed chemistry promotes understanding of octane numbers and gasoline sensitivity. In: *Energy and Fuels* 20.6 (2006), pp. 2391–2398. DOI: 10.1021/ef060339s.

[35] P. Dai, Z. Chen, S. Chen, and Y. Ju. Numerical experiments on reaction front propagation in n-heptane/air mixture with temperature gradient. In: *Proc. Combust. Inst.* 35.3 (2015), pp. 3045–3052. DOI: 10.1016/j.proci.2014.06.102.

[36] P. Eckert, S. C. Kong, and R. D. Reitz. Modeling autoignition and engine knock under spark ignition conditions. In: *SAE Tech. Pap.* 2003-01-00 (2003). DOI: 10.4271/2003-01-0011.

[37] M. A. Liberman, M. F. Ivanov, O. E. Peil, D. M. Valiev, and L. E. Eriksson. Numerical modeling of the propagating flame and knock occurrence in spark-ignition engines. In: *Combust. Sci. Technol.* 177.1 (2005), pp. 151–182. DOI: 10.1080/00102200590883813.

[38] L. Liang, R. D. Reitz, C. O. Iyer, and J. Yi. Modeling Knock in Spark-Ignition Engines Using a G-equation Combustion Model Incorporating Detailed Chemical Kinetics. In: *SAE Tech. Pap.* 2007-01-01 (2007). DOI: 10.4271/2007-01-0165.

[39] Z. Wang, Y. Wang, and R. D. Reitz. Pressure oscillation and chemical kinetics coupling during knock processes in gasoline engine combustion. In: *Energy and Fuels* 26.12 (2012), pp. 7107–7119. DOI: 10.1021/ef301472g.

[40] P. Pal, Y. Wu, T. Lu, S. Som, Y. C. See, and A. Le Moine. Multidimensional numerical simulations of knocking combustion in a cooperative fuel research engine. In: *J. Energy Resour. Technol. Trans. ASME* 140.10 (2018), pp. 1–8. DOI: 10.1115/1.4040063.

[41] P. Pal, C. P. Kolodziej, S. Choi, S. Som, A. Broatch, J. Gomez-Soriano, Y. Wu, T. Lu, and Y. C. See. Development of a Virtual CFR Engine Model for Knocking Combustion Analysis. In: *SAE Int. J. Engines* 11.6 (2018), pp. 1069–1082. DOI: 10.4271/2018-01-0187.

[42] C. Chen, P. Pal, M. Ameen, D. Feng, and H. Wei. Large-eddy simulation study on cycle-to-cycle variation of knocking combustion in a spark-ignition engine. In: *Appl. Energy* 261 (2020), pp. 1–33. DOI: 10.1016/j.apenergy.2019.114447.

[43] A. P. da Cruz. Three-dimensional Modeling of Self-ignition in HCCI and Conventional Diesel Engines. In: *Combust. Sci. Technol.* 176.5-6 (2004), pp. 867–887. DOI: 10.1080/00102200490428503.

[44] O. Colin, A. Pires Da Cruz, and S. Jay. Detailed chemistry-based auto-ignition model including low temperature phenomena applied to 3-D engine calculations. In: *Proc. Combust. Inst.* 30 II (2005), pp. 2649–2656. DOI: 10.1016/j.proci.2004.08.058.

[45] V. Knop, L. De Francqueville, F. Duffour, and F. Vangraefschèpe. Influence of the valve-lift strategy in a CAI™ engine using exhaust gas re-breathing - Part 2: Optical diagnostics and 3D CFD results. In: *SAE Tech. Pap.* 2.1 (2009), pp. 271–288. DOI: 10.4271/2009-01-0495.

[46] V. Knop, B. Thirouard, and J. Chérel. Influence of the local mixture characteristics on the combustion process in a CAI™ engine. In: *SAE Int. J. Fuels Lubr.* 1.1 (2009), pp. 1133–1149. DOI: 10.4271/2008-01-1671.

[47] V. Knop, J. B. Michel, and O. Colin. On the use of a tabulation approach to model auto-ignition during flame propagation in SI engines. In: *Appl. Energy* 88.12 (2011), pp. 4968–4979. DOI: 10.1016/j.apenergy.2011.06.047.

[48] J. Livengood and P. Wu. “Correlation of autoignition phenomena in internal combustion engines and rapid compression machines”. In: *Symp. Combust.* Vol. 5. 1. 1955, pp. 347–356. DOI: 10.1016/S0082-0784(55)80047-1.

[49] F. A. Lafossas, M. Castagne, J. P. Dumas, and S. Henriot. Development and validation of a knock model in spark ignition engines using a CFD code. In: *SAE Tech. Pap.* 111.2002 (2002), pp. 1252–1263. DOI: 10.4271/2002-01-2701.

[50] A. P. Kleemann, P. Menegazzi, S. Henriot, and A. Marchal. “Numerical Study on Knock for an SI Engine by Thermally Coupling Combustion Chamber and Cooling Circuit Simulations”. In: *SAE Tech. Pap.* Vol. 112. 2003. 2003, pp. 821–831. DOI: 10.4271/2003-01-0563.

[51] A. Teraji, T. Tsuda, T. Noda, M. Kubo, and T. Itoh. Development of a three-dimensional knock simulation method incorporating a high-accuracy flame propagation model. In: *Int. J. Engine Res.* 6.1 (2005), pp. 73–83. DOI: 10.1243/146808705X7338.

[52] P. Jaworski, P. Priesching, A. Teodorczyk, and W. Bandel. Validation of the Numerical Simulation of Iso-octane Auto-ignition Delay Time in Rapid Compression Machine with the Use of ECFM-3Z (Extended Coherent Flame Model - 3 Zones) Combustion Model Against Experimental Data. In: *Combustion* 30.1 (2010), pp. 1–14.

[53] D. Linse, A. Kleemann, and C. Hasse. Probability density function approach coupled with detailed chemical kinetics for the prediction of knock in turbocharged direct injection spark ignition engines. In: *Combust. Flame* 161.4 (2014), pp. 997–1014. DOI: 10.1016/j.combustflame.2013.10.025.

[54] M. B. Young. Cyclic dispersion in the homogeneous-charge spark-ignition engine—a literature survey. In: *SAE Transactions* 90 (1981), pp. 49–73. DOI: 10.4271/810020.

[55] N. Ozdor, M. Dulger, and E. Sher. “Cyclic Variability in Spark Ignition Engines A Literature Survey”. In: *SAE Tech. Pap.* Vol. 103. 1994. 1994, pp. 1514–1552. DOI: 10.4271/940987.

[56] M. Buschbeck, N. Bittner, T. Halfmann, and S. Arndt. Dependence of combustion dynamics in a gasoline engine upon the in-cylinder flow field, determined by high-speed PIV. In: *Exp. Fluids* 53.6 (2012), pp. 1701–1712. DOI: 10.1007/s00348-012-1384-3.

[57] A. Di Mauro, H. Chen, and V. Sick. Neural network prediction of cycle-to-cycle power variability in a spark-ignited internal combustion engine. In: *Proc. Combust. Inst.* 37.4 (2019), pp. 4937–4944. DOI: 10.1016/j.proci.2018.08.058.

[58] W. Zeng, S. Keum, T. W. Kuo, and V. Sick. Role of large scale flow features on cycle-to-cycle variations of spark-ignited flame-initiation and its transition to turbulent combustion. In: *Proc. Combust. Inst.* 37.4 (2019), pp. 4945–4953. DOI: 10.1016/j.proci.2018.07.081.

[59] D. Dreher, M. Schmidt, C. Welch, S. Ourza, S. Zündorf, J. Maucher, S. Peters, A. Dreizler, B. Böhm, and A. Hanuschkin. Deep feature learning of in-cylinder flow fields to analyze cycle-to-cycle variations in an SI engine. In: *Int. J. Engine Res.* 22.11 (2021), pp. 3263–3285. DOI: 10.1177/1468087420974148.

[60] A. Hanuschkin, S. Zündorf, M. Schmidt, C. Welch, J. Schorr, S. Peters, A. Dreizler, and B. Böhm. Investigation of cycle-to-cycle variations in a spark-ignition engine based on a machine learning analysis of the early flame kernel. In: *Proc. Combust. Inst.* 38.4 (2021), pp. 5751–5759. DOI: 10.1016/j.proci.2020.05.030.

[61] C. J. Rutland. Large-eddy simulations for internal combustion engines – a review. In: *International Journal of Engine Research* 12.5 (2011), pp. 421–451. DOI: 10.1177/1468087411407248.

[62] C. Hasse. Scale-resolving simulations in engine combustion process design based on a systematic approach for model development. In: *Int. J. Engine Res.* 17.1 (2016), pp. 44–62. DOI: 10.1177/1468087415597842.

[63] B. Enaux, V. Granet, O. Vermorel, C. Lacour, C. Pera, C. Angelberger, and T. Poinsot. LES study of cycle-to-cycle variations in a spark ignition engine. In: *Proc. Combust. Inst.* 33.2 (2011), pp. 3115–3122. DOI: 10.1016/j.proci.2010.07.038.

[64] K. Truffin, C. Angelberger, S. Richard, and C. Pera. Using large-eddy simulation and multivariate analysis to understand the sources of combustion cyclic variability in a spark-ignition engine. In: *Combust. Flame* 162.12 (2015), pp. 4371–4390. DOI: 10.1016/j.combustflame.2015.07.003.

[65] L. Zhao, A. A. Moiz, S. Som, N. Fogla, M. Bybee, S. Wahiduzzaman, M. Mirzaeian, F. Millo, and J. Kodavasal. Examining the role of flame topologies and in-cylinder flow fields on cyclic variability in spark-ignited engines using large-eddy simulation. In: *Int. J. Engine Res.* 19.8 (2018), pp. 886–904. DOI: 10.1177/1468087417732447.

[66] L. Engelmann, J. Laichter, P. Wollny, M. Klein, S. A. Kaiser, and A. M. Kempf. Cyclic Variations in the Flame Propagation in an Spark-Ignited Engine: Multi Cycle Large Eddy Simulation Supported by Imaging Diagnostics. In: *Flow, Turbul. Combust.* 110.1 (2023), pp. 91–104. DOI: 10.1007/s10494-022-00350-w.

[67] H. Chu, C. Welch, H. Elmestikawy, S. Cao, M. Davidovic, B. Böhm, A. Dreizler, and H. Pitsch. A Combined Numerical and Experimental Investigation of Cycle-to-Cycle Variations in an Optically Accessible Spark-Ignition Engine. In: *Flow, Turbul. Combust.* 110.1 (2023), pp. 3–29. DOI: 10.1007/s10494-022-00353-7.

[68] S. Fontanesi, S. Paltrinieri, A. D'Adamo, G. Cantore, and C. Rutland. Knock Tendency Prediction in a High Performance Engine Using LES and Tabulated Chemistry. In: *SAE Int. J. Fuels Lubr.* 6.1 (2013), pp. 2013–01–1082. DOI: 10.4271/2013-01-1082.

[69] T. Poinsot and D. Veynante. *Theoretical and numerical combustion*. RT Edwards, Inc., 2005.

[70] J. O. Hirschfelder, C. F. Curtiss, and R. B. Bird. Molecular theory of gases and liquids. In: *Molecular theory of gases and liquids* (1964).

[71] B. J. McBride. *Coefficients for calculating thermodynamic and transport properties of individual species*. Tech. rep. 1993.

[72] P. Thomas and C. Lombard. Geometric conservation law and its application to flow computations on moving grids. In: *AIAA journal* 17.10 (1979), pp. 1030–1037.

[73] I. Demirdžić and M. Perić. Space conservation law in finite volume calculations of fluid flow. In: *International journal for numerical methods in fluids* 8.9 (1988), pp. 1037–1050.

[74] J. H. Ferziger and M. Perić. *Computational Methods for Fluid Dynamics*. Springer Berlin Heidelberg, 2002. DOI: 10.1007/978-3-642-56026-2.

[75] A. N. Kolmogorov. "The local structure of turbulence in incompressible viscous fluid for very large Reynolds number". In: *Dokl. Akad. Nauk. SSSR*. Vol. 30. 1941, pp. 301–303.

[76] A. N. Kolmogorov. "Dissipation of energy in the locally isotropic turbulence". In: *Dokl. Akad. Nauk. SSSR*. Vol. 32. 1941, pp. 19–21.

[77] H. Pitsch. Large-eddy Simulation of Turbulent Combustion. In: *Annual Review of Fluid Mechanics* 38.1 (2006), pp. 453–482. DOI: 10.1146/annurev.fluid.38.050304.092133.

[78] U. Schumann. Subgrid scale model for finite difference simulations of turbulent flows in plane channels and annuli. In: *Journal of computational physics* 18.4 (1975), pp. 376–404.

[79] J. Boussinesq. Theorie de l'ecoulement tourbillant. In: *Mem. Acad. Sci.* 23 (1877), p. 46.

[80] F. Nicoud, H. B. Toda, O. Cabrit, S. Bose, and J. Lee. Using singular values to build a subgrid-scale model for large eddy simulations. In: *Phys. Fluids* 23.8 (2011). DOI: 10.1063/1.3623274.

[81] U. Maas and S. B. Pope. Simplifying Chemical Kinetics: Intrinsic Low-Dimensional Manifolds in Composition Space. In: *Combust. Flame* 88 (1992), pp. 239–264. DOI: 10.1073/pnas.1619819114.

[82] O. Gicquel, N. Darabiha, and D. Thévenin. Laminar Premixed Hydrogen/Air Counterflow Flame Simulations Using Flame Prolongation of ILDM with Differential Diffusion. In: *Proc. Combust. Inst.* 28.2 (2000), pp. 1901–1908. DOI: 10.1016/s0082-0784(00)80594-9.

[83] J. A. van Oijen and L. P. de Goey. Modelling of premixed laminar flames using flamelet-generated manifolds. In: *Combust. Sci. Technol.* 161.1 (2000), pp. 113–137. DOI: 10.1080/00102200008935814.

[84] C. D. Pierce and P. Moin. Progress-Variable Approach for Large-Eddy Simulation of Non-Premixed Turbulent Combustion. In: *J. Fluid Mech.* 504.504 (2004), pp. 73–97. DOI: 10.1017/S0022112004008213.

[85] V. Bykov and U. Maas. The Extension of the ILDM Concept to Reaction-Diffusion Manifolds. In: *Combust. Theory Model.* 11.6 (2007), pp. 839–862. DOI: 10.1080/13647830701242531.

[86] L. Cai, A. Ramalingam, H. Minwegen, K. Alexander Heufer, and H. Pitsch. Impact of exhaust gas recirculation on ignition delay times of gasoline fuel: An experimental and modeling study. In: *Proc. Combust. Inst.* 37.1 (2019), pp. 639–647. DOI: 10.1016/j.proci.2018.05.032.

[87] D. G. Goodwin, H. K. Moffat, I. Schoegl, R. L. Speth, and B. W. Weber. *Cantera: An Object-oriented Software Toolkit for Chemical Kinetics, Thermodynamics, and Transport Processes*. https://www.cantera.org. Version 2.6.0. 2022. DOI: 10.5281/zenodo.6387882.

[88] S. P. R. Muppala, N. K. Aluri, F. Dinkelacker, and A. Leipertz. Development of an algebraic reaction rate closure for the numerical calculation of turbulent premixed methane, ethylene, and propane/air flames for pressures up to 1.0 MPa. In: *Combust. Flame* 140.4 (2005), pp. 257–266. DOI: 10.1016/j.combustflame.2004.11.005.

[89] P. R. Janas. "Large Eddy Simulation of In-Cylinder Phenomena in Spark Ignition Engines". PhD thesis. Universität Duisburg-Essen, 2017, p. 167.

[90] A. Zschutschke, D. Messig, A. Scholtissek, and C. Hasse. *Universal Laminar Flame Solver (ULF)*. 2017. DOI: https://doi.org/10.6084/m9.figshare.5119855.v2.

[91] F. Hoppe, M. Thewes, H. Baumgarten, and J. Dohmen. Water injection for gasoline engines: Potentials, challenges, and solutions. In: *Int. J. Engine Res.* 17.1 (2016), pp. 86–96. DOI: 10.1177/1468087415599867.

[92] M. Thewes, M. Muether, S. Pischinger, M. Budde, A. Brunn, A. Sehr, P. Adomeit, and J. Klankermayer. Analysis of the impact of 2-methylfuran on mixture formation and combustion in a direct-injection spark-ignition engine. In: *Energy and Fuels* 25.12 (2011), pp. 5549–5561. DOI: 10.1021/ef201021a.

[93] P. Burkardt, T. Ottenwälder, A. König, J. Viell, A. Mitsos, C. Wouters, W. Marquardt, S. Pischinger, and M. Dahmen. Toward co-optimization of renewable fuel blend production

and combustion in ultra-high efficiency SI engines. In: *Int. J. Engine Res.* (2021). DOI: 10.1177/14680874211040995.

[94] R. S. Spindt. Air-fuel ratios from exhaust gas analysis. In: *SAE Tech. Pap.* 74 (1965), pp. 788–793. DOI: 10.4271/650507.

[95] D. Bresenham, J. Reisel, and K. Neusen. Spindt air-fuel ratio method generalization for oxygenated fuels. In: *SAE Tech. Pap.* 107 (1998), pp. 2154–2171. DOI: 10.4271/982054.

[96] G. M. Rassweiler and L. Withrow. Motion pictures of engine flames correlated with pressure cards. In: *SAE Tech. Pap.* 33 (1938), pp. 185–204. DOI: 10.4271/380139.

[97] A. Amer, H. Babiker, J. Chang, G. Kalghatgi, P. Adomeit, A. Brassat, and M. Günther. Fuel effects on knock in a highly boosted direct injection spark ignition engine. In: *SAE Tech. Pap.* 9.3 (2012), pp. 1048–1065.

[98] C. K. Westbrook, M. Mehl, W. J. Pitz, and M. Sjöberg. Chemical kinetics of octane sensitivity in a spark-ignition engine. In: *Combust. Flame* 175 (2017), pp. 2–15. DOI: 10.1016/j.combustflame.2016.05.022.

[99] J. P. Szybist and D. A. Splitter. Pressure and temperature effects on fuels with varying octane sensitivity at high load in SI engines. In: *Combust. Flame* 177 (2017), pp. 49–66. DOI: 10.1016/j.combustflame.2016.12.002.

[100] A. Pati. “Numerical investigation of the in-cylinder flow-spray-wall interactions in direct injection engines”. PhD thesis. TU Darmstadt, 2022.

[101] S. Weise and C. Hasse. Reducing the memory footprint in large eddy simulations of reactive flows. In: *Parallel Computing* 49 (2015), pp. 50–65.

[102] D. Paredi, T. Lucchini, G. D’Errico, A. Onorati, S. Golini, and N. Rapetto. Gas Exchange and Injection Modeling of an Advanced Natural Gas Engine for Heavy Duty Applications. In: *SAE Tech. Pap.* 2017-September (2017). DOI: 10.4271/2017-24-0026.

[103] J. Zembi, F. Mariani, and M. Battistoni. Large Eddy Simulation of Ignition and Combustion Stability in a Lean SI Optical Access Engine. In: *SAE Tech. Pap.* 2019 (2019). DOI: 10.4271/2019-24-0087.

[104] P. K. Sweby. High resolution schemes using flux limiters for hyperbolic conservation laws. In: *SIAM journal on numerical analysis* 21.5 (1984), pp. 995–1011.

[105] M. Mehl, J. Y. Chen, W. J. Pitz, S. M. Sarathy, and C. K. Westbrook. An Approach for Formulating Surrogates for Gasoline with Application toward a Reduced Surrogate Mechanism for CFD Engine Modeling. In: *Energy & Fuels* 25.11 (2011), pp. 5215–5223. DOI: 10.1021/ef201099y.

[106] D. Linse, C. Hasse, and B. Durst. An experimental and numerical investigation of turbulent flame propagation and flame structure in a turbo-charged direct injection gasoline engine. In: *Combust. Theory Model.* 13.1 (2009), pp. 167–188. DOI: 10.1080/13647830802524829.

[107] C. Welch, M. Schmidt, L. Illmann, A. Dreizler, and B. Böhm. The Influence of Flow on Cycle-to-Cycle Variations in a Spark-Ignition Engine: A Parametric Investigation of Increasing Exhaust Gas Recirculation Levels. In: *Flow, Turbul. Combust.* 110.1 (2023), pp. 185–208. DOI: 10.1007/s10494-022-00347-5.

[108] F. A. Matekunas. Modes and Measures of Cyclic Combustion Variability. In: *SAE Technical Paper* 830337 (1983). DOI: 10.4271/830337.

[109] L. Engelmann, C. Welch, M. Schmidt, D. Meller, P. Wollny, B. Böhm, A. Dreizler, and A. Kempf. A temporal fluid-parcel backwards-tracing method for Direct-Numerical and Large-Eddy Simulation employing Lagrangian particles. In: *Appl. Energy* 342 (2023), p. 121094. DOI: 10.1016/j.apenergy.2023.121094.

[110] S. Buhl, F. Gleiss, M. Köhler, F. Hartmann, D. Messig, C. Brücker, and C. Hasse. A Combined Numerical and Experimental Study of the 3D Tumble Structure and Piston Boundary Layer Development During the Intake Stroke of a Gasoline Engine. In: *Flow, Turbul. Combust.* 98.2 (2017), pp. 579–600. DOI: 10.1007/s10494-016-9754-1.

[111] A. Lindenthal. "Datenbasierte Analyse der Selbstzündungs-Modellierung auf Basis eines DNS Datensatzes". Bachelor's thesis. TU Darmstadt, 2022.

[112] V. Mittal, D. J. Cook, and H. Pitsch. An extended multi-regime flamelet model for IC engines. In: *Combust. Flame* 159.8 (2012), pp. 2767–2776. DOI: 10.1016/j.combustflame.2012.01.014.

[113] S. Jerzembeck, N. Peters, P. Pepiot-Desjardins, and H. Pitsch. Laminar burning velocities at high pressure for primary reference fuels and gasoline: Experimental and numerical investigation. In: *Combust. Flame* 156.2 (2009), pp. 292–301. DOI: 10.1016/j.combustflame.2008.11.009.